



# **UNIVERSIDAD DE INVESTIGACIÓN DE TECNOLOGÍA EXPERIMENTAL YACHAY**

**Escuela de Ciencias Físicas y Nanotecnología**

**TÍTULO: Tight binding model of a superconducting nanowire**

Trabajo de integración curricular presentado como requisito para la  
obtención del título de Físico

**Autor:**

Torres Luna Juan Daniel

**Tutor:**

Ph.D. Medina Dagger Ernesto Antonio

Urququí, Julio, 2020

**SECRETARÍA GENERAL**  
**(Vicerrectorado Académico/Cancillería)**  
**ESCUELA DE CIENCIAS FÍSICAS Y NANOTECNOLOGÍA**  
**CARRERA DE FÍSICA**  
**ACTA DE DEFENSA No. UITEY-PHY-2020-00013-AD**

A los 12 días del mes de junio de 2020, a las 14:30 horas, de manera virtual mediante videoconferencia, y ante el Tribunal Calificador, integrado por los docentes:

<b>Presidente Tribunal de Defensa</b>	Dr. PINTO ESPARZA, HENRY PAUL , Ph.D.
<b>Miembro No Tutor</b>	Dra. PERALTA ARCIA, MAYRA ALEJANDRA DE JESUS , Ph.D.
<b>Tutor</b>	Dr. MEDINA DAGGER, ERNESTO ANTONIO, Ph.D.

El(la) señor(ita) estudiante **TORRES LUNA, JUAN DANIEL**, con cédula de identidad No. **1104771157**, de la **ESCUELA DE CIENCIAS FÍSICAS Y NANOTECNOLOGÍA**, de la Carrera de **FÍSICA**, aprobada por el Consejo de Educación Superior (CES), mediante Resolución **RPC-SO-39-No.456-2014**, realiza a través de videoconferencia, la sustentación de su trabajo de titulación denominado: **Tight Binding Model of a Superconducting Nanowir**, previa a la obtención del título de **FÍSICO/A**.

El citado trabajo de titulación, fue debidamente aprobado por el(los) docente(s):

<b>Tutor</b>	Dr. MEDINA DAGGER, ERNESTO ANTONIO, Ph.D.
--------------	---

Y recibió las observaciones de los otros miembros del Tribunal Calificador, las mismas que han sido incorporadas por el(la) estudiante.

Previamente cumplidos los requisitos legales y reglamentarios, el trabajo de titulación fue sustentado por el(la) estudiante y examinado por los miembros del Tribunal Calificador. Escuchada la sustentación del trabajo de titulación a través de videoconferencia, que integró la exposición de el(la) estudiante sobre el contenido de la misma y las preguntas formuladas por los miembros del Tribunal, se califica la sustentación del trabajo de titulación con las siguientes calificaciones:

Tipo	Docente	Calificación
Presidente Tribunal De Defensa	Dr. PINTO ESPARZA, HENRY PAUL , Ph.D.	10,0
Tutor	Dr. MEDINA DAGGER, ERNESTO ANTONIO, Ph.D.	10,0
Miembro Tribunal De Defensa	Dra. PERALTA ARCIA, MAYRA ALEJANDRA DE JESUS , Ph.D.	10,0

Lo que da un promedio de: **10 (Diez punto Cero)**, sobre 10 (diez), equivalente a: **APROBADO**

Para constancia de lo actuado, firman los miembros del Tribunal Calificador, el/la estudiante y el/la secretario ad-hoc.

*Certifico que en cumplimiento del Decreto Ejecutivo 1017 de 16 de marzo de 2020, la defensa de trabajo de titulación (o examen de grado modalidad teórico práctica) se realizó vía virtual, por lo que las firmas de los miembros del Tribunal de Defensa de Grado, constan en forma digital.*

**TORRES LUNA, JUAN DANIEL**  
**Estudiante**

Dr. PINTO ESPARZA, HENRY PAUL , Ph.D.  
**Presidente Tribunal de Defensa**

Dr. MEDINA DAGGER, ERNESTO ANTONIO, Ph.D.  
**Tutor**

Dra. PERALTA ARCIA, MAYRA ALEJANDRA DE JESUS , Ph.D.  
**Miembro No Tutor**

CIFUENTES TAFUR, EVELYN CAROLINA  
**Secretario Ad-hoc**

## AUTORÍA

Yo, **JUAN DANIEL TORRES LUNA**, con cédula de identidad **1104771157**, declaro que las ideas, juicios, valoraciones, interpretaciones, consultas bibliográficas, definiciones y conceptualizaciones expuestas en el presente trabajo; así como, los procedimientos y herramientas utilizadas en la investigación, son de absoluta responsabilidad de el/la autora (a) del trabajo de integración curricular. Así mismo, me acojo a los reglamentos internos de la Universidad de Investigación de Tecnología Experimental Yachay.

Urcuquí, Julio, 2020.



---

Juan Daniel Torres Luna  
CI: 1104771157

## AUTORIZACIÓN DE PUBLICACIÓN

Yo, **JUAN DANIEL TORRES LUNA**, con cédula de identidad **1104771157**, cedo a la Universidad de Investigación de Tecnología Experimental Yachay, los derechos de publicación de la presente obra, sin que deba haber un reconocimiento económico por este concepto. Declaro además que el texto del presente trabajo de titulación no podrá ser cedido a ninguna empresa editorial para su publicación u otros fines, sin contar previamente con la autorización escrita de la Universidad.

Asimismo, autorizo a la Universidad que realice la digitalización y publicación de este trabajo de integración curricular en el repositorio virtual, de conformidad a lo dispuesto en el Art. 144 de la Ley Orgánica de Educación Superior

Urcuquí, Julio, 2020.



---

Juan Daniel Torres Luna  
CI: 1104771157

## **Agradecimientos**

A mis profesores, quienes siempre me guiaron por el camino de la ciencia y de la excelencia.

## Abstract

Majorana bound states (MBS) are topologically protected zero energy modes with exciting properties to build a decoherence free quantum computer. MBS appear for the first time in the Kitaev's toy model, which can be effectively built from elementary interactions. In 2014, an experimental setup was built which consisted of a three layer zig-zag Fe nanowire, which is ferromagnetic (FM), deposited on top of a Pb (110) superconducting (SC) surface where SC and Rashba spin-orbit (SO) interactions are inherited by proximity effects. As expected, the experiment showed clear evidence of MBS localized at the ends of the wire. However, further theoretical analysis is required to understand and control the physical features of the excitations. In this work we develop an analytical tight-binding model of the experimental setup using matrix partitioning techniques. We describe the mobile electrons ( $\pi$ -band) of the nanowire including effectively the  $\sigma$ -band, and the proximity induced SC and SO. The geometrical details of the setup are included within the Slater-Koster formalism, and analytical expressions for the effective interactions are derived. We analyze the interplay between SC and FM and characterize its influence on the topological phase by calculating the spectra and Pfaffian invariant. Finally, we determine optimal experimental conditions for the appearance of MBS.

**Keywords:** Ferromagnetism, superconductivity, Spin Orbit, Majorana.

## Resumen

Los estados ligados de Majorana son estados de cero energía con propiedades que pueden ser aplicadas para construir una computadora cuántica libre de errores. Aparecieron por primera vez en el modelo de juguete Kitaev, el cual puede ser construido de manera efectiva usando interacciones elementales. En el 2014, un dispositivo experimental que indicaba la presencia de estados ligados de Majorana, fue construido. Consiste en un cable ferromagnético de átomos de hierro depositado sobre una superficie (110) superconductora de plomo la cual presenta interacción de espín del tipo Rashba. Estas interacciones son transferidas al cable a través de efectos de proximidad. El experimento indicó evidencia clara de estas partículas, sin embargo carecía de un análisis teórico que permita entender la física del sistema. En este trabajo desarrollamos un modelo analítico de tight-binding correspondiente al dispositivo experimental utilizando métodos de particionado de matrices. Describimos los electrones móviles del sistema (banda  $\pi$ ), e incluimos de manera efectiva los electrones internos (banda  $\sigma$ ) y el efecto de proximidad. Los detalles geométricos son incluidos usando el formalismo de Slater-Koster, y derivamos expresiones analíticas para las interacciones del sistema. Analizamos la competencia entre la superconductividad y el ferromagnetismo, así como su influencia sobre la fase topológica del sistema. Finalmente, determinamos las condiciones experimentales óptimas para que existan los estados ligados de Majorana.

**Palabras clave:** Ferromagnetismo, superconductividad, Spin Orbit, Majorana.

# Contents

<b>List of Figures</b>	<b>viii</b>
<b>List of Tables</b>	<b>xi</b>
<b>1 Introduction</b>	<b>1</b>
1.1 Problem Statement . . . . .	3
1.2 General and Specific Objectives . . . . .	4
<b>2 Methodology</b>	<b>5</b>
2.1 Slater Koster Integrals . . . . .	5
2.2 Tight Binding Model of Monolayer Graphene . . . . .	7
2.2.1 Geometrical Structure . . . . .	7
2.2.2 Reciprocal Space Representation . . . . .	7
2.2.3 Effective Hamiltonian at the K point . . . . .	9
2.2.4 Chirality and Polarization . . . . .	10
2.3 Matrix Perturbation Theory: The Band Folding Method . . . . .	11
2.4 Spin Orbit in Graphene . . . . .	13
2.5 The Kitaev Model . . . . .	14
2.5.1 Majorana Operators . . . . .	15
2.5.2 Real Space Kitaev Model . . . . .	15
2.5.3 Reciprocal Space Kitaev Hamiltonian . . . . .	19
2.5.4 Linear Approximation of the Kitaev Hamiltonian . . . . .	20
2.5.5 Majorana Fermions at a Domain Wall . . . . .	21
2.6 Effective TB model of a ferromagnetic chain of atoms on top of a superconducting surface . . . . .	22
2.6.1 Unit Cell . . . . .	23
2.6.2 Atomic basis and orbital structure . . . . .	23
2.6.3 Effective Single Orbital Chain . . . . .	27
2.6.4 Proximity Induced Superconductivity and Rashba SO from Pb surface . . . . .	28

2.6.5	Effective $2 \times 2$ Hamiltonian . . . . .	31
2.6.6	Deformation Scheme . . . . .	32
<b>3</b>	<b>Results &amp; Discussion</b>	<b>35</b>
3.1	Effective Hamiltonian . . . . .	35
3.2	Physical Parameters . . . . .	35
3.3	Real Space Signatures of MBS . . . . .	36
3.3.1	Effective Interactions . . . . .	36
3.3.2	Topological phase . . . . .	37
3.3.3	Wavefunctions of MBS . . . . .	41
3.3.4	Local Density of States . . . . .	42
3.3.5	Experimental Signatures: STM measurements . . . . .	42
<b>4</b>	<b>Conclusions &amp; Outlook</b>	<b>45</b>
<b>A</b>	<b>Spin Orbit Interaction</b>	<b>47</b>
<b>B</b>	<b>Tight-Binding Method</b>	<b>49</b>
B.1	Direct Integral Matrix . . . . .	50
B.2	Overlap Integral Matrix . . . . .	51
<b>C</b>	<b>Theory of Superconductivity</b>	<b>53</b>
C.1	BCS Theory . . . . .	53
C.1.1	BCS Ground State . . . . .	54
C.1.2	BCS Ground State Energy . . . . .	54
C.2	Bogoliubov-de-Gennes Hamiltonian . . . . .	55
<b>D</b>	<b>Topology in Condensed Matter: SSH Model</b>	<b>57</b>
D.1	Bulk Properties . . . . .	57
D.2	Edge States . . . . .	59
<b>E</b>	<b>Effective Hamiltonians and Block Diagonalization</b>	<b>61</b>
E.0.1	Energy-Independent Partitioning Methods . . . . .	61
	<b>Bibliography</b>	<b>65</b>

# List of Figures

1.1	Some physical realizations of devices with MBS. (a) False-colour scanning electron micrograph of device A. Image and caption taken from Zhang, et. al. (2018) <sup>1</sup> . (b) Schematics of device A. Image taken from literature <sup>1</sup> . (c) Schematic of the proposal for Majorana quasiparticle realization and detection: a ferromagnetic atomic chain is placed on the surface of strongly spin-orbit coupled superconductor and studied using scanning tunneling microscopy. Image and caption taken from Nadj, et. al, (2015) <sup>2</sup> . (d) Model calculation of the local density of states (LDOS) of the atomic chain embedded in a 2D superconductor. Image and caption taken from literature <sup>2</sup> . . . . .	2
2.1	Sketch of a linear chain of artificial atoms with two possible states: $p_z$ and $d_{xz}$ orbitals. The parameter $V_{pp\pi}$ describes hopping between the neighboring $p$ orbitals and $V_{pd\pi}$ between the $p$ and $d_{xz}$ orbitals, where the $\pi$ bondings are represented by tunnels. Image and caption taken from the literature <sup>3</sup> . . . . .	6
2.2	Two $d_{z^2-r^2}$ orbitals connected by a vector (red) in the XYZ coordinate system. The angles with respect to each axis are $\alpha, \beta$ and $\gamma$ . . . . .	6
2.3	SK parameters of the $\sigma$ and $\pi$ bonding in the $d_{z^2-r^2}$ orbital. Frontal(blue) overlap corresponds to $\sigma$ sector. Lateral(red) overlap corresponds to $\pi$ sector. A bonding along a direction perpendicular to $\sigma$ and $\pi$ corresponds to the $\delta$ bonding. . . . .	6
2.4	Geometrical structure of graphene taken from the book <i>Graphene Nanoelectronics</i> by McCann <sup>4</sup> . Graphene lattice has two inequivalent atoms called A (white) and B (black). The area in gray represents the primitive cell of graphene that contains a pair of atoms A and B. The lattice parameter is $a$ . The nearest neighbor vectors that connect A with the three closest B atoms are labeled $\delta$ . . . . .	8
2.5	3D spectrum of a graphene monolayer. Electrons move along $k_x$ and $k_y$ within the first Brillouin zone.	9
2.6	Cut of the graphene spectra along $k_y = 0$ . At the point K two Dirac cones can be appreciated. Inset: A zoom of the Dirac cone at K is shown. . . . .	9
2.7	Graphical representation of MBS. Each domino represents two Majoranas $\gamma_n$ . There are 4 electrons, then 8 Majoranas. Image taken from the course <i>Topology in Condensed Matter</i> <sup>5</sup> . . . . .	15
2.8	Calculated eigenvalues of the Kitaev chain represent the energy of the lowest states. Two zero energy modes can be observed at the end. . . . .	17
2.9	Calculated wavefunctions of low-energy states. (Red) Wavefunction of MBS localized at the ends of the wire. (Blue) First mode of the chain. . . . .	17

2.10	Calculated phase transition between trivial and topological phase for the Kitaev wire. Low energy spectra is shown as a function of the chemical potential $\mu$ . The lowest level is shown in red, and it marks the topological phase when it is at zero energy. . . . .	18
2.11	Spectra of Kitaev disperssion relation with parameters (eV): $\Delta = 1, \mu = 0.5 \omega = 0.5$ . Al . . . . .	20
2.12	Spectra of Kitaev disperssion relation with parameters (eV): $\Delta = 1, \mu = 1.5 \omega = 0.5$ . . . . .	20
2.13	Graphical representation of the computed wavefunctions at a domain wall for different mass functions in the Kitaev model. Red and blue line: $ \Psi(x) ^2$ . Black dashed line: $m(x)$ . Blue region: $m(x) < 0$ . Red region: $m(x) > 0$ . (a) $m(x) = x$ . (b) $m(x) = \arctan(x)$ . (c) $m(x) = -x^2 + 3$ . . . . .	21
2.14	Lateral view of the atomic wire showing Fe (blue) atoms and the bonds (gray), on top of a Pb (orange) surface. . . . .	22
2.15	Unit cell of the ferromagnetic atomic chain. Two layers of Pb atoms are considered to interact at the top of the surface. (a) Lateral view where the Fe atoms are called <b>A</b> , <b>B</b> and <b>C</b> . (b) Front view where all the five Pb atoms can be observed. Pb atom <b>D'</b> (gray) is behind Fe atom <b>C</b> . . . . .	25
2.16	(a) Symmetry breaking process where two Pb atoms lift symmetrically. (b) Symmetry breaking process where two Pb atoms lift anti-symmetrically. . . . .	30
2.17	(a) SK integrals of the atomic chain. (b) SK integrals that connect Pb to Fe from $p$ -orbitals. . . . .	32
3.1	Effective interactions as a function $\theta$ . (a) Magnitude of energy shift in $d$ -orbitals caused by magnetic order. (b) Magnitude of energy shift in <b>B</b> atom due to BF of <b>C</b> atom. (c) Rashba SO and SC gap as a function of $\theta$ . (d) Magnitude of SO-exchange interaction, $\xi_J$ , as a function of $\theta$ for different values of $J$ . . . . .	37
3.2	Low energy spectra for an atomic chain of $L = 200$ sites with parameters from Table 3.1, and $J = 1.5$ eV. The two lowests states are shown in red. The shaded gray region is considered the topological phase of the system and the energy difference between the these two sattes is 0.005eV. . . . .	38
3.3	Zoom of the zero-energy states in Fig. 3.2. . . . .	39
3.4	Low-energy spectra a s function of $J$ , angular configuration <b>1</b> , and $\Delta=0.05$ eV. Criteria for the shaded region (topological phase) was $10^{-7}$ eV. . . . .	40
3.5	Low-energy spectra a s function of $J$ , angular configuration <b>2</b> , and $\Delta=0.3$ eV. Criteria for the shaded region (topological phase) was 5 meV. . . . .	40
3.6	Wavefunctions of the two lowests energy states in angular configuration <b>1</b> , and $J = 1.5$ eV. . . . .	41
3.7	Wavefunctions of the two lowests energy states in angular configuration <b>2</b> , and $J = 1.8$ eV. . . . .	42
3.8	Illustrative image of the local density of states of an atomic chain of 100 sites of length. Axes in plane represent position (atomic sites) and energy (eV), and vertical axis represents $ \Psi ^2$ . States out of the gao are orange, while in gap states are yellow. Parameters used are within the topological regime, but without discussion purpouses. . . . .	43

# List of Tables

2.1	Orbital basis of $p$ and $d$ orbitals in the cartesian and spherical harmonic basis. These basis set is used to describe the different atomic species of the system. Note that the $d$ orbitals were related to lie around the $x$ direction, but SO matrix elements have not changed. . . . .	24
2.2	Spin orbit interaction matrix elements for $p$ and $d$ orbitals. Here, $\xi_p$ ( $\xi_d$ ) is the magnitude of the SO interaction between $p$ ( $d$ ) orbitals, and the $\sigma_i$ operators are the spin Pauli matrices. Note that there is no SO interaction between $p$ and $d$ orbitals. . . . .	24
2.3	Slater Koster integrals for $d$ orbitals. Vertical and horizontal lines separate the subspace of $d$ bands $\sigma$ , $\pi$ and $\delta$ . Here $V_{dd\sigma}$ , $V_{dd\pi}$ and $V_{dd\delta}$ are the SK parameters that describe the strength of the bonding. . . . .	25
2.4	Matrix elements of the interaction between orbitals within the chain without ferromagnetic Stoner interaction. Internal lines are used to separate the three bands $\pi$ , $\sigma$ and $\delta$ in that order. . . . .	27
2.5	Slater Koster integrals for $d_{xz}$ and $p$ orbitals for all the atoms in the unit cell except for $\mathbf{D}'$ . Also, for Pb atoms only $p_x$ and $p_z$ are considered. Since the symmetry of the unit cell (Fig. 2.15), all the SK integrals can be expressed with two expressions $U_x$ and $U_z$ . . . . .	29
2.6	Slater Koster integrals for $d_{xz}$ and $p$ orbitals for all the atoms in the unit cell except for $\mathbf{D}'$ . Also, for Pb atoms only $p_x$ and $p_z$ are considered. Since the symmetry of the unit cell (Fig. 2.15), all the SK integrals can be expressed with two expressions $U_x$ and $U_z$ . . . . .	29
3.1	SK parameters for $d$ and $p$ orbitals. . . . .	36
3.2	Calculated effective SO and SC interactions for two different angular configurations of the atomic chain and for $\Delta = 0.05$ eV. Atomic and SK parameters were taken from Table 3.1. . . . .	38



# Chapter 1

## Introduction

Majorana particles appeared for the first time in 1930 in the work of Ettore Majorana<sup>6</sup>. Majorana particles are characterized by being its own antiparticles. The notion of antiparticle was suggested by Dirac in order to interpret the negative energy solutions of his equation<sup>7</sup>, which were discovered soon after his prediction. The search for Majorana particles continues in the realm of fundamental physics to this day. The neutrino was proposed to be a Majorana particle, but there is no definite assessment for of this fact yet.

In the context of condensed matter physics, Majorana bound states (MBS) can be built from elementary excitations of a combination of materials<sup>8</sup>. Electrons and holes in a superconductor can be seen as a particle and antiparticle pair. At zero energy, there is no difference between particles and holes, which reminds us the notion of a Majorana particle. MBS appear bounded to a defect such as a domain wall or a vortex in a superconductor. MBS are topologically protected states, so they are decoherence-free degrees of freedom as the edge states of graphene. MBS have been proposed to be topological qubits in a topological quantum computer. Nowadays, the understanding and development of a platform for MBS is an active research area for experimental and theoretical physicists<sup>9 10 2 11</sup>.

The initial proposals about Majorana particles were based on midgap excitations of  $p$ -wave superconductors. Quasi particles with non-Abelian statistics found in the fractional quantum Hall (FQH) were investigated<sup>12</sup> as possible candidates for MBS. In 2000, Alexei Kitaev proposed a toy model for a one dimensional system with MBS at the end points<sup>13</sup>. It was simpler than previous ones in two or three dimensions. The Kitaev model describes a nanowire deposited on top of a 3d superconductor. By proximity effects, superconductivity is induced on the nanowire. It is a toy model since electron is considered spinless. Such spinless electrons can be built in a  $p$ -wave superconductor, but is a really fragile state<sup>8</sup>. Since there are two ends to the Kitaev wire, MBS come in pairs. Such states lie in the middle of the superconducting gap, and are degenerate. This subspace is called as a topologically protected degenerate low-energy manifold. This means these particles are immune to local perturbations.

The Kitaev model is a simple and interesting way to describe the physics of MBS, particles that are exciting candidates for quantum computation. Nevertheless, a more realistic proposal is necessary. Recent experimental developments have attracted major interest on this topic<sup>14</sup>. In fact, Kane and Fu showed that a simple s-wave superconductor in proximity to the surface of a strong topological insulator (TI) hosts MBS as edge states. These

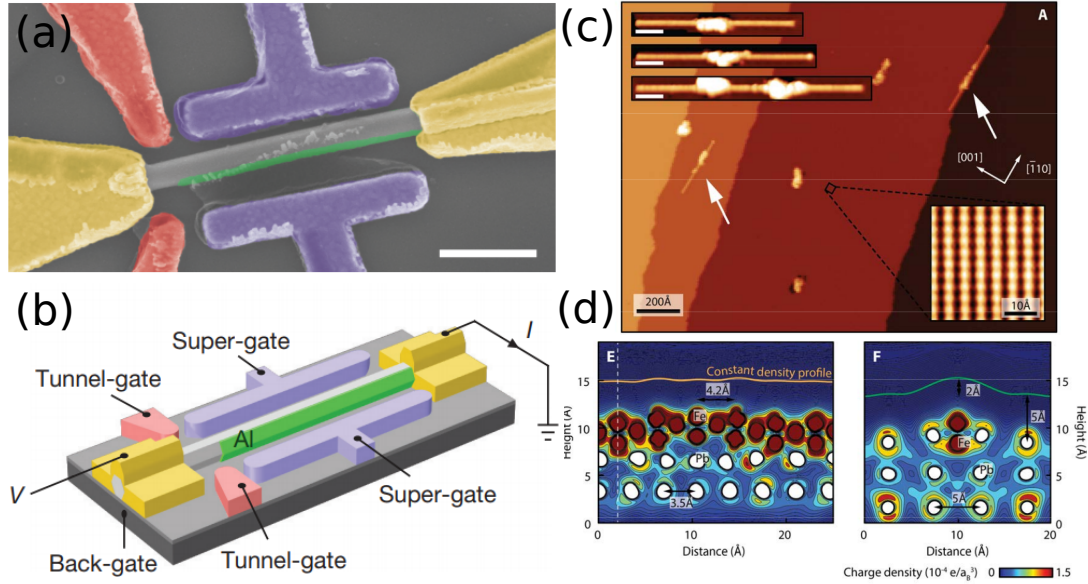


Figure 1.1: Some physical realizations of devices with MBS. (a) False-colour scanning electron micrograph of device A. Image and caption taken from Zhang, et. al. (2018)<sup>1</sup>. (b) Schematics of device A. Image taken from literature<sup>1</sup>. (c) Schematic of the proposal for Majorana quasiparticle realization and detection: a ferromagnetic atomic chain is placed on the surface of strongly spin-orbit coupled superconductor and studied using scanning tunneling microscopy. Image and caption taken from Nadj, et. al. (2015)<sup>2</sup>. (d) Model calculation of the local density of states (LDOS) of the atomic chain embedded in a 2D superconductor. Image and caption taken from literature<sup>2</sup>.

MBS are located at the edges of a 2D surface. This is important because it is much easier to use s-wave than p-wave superconductivity. Spin-orbit (SO) interaction and magnetic fields are used to build an effective spinless system. In Fig. 1.1 one can observe the main experimental realizations. A recent and novel proposal is based on semiconducting nanowires, (a) and (b), in proximity to a superconductor<sup>9,15</sup>. This proposal is widely used nowadays because its experimental achievements<sup>16–20</sup>. Other proposals rely on magnetic systems<sup>2,21</sup>, (c) and (d), that show interesting properties such as robustness against disorder and highly localized end states<sup>22–25</sup>.

The concept of a topological qubit has gained relevance in the field of quantum computation. In fact, according to C. Beenaker<sup>9</sup> it represents a "fundamentally new way to store and manipulate quantum information". MBS's can be used to build qubit states, that is, a linear superposition of two quantum states which logically correspond to zero and one. A qubit made of MBS is decoherence free since the operations that produce errors, such as a bit-flip, cannot happen for a single MBS, but for paired MBS<sup>10</sup>. The topological protection is deeply related to the existence of a non-zero gap for quasiparticle excitations<sup>9</sup>. Degenerate states in the middle of the gap, at zero energy, live in a topologically protected subspace. The set of operations that can be applied to on these qubits corresponds to the braid group<sup>14</sup>, which represents all the possible braiding operations, *i.e.* moving MBS around each other. However,

such group cannot be used to build a universal quantum computer<sup>10</sup>. In any case, MBS offer the realization of a decoherence-free quantum computing platform. Finally, the measurement process of a topological qubit can be done by fusing the qubits together. MBS can be fused together and the resulting state can be measured. The result depends on the transformations, braiding process, applied to the qubits.

The promising possibilities of MBS has caused a lot of theoretical and experimental research in this field. In fact, there are several proposals to build a device that hosts MBS's<sup>15</sup>. The nature of MBS is present as a signature in the transport and thermodynamic properties of the device<sup>9</sup>. The presence of MBS can be experimentally confirmed by the following measurements:

- **Half-Integer Conductance Quantization:** Tunneling spectroscopy can be used to probe the states of the system. Resonant tunneling to the midgap states of the system shows a  $2e^2/h$  quantization of the conductance<sup>9</sup>. This tunneling process produces a current that flows from non-interacting Fermi leads to the grounded superconducting system with MBS's<sup>26,27</sup>. The system is similar to the Half-Integer Quantum Hall Effect of graphene<sup>28</sup>.
- **Nonlocal Tunneling:** The overlapping of the wavefunction of the MBS's in the wire can produce nonlocal tunneling<sup>9,29</sup>. It is a conduction process that involves both MBS's. It is not possible without these quasiparticles. Then, it allows one to determine its presence.
- **$4\pi$ -periodic Josephson junction:** The usual Josephson effect<sup>30</sup> acquires a new feature if there are MBS in the system<sup>15</sup>. Since the presence of MBS opens a new channel for single electrons<sup>9</sup> in the superconductor, that only allows paired electrons (Cooper pairs), the periodicity of the system is affected. Such phenomena can be detected<sup>31,32</sup> and used to determine the presence of MBS's. Several setups for this device have been developed. Some experiments<sup>31-33</sup> found a Josephson effect happening at the surface of a 3D topological insulator.

In summary, MBS are quasiparticles with non-Abelian statistics that can be used as topological qubits. MBS are topologically protected, that is, they are decoherence free degrees of freedom which are affected only by non-local operations. The Kitaev model<sup>10</sup> was the first one-dimensional system with MBS theoretically proposed. Further developments<sup>14</sup> were necessary to make realistic proposals of such toy model. The most studied realizations of MBS are based on semiconductor heterostructures with strong SO, and magnetic systems are a promising candidate for new MBS platforms.

## 1.1 Problem Statement

A recent proposal describes a ferromagnetic atomic chain in proximity to and s-wave superconductor with strong SO as a candidate for hosting MBS<sup>2,22</sup>. It describes a three-layer zigzag chain made of Fe atoms embedded into a superconducting Pb (110) surface. Density Functional Theory (DFT) simulations<sup>2</sup> based on the projector augmented wave pseudopotential using the Viena Ab-Initio simulation package (VASP)<sup>34</sup> show that this structure is the most stable configuration of the system. However, no analytic solution of the microscopic model is given. It would allow one to manipulate properties of MBS by changing the chain's geometric configuration and study the stability of MBS

in different configurations. The space of parameters of our system in the topological and trivial regime, which are defined later, can be studied in a realistic set of parameters and compared with previous results.

## 1.2 General and Specific Objectives

- Based on the literature, develop a one-dimensional analytic tight binding model with MBS at the wire's endings.
  - Starting from a geometrical description of the system, build all the interactions that are present in state-of-the-art proposals using analytical methods.
- Determine the range of parameters that generate topological states that correspond to physical states in the device.
  - Analyze the nature of the eigenstates in a finite system with different parameter configurations.
- Based on the microscopic details of the problem, propose how to experimentally manipulate the proximity induced interactions.
  - Determine which microscopic parameters maximize a particular interaction.
  - Determine how such parameters are related to the topological properties of the system.

In section 2 we describe the theoretical basis required to work on this problem understanding the underlying physics. As a reference model for the TB development, we use Graphene. We use partitioning methods to discuss SO effects of graphene. Finally, we discuss the Kitaev model. The required theory is detailed in the appendices. After setting up the background, our model is introduced in section 3. Then, we build an effective Hamiltonian which contains MBS as end modes. The topological character of the system and the MBS are analyzed. Finally, a discussion is performed in order to understand the physics derived from our model and its relevance to the field.

# Chapter 2

## Methodology

### 2.1 Slater Koster Integrals

Solids are made of atoms, which are described approximately by hydrogenic wavefunctions and their interaction is a perturbation. In quantum mechanical problems, one often calculate inner products, which are written in the basis of hydrogenic wavefunctions, of the form  $\langle \phi_A(\mathbf{r} - \mathbf{R}_{Aj}) | \mathcal{H} | \phi_B(\mathbf{r} - \mathbf{R}_{Bi}) \rangle$ , that can be complicated to solve exactly. Slater and Koster developed an approximation<sup>35</sup> where the magnitude of such product depends on the overlap of the wavefunctions in a given geometrical configuration. Considering only two-center interactions, the integrals became a combination of overlapping parameters that depends on the director cosines defined in Fig. 2.2.

Considering the vector that connects the two atoms,  $\mathbf{R}_j - \mathbf{R}_i$ , as the molecular axis, its overlap will be a combination of  $\sigma$ ,  $\pm\pi$  and  $\pm\delta$  bonding (Fig. 2.3) depending on wavefunction overlap parallel and perpendicular with respect to the bond axis. Slater Koster table capture the geometrical relations of the two center integrals. Such formulas preserve the symmetry of the atomic wavefunctions, and reduce the number of parameters. Systems with interesting geometries, such as surfaces, atomic chains, or even a DNA molecule, can be analytically studied using Slater-Koster parameters.

The overlapping parameters depends on the orbital basis and bonding between the atoms and can be observed in Fig. 2.1. The  $\sigma$  bonding is the strongest part of a covalent bond where electrons are shared by two atoms. The parameters that represent this interaction are:  $V_{\mu\nu\sigma}$ , where  $\mu, \nu$  can be a particular orbital  $s, p, \text{ or } d$ . The  $\pi$  bonding corresponds to the lateral overlap of orbitals. Their overlapping parameters are:  $V_{\mu\nu\pi}$  corresponding with the previous definition. A graphical representation of the  $\pi$  and  $\sigma$  bonding can be appreciated in Fig. 2.3.

The director cosines are shown in Fig. 2.2 and are defined as,

$$l = \cos \alpha, \quad m = \cos \beta, \quad n = \cos \gamma. \quad (2.1)$$

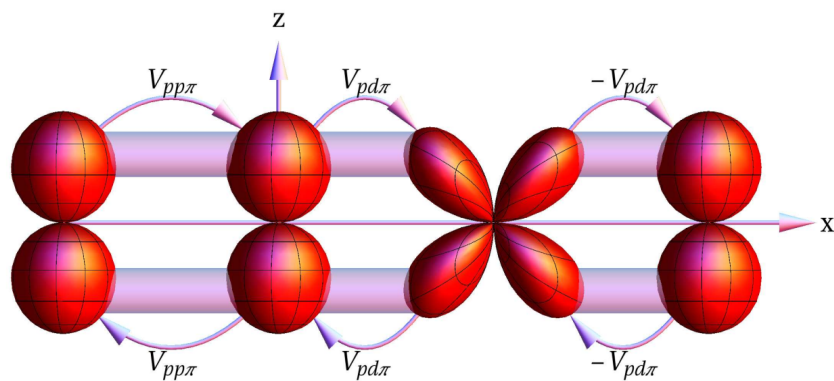


Figure 2.1: Sketch of a linear chain of artificial atoms with two possible states:  $p_z$  and  $d_{xz}$  orbitals. The parameter  $V_{pp\pi}$  describes hopping between the neighboring  $p$  orbitals and  $V_{pd\pi}$  between the  $p$  and  $d_{xz}$  orbitals, where the  $\pi$  bondings are represented by tunnels. Image and caption taken from the literature<sup>3</sup>.

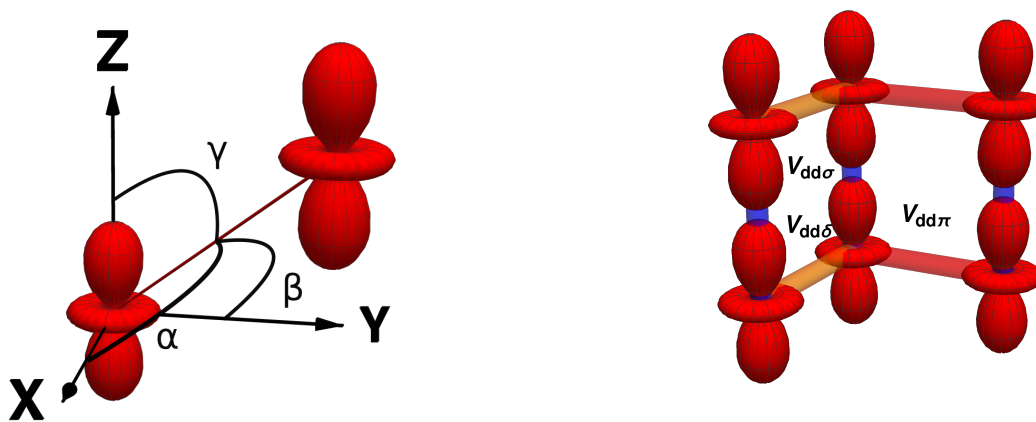


Figure 2.2: Two  $d_{z^2-r^2}$  orbitals connected by a vector (red) in the XYZ coordinate system. The angles with respect to each axis are  $\alpha$ ,  $\beta$  and  $\gamma$ .

Figure 2.3: SK parameters of the  $\sigma$  and  $\pi$  bonding in the  $d_{z^2-r^2}$  orbital. Frontal (blue) overlap corresponds to  $\sigma$  sector. Lateral (red) overlap corresponds to  $\pi$  sector. A bonding along a direction perpendicular to  $\sigma$  and  $\pi$  corresponds to the  $\delta$  bonding.

## 2.2 Tight Binding Model of Monolayer Graphene

The first TB model for a hexagonal honeycomb lattice of atoms was solved by Wallace<sup>36</sup>. He was describing the electronic structure of graphite for a single layer of carbon atoms. It can be described using the TB method described in section B. A low energy Dirac Hamiltonian can be derived in the vicinity of the Fermi level to describe electrons in this material<sup>4,37</sup>. As will be derived, it hosts Dirac-like chiral massless fermions. This is a remarkable model because it describes a relativistic dispersion relation in a condensed matter context. In spite of being described for the first time in the 40's. It was revived theoretically in 2016 with the Kane and Mele<sup>38</sup> proposal of topological insulators. Nowadays, it is an active area of research experimentally and theoretically<sup>39 28 40</sup>.

Consider the lattice is shown in Fig. 2.4. The atoms at each lattice point are carbon atoms. Carbon has six electrons, two of them well bound to carbon. In this structure, three electrons in the orbitals  $|2s\rangle, |2p_x\rangle, |2p_y\rangle$ , participate in the bonds between atoms. They represent the so called " $\sigma$ -structure" of graphene. The remaining electron is in the  $|2p_z\rangle$  orbital. It represents the so called " $\pi$ -structure". Electron transport will be determined by the dynamics of the unpaired electron in the  $|2p_z\rangle$  orbital. Therefore, we are interested in solving the  $\pi$ -subspace to a very good approximation<sup>4</sup>. As a first approximation, we will ignore the  $\sigma$ -subspace. This model does not consider  $\sigma - \pi$  interactions caused by fluctuations of the flat structure.

### 2.2.1 Geometrical Structure

To describe graphene as a honeycomb lattice of carbon atoms, let us start by describing its real space structure. As is shown in Fig. 2.4, the AB atomic basis is the primitive cell that will be replicated periodically. The basis vectors to translate this basis are given by,

$$\mathbf{a}_1 = \frac{a}{2}(\mathbf{e}_x + \sqrt{3}\mathbf{e}_y) \quad \mathbf{a}_2 = \frac{a}{2}(\mathbf{e}_x - \sqrt{3}\mathbf{e}_y), \quad (2.2)$$

where  $e_x$  and  $e_y$  are the unit vectors along  $x$  and  $y$  directions respectively and  $a$  is the lattice parameter shown in Fig. 2.4. The representation in reciprocal space can be obtained by transforming<sup>41</sup> the basis vectors. That is, they must obey  $\mathbf{a}_i \cdot \mathbf{b}_j = 2\pi\delta_{ij}$ . The basis vectors in reciprocal space are given by:

$$\mathbf{b}_1 = \frac{2\pi}{a}(\mathbf{e}_x + \frac{1}{\sqrt{3}}\mathbf{e}_y), \quad \mathbf{b}_2 = \frac{2\pi}{a}(\mathbf{e}_x - \frac{1}{\sqrt{3}}\mathbf{e}_y). \quad (2.3)$$

### 2.2.2 Reciprocal Space Representation

To obtain the reciprocal space Hamiltonian, we use Bloch's theorem and address the generalized eigenvalue problem for a non-orthogonal basis. The general formalism is developed in B. We want to know the dispersion relation of this system. Then, we must solve Eq. B.11. We have to find the elements of H and S matrices. To obtain H, see Eq. B.13 and Eq. B.15. They are given by,

$$H = \begin{pmatrix} \epsilon_\pi & -\gamma_o f(\mathbf{k}) \\ -\gamma_o f^*(\mathbf{k}) & \epsilon_\pi \end{pmatrix}, \quad S = \begin{pmatrix} 1 & s_o f(\mathbf{k}) \\ s_o f^*(\mathbf{k}) & 0 \end{pmatrix} \quad (2.4)$$

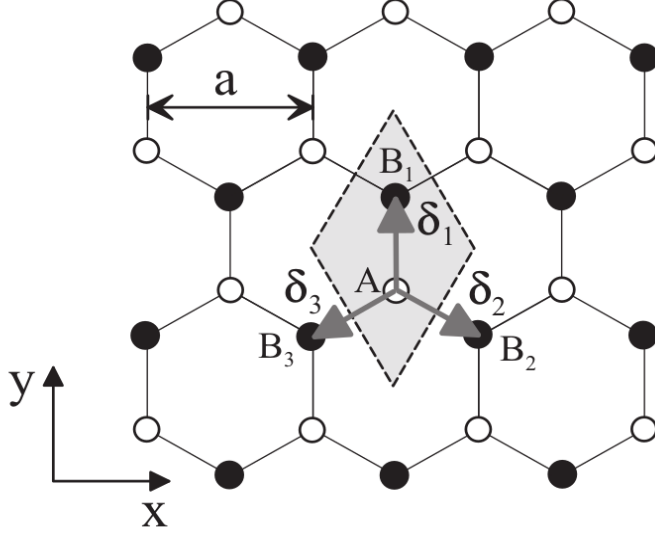


Figure 2.4: Geometrical structure of graphene taken from the book *Graphene Nanoelectronics* by McCann<sup>4</sup>. Graphene lattice has two inequivalent atoms called A (white) and B (black). The area in gray represents the primitive cell of graphene that contains a pair of atoms A and B. The lattice parameter is  $a$ . The nearest neighbor vectors that connect A with the three closest B atoms are labeled  $\delta$ .

The vectors  $\delta_i$  connect the A atom to its 3 nearest neighbor B atoms. They are indicated in Fig. 2.4. They are given by:

$$\delta_1 = \frac{a}{\sqrt{3}}\mathbf{e}_y, \quad \delta_2 = -\frac{a}{2}\mathbf{e}_x - \frac{a}{\sqrt{3}}\mathbf{e}_y, \quad \delta_3 = \frac{a}{2}\mathbf{e}_x - \frac{a}{\sqrt{3}}\mathbf{e}_y. \quad (2.5)$$

Using TB theory, the Fourier components in reciprocal space with the same magnitude for  $|p_z\rangle$  orbitals are given by,

$$f(\mathbf{k}) = e^{iak_y/\sqrt{3}} + e^{-iak_x/2}e^{-iak_y/2\sqrt{3}} + e^{iak_x/2}e^{-iak_y/2\sqrt{3}},$$

where  $k_i$ 's are the crystal momentum components. The expression can be rewritten as,

$$f(\mathbf{k}) = e^{iak_y/\sqrt{3}} + 2e^{-iak_y/2\sqrt{3}} \cos(ak_x/2). \quad (2.6)$$

This expression is used to build the  $H$  and  $S$  matrix of the TB theory as shown in Eq. 2.4. To solve the system we have to use the generalized eigenvalue problem, detailed in the appendix B, which is,

$$\det(H - SE) = 0, \quad (2.7)$$

where  $E$  is the energy. Explicitly, it is given by,

$$\det \begin{pmatrix} \epsilon_\pi - E & -(\gamma_0 + Es_0)f(\mathbf{k}) \\ -(\gamma_0 + Es_0)f^*(\mathbf{k}) & \epsilon_\pi - E \end{pmatrix} = 0. \quad (2.8)$$

Let us consider that the energy of the  $\pi$  orbitals is the reference energy of the system, *i.e.*  $\epsilon_\pi = 0$ . The resulting dispersion relation is given by,

$$\begin{aligned} E^2 - (Es_0 + \gamma_0)|f(\mathbf{k})|^2 &= 0, \\ E_\pm(1 \mp s_0) &= \pm\gamma_0|f(\mathbf{k})|, \\ E_\pm &= \pm \frac{\gamma_0|f(\mathbf{k})|}{1 \mp s_0}. \end{aligned} \quad (2.9)$$

The dispersion relation in the first Brillouin zone is shown in Fig. 2.5. Clearly, there are two bands that correspond to bound and mobile electrons. If one considers  $k_y = 0$ , then one finds the dispersion relation shown in Fig. 2.6 where one can find a band crossing at the K point. Also, if one observes closer (inset of Fig. 2.6) a linear structure that corresponds to the so-called Dirac cones.

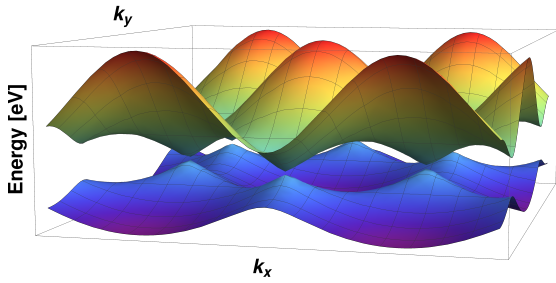


Figure 2.5: 3D spectrum of a graphene monolayer. Electrons move along  $k_x$  and  $k_y$  within the first Brillouin zone.

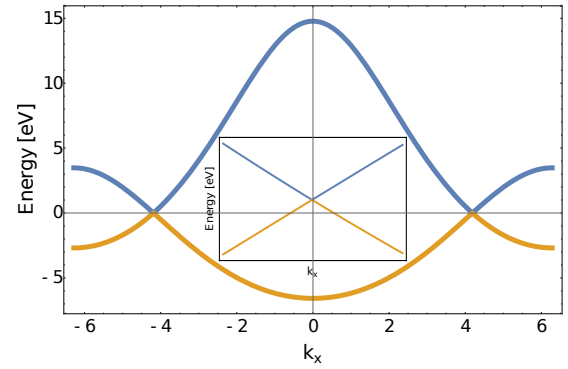


Figure 2.6: Cut of the graphene spectra along  $k_y = 0$ . At the point K two Dirac cones can be appreciated. Inset: A zoom of the Dirac cone at K is shown.

### 2.2.3 Effective Hamiltonian at the K point

First, there are two inequivalent points in the first Brillouin zone labeled  $K_\pm$ . They are described by,

$$\mathbf{K}_\pm = \pm \frac{1\pi}{3a} \mathbf{e}_x. \quad (2.10)$$

Replacing that point in Eq. 2.6, we have that,

$$f(\mathbf{K}_\pm) = e^0 + e^{\pm i2\pi/3} + e^{\mp i2\pi/3} = 0. \quad (2.11)$$

At these points, there is no coupling between A and B sublattices because  $f(k) = 0$ . Then, there is a degeneracy exactly at the K point. To describe the behaviour of fermions in the vicinity of the Fermi level, so we define a momentum vector that is centered at K,

$$\mathbf{p} = \hbar\mathbf{k} \pm \hbar\mathbf{K}, \quad |\mathbf{p}| \ll 1. \quad (2.12)$$

We expand Eq. 2.6 for  $\mathbf{p} \approx 0$ . Our expansion remains valid as long as we remain close to  $\mathbf{K}_\pm$ , and it is shown in Fig. 2.6. That is,  $|\mathbf{p}|a/\hbar \ll 1$ . Considering only linear terms in momentum,

$$f(\mathbf{p}) = e^{iap_y/\sqrt{3}} + 2e^{-iap_y/2\sqrt{3}} \cos\left(\frac{ap_x}{2} \pm \frac{2\pi}{3}\right) \approx \left(1 + \frac{ap_y}{\sqrt{3}}\right) + 2\left(1 - \frac{ap_y}{\sqrt{3}}\right)\left(-\frac{1}{2} \mp \frac{a\sqrt{3}p_x}{4}\right),$$

expanding the momentum to lowest order we find,

$$f(\mathbf{p}) \approx -\frac{\sqrt{3}a}{2} (\pm p_x + ip_y), \quad (2.13)$$

then, the direct integral matrix reads,

$$H_\pm = \frac{\sqrt{3}a\gamma_0}{2} \begin{pmatrix} 0 & \pm p_x - ip_y \\ \pm p_x + ip_y & 0 \end{pmatrix} \quad (2.14)$$

where  $\gamma_0$  is the overlap parameter. Immediately, we recognize that it can be rewritten in terms of the Pauli matrix in sublattice space. Its eigenstates represent the relative amplitude of an electron at each atom of the sublattice. This degree of freedom has the same form as that of the 1/2-spin. Then, we call it a pseudospin. Written in this basis, the Hamiltonian can be rewritten as,

$$H_\pm = v\hat{\sigma} \cdot \hat{\mathbf{n}} \quad (2.15)$$

where  $v = \frac{\sqrt{3}a\gamma_0}{2}$ , and  $\hat{\sigma} = (\sigma_x, \sigma_y, \sigma_z)$  are the usual Pauli matrices, and  $\hat{\mathbf{n}} = (\pm p_x, p_y)$  is the momentum vector. This is the Dirac Hamiltonian for massless fermions that move at velocity  $v$ . The dispersion relation is shown in the inset of Fig. 2.6. The Dirac dispersion relation is,

$$E_\pm = \pm v|\mathbf{p}|. \quad (2.16)$$

We call this the Dirac dispersion since it is linear with respect to momentum, as in the case of the Dirac equation. The states that are described by this model correspond to the eigenvectors of Eq. B.13. It is straightforward to derive that,

$$|\psi_\pm\rangle = \frac{1}{\sqrt{2}} \begin{pmatrix} 1 \\ \pm e^{\pm i\phi} \end{pmatrix} e^{i\mathbf{p}\cdot\mathbf{r}}. \quad (2.17)$$

### 2.2.4 Chirality and Polarization

Since the Hamiltonian represents the energy of a system and is hermitian, it is conserved. Also, any operator that commutes with the Hamiltonian represents a conserved quantity. It is equivalent to say that they have a common set of eigenstates. From this fact, two important consequences are derived for graphene. Since  $H = \hbar v \hat{\sigma} \cdot \mathbf{p}$ , then,  $H|\psi_\pm\rangle = \pm v|\psi_\pm\rangle$ . It means that the projection of the spin onto the momentum is conserved and can only be  $\pm 1$ .

Consider the polarization of the pseudospin as  $\langle \sigma \rangle = (\langle \sigma_x \rangle, \langle \sigma_y \rangle, \langle \sigma_z \rangle)$ . Obtaining the expectation value of each component using the states of Eq. 2.17, we obtain that,

$$\langle \sigma_x \rangle = \frac{1}{2} \begin{pmatrix} 1 & \pm e^{i\mp\phi} \end{pmatrix} \begin{pmatrix} 0 & 1 \\ 1 & 0 \end{pmatrix} \begin{pmatrix} 1 \\ \pm e^{\pm i\phi} \end{pmatrix} = \cos(\phi), \quad (2.18)$$

$$\langle \sigma_y \rangle = \sin(\phi), \quad (2.19)$$

$$\langle \sigma_z \rangle = 0, \quad (2.20)$$

the phase of the state rotates the momentum by an angle  $\phi$ . Consider an adiabatic transformation of the phase  $\phi = 0 \rightarrow 2\pi$  along a closed contour in the complex plane which is identical for both sublattices. The phase acquired by the wavefunction after such transformation is of  $\pi$ . This is the so-called Berry phase<sup>42</sup>. It reflects the rotation of the pseudospin degree of freedom<sup>4</sup>.

Second, as long as the sublattice symmetry is maintained, *i.e.* no interactions that treats different A from B, chirality is conserved. We are interesting in obtaining the probability of a scattering amplitude that depends on the final angle. Considering  $\phi = 0$  as the direction of motion, the scattering amplitude is proportional to

$$w(\phi) = |\langle \psi_{\pm}(\phi) | \psi_{\pm}(0) \rangle|^2 = \cos^2(\phi/2). \quad (2.21)$$

For backscattering processes,  $\phi = \pi$ , the scattering amplitude is zero. Backscattering is not allowed in graphene because the direction of the momentum cannot be reversed without also changing the pseudospin. It is an important concept when discussing anisotropic scattering at potential barriers in graphene and it is related to the topological properties of the system.

Although we have described the behaviour of relativistic fermions in a graphene layer, there are plenty of effects that we are ignoring. An example would be the Spin-Orbit(SO) interaction of the graphene. It arises from interactions with electrons from the  $\sigma$ -sector. In fact, to solve this problem, we need to diagonalize the full Hamiltonian that includes both  $\sigma$  and  $\pi$  subspaces. There are several ways to solve the full problem. In the next section we will discuss one of them.

## 2.3 Matrix Perturbation Theory: The Band Folding Method

There are different ways to solve the general problem of quantum mechanics, *i.e.* the secular equation. One can approach by directly finding the solution of the differential equation, or rather find a different representations that simplifies the problem. A different approach is obtained by direct substitution in an energy-dependent Hamiltonian. Let us start by considering the time-independent Schrodinger equation,

$$H\Psi = E\Psi. \quad (2.22)$$

Let us consider that  $H$  describes two kinds of eigenstates  $\alpha$  and  $\beta$ , which are weakly coupled to each other. Then, the secular equation, in matrix form, can be written as,

$$\begin{pmatrix} H_{\alpha\alpha} & H_{\alpha\beta} \\ H_{\alpha\beta}^\dagger & H_{\beta\beta} \end{pmatrix} \begin{pmatrix} v_\alpha \\ v_\beta \end{pmatrix} = E \begin{pmatrix} v_\alpha \\ v_\beta \end{pmatrix}, \quad (2.23)$$

where  $H_{\alpha\alpha}$  and  $H_{\beta\beta}$  are the Hamiltonian of each kind of eigenstates, and  $H_{\alpha\beta}$  is their coupling. Also, the eigenvector is  $\Psi = (v_\alpha \ v_\beta)^T$ , where  $v_\alpha$  and  $v_\beta$  are the eigenvectors of each kind. It can be considered as a set of two coupled equations for the eigenvalues and eigenvectors of the system,

$$H_{\alpha\alpha}v_\alpha + H_{\alpha\beta}v_\beta = Ev_\alpha \quad H_{\alpha\beta}^\dagger v_\alpha + H_{\beta\beta}v_\beta = Ev_\beta. \quad (2.24)$$

From which, we can obtain  $v_\beta$  as,

$$v_\beta = (\mathbf{1}E - H_{\beta\beta})^{-1} H_{\alpha\beta}^\dagger v_\alpha, \quad (2.25)$$

by substitution, the equation for  $v_\alpha$  is,

$$\left( H_{\alpha\alpha} + H_{\alpha\beta} (\mathbf{1}E - H_{\beta\beta})^{-1} H_{\alpha\beta}^\dagger \right) v_\alpha = Ev_\alpha. \quad (2.26)$$

Then, we consider an expansion for the inverse matrix in the previous expression. For that, we assume that  $E \ll H_{\beta\beta}$ , then

$$\frac{1}{E - H_{\beta\beta}} = \frac{-1}{H_{\beta\beta}} \frac{1}{1 - \frac{E}{H_{\beta\beta}}} = \frac{-1}{H_{\beta\beta}} \left( 1 + \frac{E}{H_{\beta\beta}} + \dots \right) \quad (2.27)$$

After substitution in the previous expression and reordering terms, we obtain,

$$\left( H_{\alpha\alpha} - H_{\alpha\beta} \frac{1}{H_{\beta\beta}} H_{\alpha\beta}^\dagger \right) v_\alpha = \left( 1 + H_{\alpha\beta} \frac{1}{H_{\beta\beta}^2} H_{\alpha\beta}^\dagger \right) E v_\alpha. \quad (2.28)$$

Let's define  $S = \left( 1 + H_{\alpha\beta} (H_{\beta\beta}^{-1})^2 H_{\alpha\beta}^\dagger \right)$ , and  $\Phi = S^{1/2} v_\alpha$ . Then,

$$S^{-1/2} \left( H_{\alpha\alpha} + H_{\alpha\beta} (\mathbf{1}E - H_{\beta\beta})^{-1} H_{\alpha\beta}^\dagger \right) S^{-1/2} \Phi = E \Phi. \quad (2.29)$$

The problem of the two subspaces has been reduced to an effective problem of a single subspace, where the second subspace is included in the effective Hamiltonian in a perturbatively manner. That is,

$$H_{eff} \Phi = E \Phi, \quad (2.30)$$

where,

$$H_{eff} = S^{-1/2} \left( H_{\alpha\alpha} + H_{\alpha\beta} (\mathbf{1}E - H_{\beta\beta})^{-1} H_{\alpha\beta}^\dagger \right) S^{-1/2} \quad (2.31)$$

This method has been widely used to study tight-binding Hamiltonians<sup>43</sup>. As an example in graphene, the conduction occurs in the pi structure made of  $p_z$  orbitals, but the spin orbit interaction occurs in the  $p_x$  and  $p_y$  that correspond to the sigma structure. Such spin interactions can be included effectively using the band folding formulation, as in the literature.

## 2.4 Spin Orbit in Graphene

Spin orbit in graphene was introduced by Kane and Mele through a symmetry argument<sup>38</sup>. The Slater Koster approach, on the other hand, allows to derive the same term plus the microscopic coupling. Here we rederive the SI coupling for graphene involving  $p_z$  and  $d$  orbitals as found by Kanschuh et al. Using the methods described in this section, we want to address the problem of the SO splitting in graphene. Since the SO interaction does not connect  $|p_z\rangle$  states directly, our previous model cannot describe this feature. To include SO interaction into the problem,  $|d\rangle$  orbitals are included for first order in the SO coupling. Particularly,  $\{|zx\rangle, |yz\rangle\}$ . Also, spin states are included as  $\{|\uparrow\rangle, |\downarrow\rangle\}$ . The SO interaction is discussed in Section A, and the SO matrix elements are derived for d-orbitals. Recalling the matrix elements,

$$\langle yz \uparrow | H_{SO} | zx \uparrow \rangle = i\lambda_d, \quad \langle yz \downarrow | H_{SO} | zx \downarrow \rangle = -i\lambda_d, \quad (2.32)$$

where  $\lambda_d$  is the magnitude of the SO coupling for  $d$  orbitals. The full Hamiltonian of the system includes  $\{|p_z\rangle, |zx\rangle, |yz\rangle\}$  as the orbital basis, the spin basis, and the sublattice basis. The problem can be rewritten as Eq. E.1. That is,

$$H = \begin{pmatrix} H_{pp} & H_{pd} \\ H_{pd}^\dagger & H_{dd} \end{pmatrix} \quad (2.33)$$

where the diagonal components corresponds to the pure Hamiltonian of the  $p$  and  $d$  subspaces respectively, and the non diagonal terms represent the  $p - d$  coupling. We are interested in effectively describing the subspace  $H_{pp}$ . It describes the conduction electrons while the  $H_{dd}$  subspace includes the SO interaction.  $H_{dd}$  is folded into  $H_{pp}$  to create an effective model. First of all, we need to find a basis such that  $H_{dd}$  is diagonal<sup>44</sup>. Let,

$$|\Psi_\pm\rangle = \frac{1}{\sqrt{2}}(|\uparrow\rangle \pm |\downarrow\rangle) \quad (2.34)$$

$$|d_\pm\rangle = \frac{1}{\sqrt{2}}(|yz\rangle \pm i|zx\rangle) \quad (2.35)$$

The basis that we consider for the d-orbitals is given by the combinations of Eq. 2.34 and Eq. 2.35. That is,

$$|d_1\rangle = |\Psi_-\rangle \otimes |d_-\rangle \quad (2.36)$$

$$|d_2\rangle = |\Psi_+\rangle \otimes |d_+\rangle \quad (2.37)$$

$$|d_3\rangle = |\Psi_+\rangle \otimes |d_-\rangle \quad (2.38)$$

$$|d_4\rangle = |\Psi_-\rangle \otimes |d_+\rangle \quad (2.39)$$

We are going to use this basis to build the Hamiltonian matrix for the d orbitals,  $H_{dd}$ . Note that the  $H_K$  accounts for hopping interactions and self-energies while  $H_{SO}$  accounts for spin interactions of Eq. 2.32. The Hamiltonian that describes the system is the following:

$$H = H_K + H_{SO} \quad (2.40)$$

To build the Hamiltonian matrix we need to take the matrix elements in the given basis. We quote the results of Boykin<sup>44</sup>, that is,

$$H_{dd} = \begin{pmatrix} E_d - \lambda_d & 0 & 0 & 0 \\ 0 & E_d - \lambda_d & 0 & 0 \\ 0 & 0 & E_d + \lambda_d & -2U_{dd} \\ 0 & 0 & -2U_{dd} & E_d - \lambda_d \end{pmatrix} \quad (2.41)$$

where  $E_d$  is the energy of the  $d$  orbitals, and  $U_{dd}$  is the SK overlap between  $xz$  and  $yz$  orbitals. In the same manner, the coupling matrix between  $p$  and  $d$  is,

$$H_{pd} = \begin{pmatrix} -iU_{pd} & -iU_{pd} & 0 & 0 \\ -iU_{pd} & iU_{pd} & 0 & 0 \end{pmatrix} \quad (2.42)$$

where  $U_{pd}$  is the Slater Koster matrix element between  $d$  and  $p$  orbitals that are responsible for creating paths involving SO interaction. We will use Eq. E.20 to obtain the effective diagonal subspace for the  $|p_z\rangle$  orbitals. The effective subspace is,

$$H_{pp} = \begin{bmatrix} E_p + h_+ & h_- \\ h_- & E_p + h_+ \end{bmatrix} \quad (2.43)$$

where,

$$h_{\pm} = -U_{pd}^2 \left( \frac{1}{E_d + \lambda_d - E_p} \pm \frac{1}{E_d - \lambda_d - E_p} \right) \quad (2.44)$$

## 2.5 The Kitaev Model

Quantum computing represents a major and exciting topic of quantum physics that can be used to perform incredibly faster some calculations. However, the nature of quantum states is very delicate and loss of phase coherence due to inelastic processes (decoherence) can affect our system before the calculation finish. There are several approaches to address the problem of decoherence, and a very interesting one is to use topologically protected qubits immune to decoherence. In 2001 Alexei Kitaev proposed an alternative model for a one-dimensional system of anyons<sup>10</sup> that can be used to build a decoherence free quantum computer. The basic idea is that a fermionic site can be represented as two Majorana sites. Quantum errors require the interaction between Majorana sites, which can be avoided by controlling the parameters of the system. An isolated Majorana site is immune to any kind of error<sup>13</sup>. Essentially, the idea behind the Majorana transformation is to divide each fermion in two parts<sup>6</sup>, as a complex number can be separated in a real and complex part. In Fig. 2.7 (a) one can observe four fermionic sites, that are represented as a domino to illustrate the Majorana transformation. In this model there are the following interactions: i) on-site chemical potential, ii) spinless superconducting pairing, and iii) hopping. By manipulating the parameters of the system one brought the system into the trivial or the topological phase. The trivial phase is shown in the panel (b) of Fig. 2.7 where the electrons are paired in the normal way, *i.e.* two majoranas correspond to the same fermionic site. The topological phase is shown in the panel (c) of Fig. 2.7 where the majoranas are paired over different fermionic site. At the ends, there are two halves of a fermions that remain separated and localized.

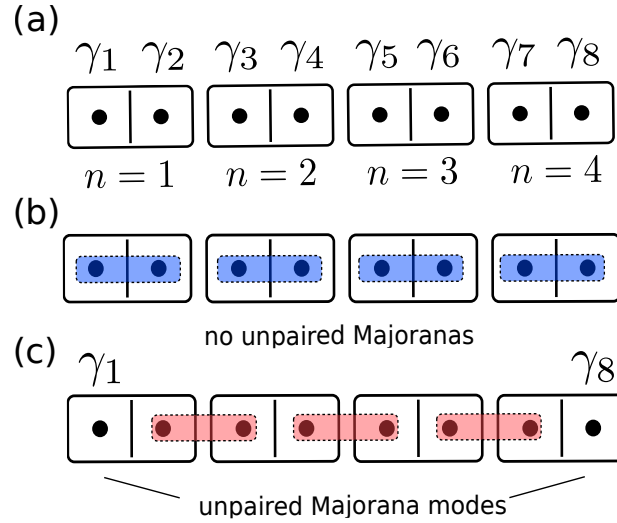


Figure 2.7: Graphical representation of MBS. Each domino represents two Majoranas  $\gamma_n$ . There are 4 electrons, then 8 Majoranas. Image taken from the course *Topology in Condensed Matter*<sup>5</sup>.

### 2.5.1 Majorana Operators

Fermions are constructed by creation and annihilation operators. Usually,  $c_{n\sigma}^\dagger$  creates a single electron with spin  $\sigma$  at site  $n$ . In the Majorana basis, an electronic site is divided in two Majorana sites, and there are two Majorana operators for each fermionic site  $\gamma_n, \gamma_{n+1}$ . That is, for the  $j$ -th electron corresponds the  $2j-1$  and  $2j$  Majorana sites.

$$\gamma_{2n-1\sigma} = c_{n\sigma}^\dagger + c_{n\sigma} \quad i\gamma_{2n} = c_{n\sigma} - c_{n\sigma}^\dagger \quad (n = 1, \dots, N) \quad (2.45)$$

$$\gamma_m = \gamma_m^\dagger \quad \{\gamma_m, \gamma_n\} = 2\delta_{m,n} \quad (m, n = 1, \dots, 2N) \quad (2.46)$$

### 2.5.2 Real Space Kitaev Model

Consider a nanowire deposited on top of a superconductor with an energy gap  $\Delta$ . It has on-site chemical potential  $\mu$  and hopping interaction  $\omega$  between sites. Superconductivity is inherited by proximity effect, from closeby orbitals. Consider  $L \gg 1$ , where  $L$  is the number of sites in the chain. Each site is either empty or occupied by a spinless electron. The Hamiltonian reads,

$$H_K = \sum_n -\omega (c_i^\dagger c_{i+1} + c_{i+1}^\dagger c_i) - \mu c_n^\dagger c_n + \Delta c_j c_{j+1} + \Delta^* c_{j+1}^\dagger c_j^\dagger. \quad (2.47)$$

The Hamiltonian is transformed according to the Majorana transformation shown previously in Sec. 2.5.1. Note that the number of sites is doubled, as well as the dimension of the Hamiltonian. We do a change of basis to each term

as follows,

$$\begin{aligned}
-\omega \sum_i (c_i^\dagger c_{i+1} + c_{i+1}^\dagger c_i) &= -\frac{\omega}{4} \sum_j (\gamma_{2j-1} - i\gamma_{2j})(\gamma_{2j+1} + i\gamma_{2j+1}) + (\gamma_{2j+1} - i\gamma_{2j+2})(\gamma_{2j-1} + i\gamma_{2j}) \\
&= -\frac{\omega}{4} (\gamma_{2j-1}\gamma_{2j+1} + \gamma_{2j+1}\gamma_{2j-1} + 2i(\gamma_{2j-1}\gamma_{2j+2} - \gamma_{2j}\gamma_{2j+1}) + \gamma_{2j}\gamma_{2j+2} + \gamma_{2j+2}\gamma_{2j}) \\
&= -i\frac{\omega}{2} \sum_j (\gamma_{2j-1}\gamma_{2j+2} - \gamma_{2j}\gamma_{2j+1}),
\end{aligned} \tag{2.48}$$

where we have used that  $\{\gamma_n, \gamma_{n+1}\} = 0$ . The term related to the chemical potential is transformed as follows,

$$\begin{aligned}
-\mu \sum_j c_j^\dagger c_j &= -\frac{\mu}{4} \sum_j \gamma_{2j-1}\gamma_{2j-1} + i(\gamma_{2j-1}\gamma_{2j} - \gamma_{2j}\gamma_{2j-1}) + \gamma_{2j}\gamma_{2j} \\
&= -i\frac{\mu}{2} \sum_j \gamma_{2j-1}\gamma_{2j},
\end{aligned} \tag{2.49}$$

where we have used  $(\gamma_i)^2 = 0$ . Finally, the superconducting term is transformed as follows,

$$\begin{aligned}
\Delta \sum_j c_j c_{j+1} + \Delta^* \sum_j c_{j+1}^\dagger c_j^\dagger &= \frac{\Delta}{4} \sum_j (\gamma_{2j-1}\gamma_{2j+1} + i(\gamma_{2j-1}\gamma_{2j+2} - \gamma_{2j}\gamma_{2j+1}) - \gamma_{2j+2}\gamma_{2j}) \\
&\quad + \frac{\Delta^*}{4} \sum_j (\gamma_{2j-1}\gamma_{2j+1} - i(\gamma_{2j-1}\gamma_{2j+2} - \gamma_{2j}\gamma_{2j+1}) - \gamma_{2j+2}\gamma_{2j}) \\
&= \frac{Im[\Delta]}{2} (\gamma_{2j}\gamma_{2j+2} + \gamma_{2j-1}\gamma_{2j+1}) + i\frac{Re[\Delta]}{2} (\gamma_{2j-1}\gamma_{2j+2} + \gamma_{2j}\gamma_{2j+1}).
\end{aligned} \tag{2.50}$$

Setting  $\Delta$  to be real, and agruping terms, the Hamiltonian is written as,

$$H_K = \frac{i}{2} \sum_n -\mu\gamma_{2n-1}\gamma_{2n} - (\omega + \Delta)\gamma_{2n-1}\gamma_{2n+2} - (\omega - \Delta)\gamma_{2n}\gamma_{2n+1}. \tag{2.51}$$

From this Hamiltonian, we can discuss the pairing of the Majorana particles. First of all, note that the majorana operators always appear in pairs. It can pair sites corresponding to a single electron, or sites from different electrons. For instance, let  $\Delta = \omega = 0$ . The Hamiltonian takes the form,

$$H_K = -i\frac{\mu}{2} \sum_n c_{2n-1}c_{2n} \tag{2.52}$$

This pairing correspond to a chain of atoms with  $\mu$  chemical potential in each site. That is, MF's are paired to be isolated electrons. In other regime of parameters, the main contribution may come from terms such as  $c_{2n}c_{2n+1}$  which paires sites belonging to different electrons. Consider  $\omega = -\Delta$  and  $\mu = 0$ . Then the Hamiltonian reads,

$$H_K = -i \sum_{n=1}^{N-1} \Delta\gamma_{2n}\gamma_{2n+1}. \tag{2.53}$$

From this equation we see that the sum does not include the first and the last Majorana sites that are shown in Fig. 2.7 (c). They correspond to two unpaired MF's at each end of the chain. They are included in the Hamiltonian

as zero-energy degenerated states, while all the paired states are outside the gap. MF's are good candidates for TQC because perturbations smaller than the gap does not affect them<sup>13</sup>. In this sense, MF's are robust against local perturbations. The behaviour of the spectra is controlled by the strength of the interactions of the system. In fact, the system can be in a phase with trivial topology, and another phase with non-trivial topology as discussed previously. The transition between these two regimes occurs when zero energy modes appear after a gap closing. The phases are determined by the following relation:

$$\begin{aligned} \text{Topological:} \quad & -2\omega < \mu < 2\omega, \\ \text{Trivial:} \quad & \mu > 2\omega, \quad \mu < -2\omega. \end{aligned} \tag{2.54}$$

We choose parameters inside the topological phase to analyze the spectra and wavefunctions as shown in Fig. 2.8 and Fig. 2.9 respectively. There are two zero energy modes in the middle of the energy gap, and the wavefunctions associated with these states are localized at the ends of the Kitaev wire.

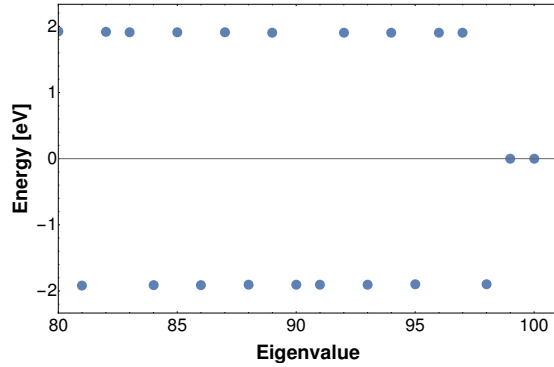


Figure 2.8: Calculated eigenvalues of the Kitaev chain represent the energy of the lowest states. Two zero energy modes can be observed at the end.

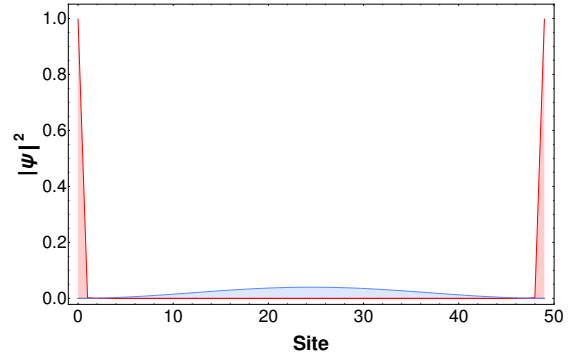


Figure 2.9: Calculated wavefunctions of low-energy states. (Red) Wavefunction of MBS localized at the ends of the wire. (Blue) First mode of the chain.

The closing and reopening of the gap indicates where the phase transition occurs, *i.e.*  $|\mu| = 2\omega$ . At that point, the energy gap becomes zero, and reopens with two zero energy modes as can be observed in Fig. 2.10.

### Hamiltonian in the canonical quadratic form

The real space Kitaev Hamiltonian written in the Majorana basis. It can be written in the canonical quadratic form given by,

$$H = \frac{i}{4} \sum_{l,m} \gamma_l A_{l,m} \gamma_m \quad A_{l,m}^* = A_{l,m}. \tag{2.55}$$

where  $l$  and  $m$  are the index of the rows and columns. The Hamiltonian must be transformed to an anti-symmetric matrix in the Majorana basis in order to be apply to study the topological properties of the system encoded in this form.

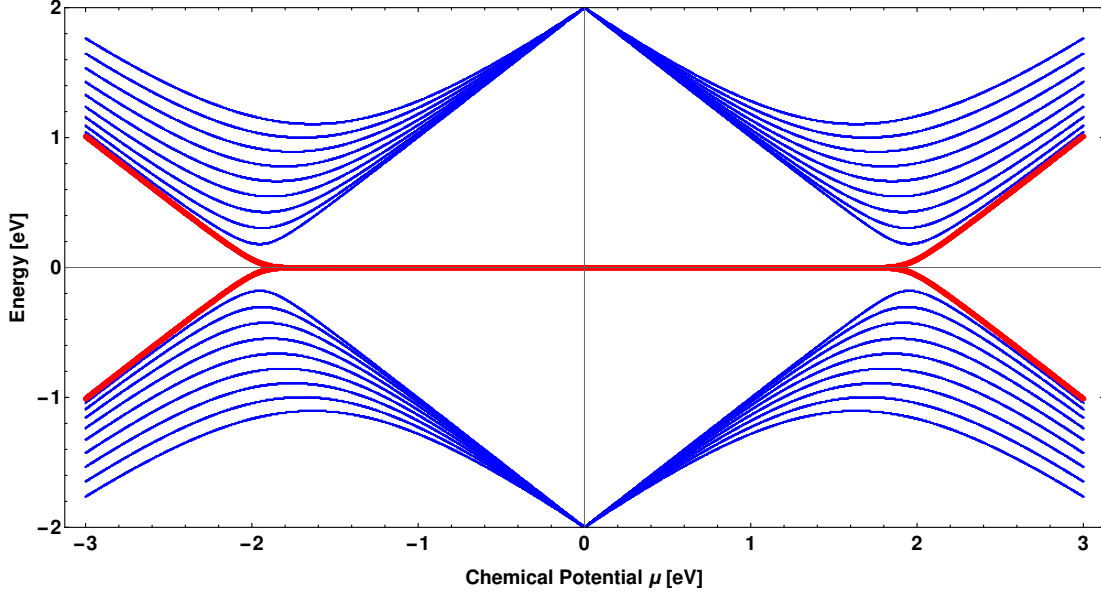


Figure 2.10: Calculated phase transition between trivial and topological phase for the Kitaev wire. Low energy spectra is shown as a function of the chemical potential  $\mu$ . The lowest level is shown in red, and it marks the topological phase when it is at zero energy.

### Considerations about particle-hole symmetry and topologically protected states

The Kitaev Hamiltonian can be written as a Bogoliubov-de-Gennes Hamiltonian, which is of the form  $H = CH_{BdG}C^\dagger$  and  $C = (c_1 \ c_2 \ \dots \ c_n \ c_1^\dagger \ \dots \ c_n^\dagger)^T$  is the vector of creation and annihilation operators. Writing Eq. 2.47 in this form, one finds that,

$$H_{BdG} = - \sum_n \mu \tau_z c_n^\dagger c_n - \sum_n \left( (i\tau_z + i\Delta\tau_y) c_{n+1}^\dagger c_n + H.C. \right), \quad (2.56)$$

where  $\tau_i$ 's corresponds to the Pauli matrices in particle-hole space. The BdG Hamiltonian acts on a new set of states as  $H_{BdG}|\tau\rangle = \pm|\tau\rangle$ , where  $|\tau\rangle$  represents particles and holes. Also,  $H_{BdG}$  has particle-hole symmetry, that is represented as,

$$\mathcal{P}H_{BdG}\mathcal{P}^\dagger = -H_{BdG}, \quad (2.57)$$

where  $\mathcal{P} = \tau_x \mathcal{K}$ , and  $\mathcal{K}$  is complex conjugation. It represents the correspondence between particles and holes, and it manifests as a symmetric spectra around zero, *i.e.* holes have the same energy as particles but with a minus sign. When there are zero energy modes in the spectra, it is forbidden to move a single MBS because it would violate particle-hole symmetry. Regarding the set of  $\tau$  matrices that describe particle-hole space, when there is also spin

interactions, the interaction in both spaces is written as, for example,

$$\tau_x \otimes \sigma_x = \begin{pmatrix} 0 & 1 \\ 1 & 0 \end{pmatrix} \otimes \begin{pmatrix} 0 & 1 \\ 1 & 0 \end{pmatrix} = \begin{pmatrix} 0 & 0 & 0 & 1 \\ 0 & 0 & 1 & 0 \\ 0 & 1 & 0 & 0 \\ 1 & 0 & 0 & 0 \end{pmatrix}. \quad (2.58)$$

### 2.5.3 Reciprocal Space Kitaev Hamiltonian

The dispersion relation of the Kitaev Model can be obtained by taking the Fourier transform of the real space Hamiltonian, Eq. 2.47. Consider the fermionic operators written in a basis in  $k$ -space where the basis functions are orthonormal,

$$c_n \rightarrow \frac{1}{\sqrt{N}} \sum_k e^{ikn} c_k \quad \sum_n e^{i(k-k')n} = N \delta_{k,k'} \quad (2.59)$$

Taking the transformation term by term,

$$\sum_n -\omega (c_i^\dagger c_{i+1} + c_{i+1}^\dagger c_i) = -2\omega \sum_k \cos(k) c_k^\dagger c_k \quad (2.60)$$

$$\sum_n -\mu c_n^\dagger c_n = -\mu \sum_k c_k^\dagger c_k \quad (2.61)$$

$$\sum_n \Delta (c_j c_{j+1} + c_{j+1}^\dagger c_j^\dagger) = i\Delta \sum_k \sin(k) (c_k^\dagger c_{-k}^\dagger - c_{-k} c_k) \quad (2.62)$$

It only creates electron traveling in the same direction, or in opposite direction. That is, creates particles and holes. We impose particle-hole symmetry,

$$-2\omega \sum_k \cos(k) c_k^\dagger c_k = 2\omega \sum_k \cos(k) c_{-k}^\dagger c_{-k} \quad (2.63)$$

$$-\mu \sum_k c_k^\dagger c_k = \mu \sum_k c_{-k}^\dagger c_{-k} \quad (2.64)$$

and we use the particle-hole basis. In such representation, the Hamiltonian can be written as,

$$H = \sum_k \begin{pmatrix} c_k^\dagger & c_{-k} \end{pmatrix} H_{BdG}(k) \begin{pmatrix} c_k \\ c_{-k}^\dagger \end{pmatrix}, \quad (2.65)$$

where,

$$H_{BdG}(k) = \begin{pmatrix} -(\mu + 2\omega \cos(k)) & 2i\Delta \sin(k) \\ -2i\Delta \sin(k) & (\mu + 2\omega \cos(k)) \end{pmatrix}, \quad (2.66)$$

this expression can be rewritten in a compact notation using the set of  $\tau$  matrices, that are similar to the spin Pauli matrices but in particle-hole space as,

$$H_{BdG}(k) = -(\mu + 2\omega \cos(k))\tau_z - 2\Delta \sin(k)\tau_y. \quad (2.67)$$

The energy-momentum relation for particle and holes is given by solutions of the secular equation,

$$\det(H_K - E) = 0 \quad (2.68)$$

Which yields the following relation consistent with the results of Kitaev<sup>10</sup>,

$$E_{\pm} = \pm \sqrt{(\mu + 2\omega \cos(k))^2 + 4\Delta^2 \sin^2(k)}. \quad (2.69)$$

It is important to consider that one is assuming an infinite system, so there will be no zero energy states because the system has no ends. Nonetheless, the topological or trivial phase manifests as an inversion of the bands that shows a Dirac cone-like structure in the topological phase as shown in Fig. 2.11. In the trivial phase, such structure is inverted, as shown in Fig. 2.12.

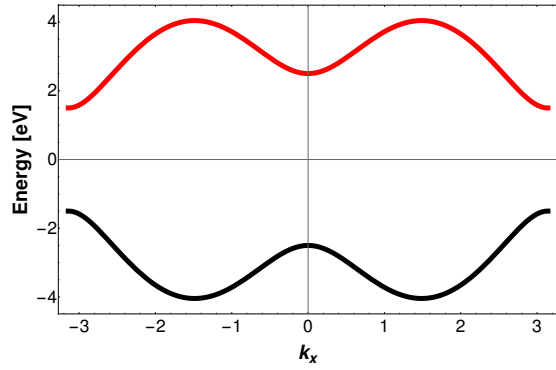


Figure 2.11: Spectra of Kitaev dispersion relation with parameters (eV):  $\Delta = 1$ ,  $\mu = 0.5$   $\omega = 0.5$ . AI

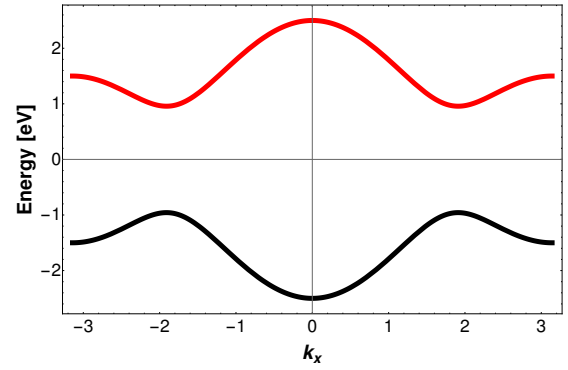


Figure 2.12: Spectra of Kitaev dispersion relation with parameters (eV):  $\Delta = 1$ ,  $\mu = 1.5$   $\omega = 0.5$ .

#### 2.5.4 Linear Approximation of the Kitaev Hamiltonian

In the energy-momentum relation of the Kitaev model there is a band inversion that happens at the phase transition point when the gap closes and can be observed in Fig. 2.11 and 2.12. In order to understand this transition, an accurate approximation close to that point is derived. Consider  $k \approx 0$  in Eq. 2.69 and Eq. 2.67, then  $\cos(k) \approx 1$  and  $\sin(k) \approx k$ , that is,

$$E(k) \approx \pm \sqrt{m^2 + 4|\Delta|^2 k^2}, \quad (2.70)$$

where  $m = \mu + 2\omega$  is the effective mass parameter. Such energy relation can be easily obtained from the following Hamiltonian,

$$H = \tau_z 2|\Delta|k + \tau_y m. \quad (2.71)$$

In the superconducting basis, the two solutions correspond for particle and hole states. The topological character of the system is controlled by the mass function,  $m(x)$ . If  $m(x) < 0$  the system is in the topological phase. If  $m(x) > 0$

the system is in the trivial phase corresponding to Fig. 2.11 and 2.12 respectively. At  $m(x) = 0$  there is a topological phase transition. At this point, the Hamiltonian becomes a Dirac-like hamiltonian. We refer to it a Dirac-like since it is linear in momentum. Considering  $v = 2|\Delta|$ , the effective Hamiltonian reads  $H = \tau_z v k$ . The eigenstates have energy  $E = \pm v k$ . It corresponds to electrons and holes around  $k = 0$  moving to the left or the right respectively.

### 2.5.5 Majorana Fermions at a Domain Wall

MBS's occur at defects, edges or domains walls<sup>9,15</sup>. To describe such situation, consider the real space representation of Eq. 2.71. To describe zero-energy modes, we know that the Schrodinger equation reads  $H\Psi = 0$ . Then, one rewrites  $H$  as,

$$\frac{\partial}{\partial x} \Psi(x) = \tau_x \frac{1}{v} m(x) \Psi(x) \quad (2.72)$$

Consider a  $m$  such that has a phase transition at  $x = 0$ . Then, the system of equations reads,

$$\partial_x \Psi_p(x) = \frac{m(x)}{v} \Psi_h(x), \quad \partial_x \Psi_h(x) = \frac{m(x)}{v} \Psi_p(x), \quad (2.73)$$

where the wavefunction is  $\Psi(x) = (\Psi_p(x) \Psi_h(x))$ , and  $\Psi_{p/h}$  corresponds to the wavefunction of the particle and hole respectively. The solution is given by the eigenvectors of  $\tau_x$  as,

$$\Psi(x) = \exp\left(\pm \int_0^x \frac{m(x')}{v} dx'\right) (1 \pm 1)^T. \quad (2.74)$$

One of the two solutions is normalizable, while the other diverges. We choose different mass functions that have one or two phase transition points, and the resulting wavefunctions are shown in Fig. 2.13.

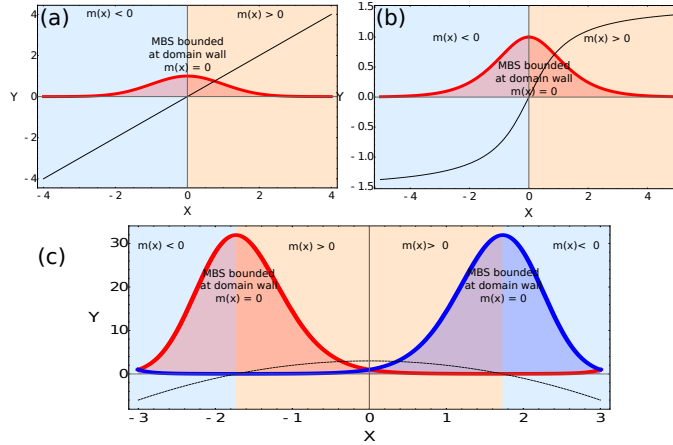


Figure 2.13: Graphical representation of the computed wavefunctions at a domain wall for different mass functions in the Kitaev model. Red and blue line:  $|\Psi(x)|^2$ . Black dashed line:  $m(x)$ . Blue region:  $m(x) < 0$ . Red region:  $m(x) > 0$ . (a)  $m(x) = x$ . (b)  $m(x) = \arctan(x)$ . (c)  $m(x) = -x^2 + 3$ .

## 2.6 Effective TB model of a ferromagnetic chain of atoms on top of a superconducting surface

To address the experimental setup recently suggested<sup>2</sup> from DFT calculations, and give insight into the microscopical details of the proximity effect, we develop an analytical TB model of such system where MBS appear as zero energy modes. We consider a two layer zig-zag atomic chain on top of a Pb (110) superconducting surface. The atomic chain is periodic along the  $x$ -axis as shown in Fig. 2.14. The chain is ferromagnetic and the magnetization directions follows the chain axis. The zig-zag structure generates an embedding of the lowestmost atom and the topmost atoms are out of the surface. Two layers of Pb atoms are interacting with the Fe chain and producing different coupling for each atom.

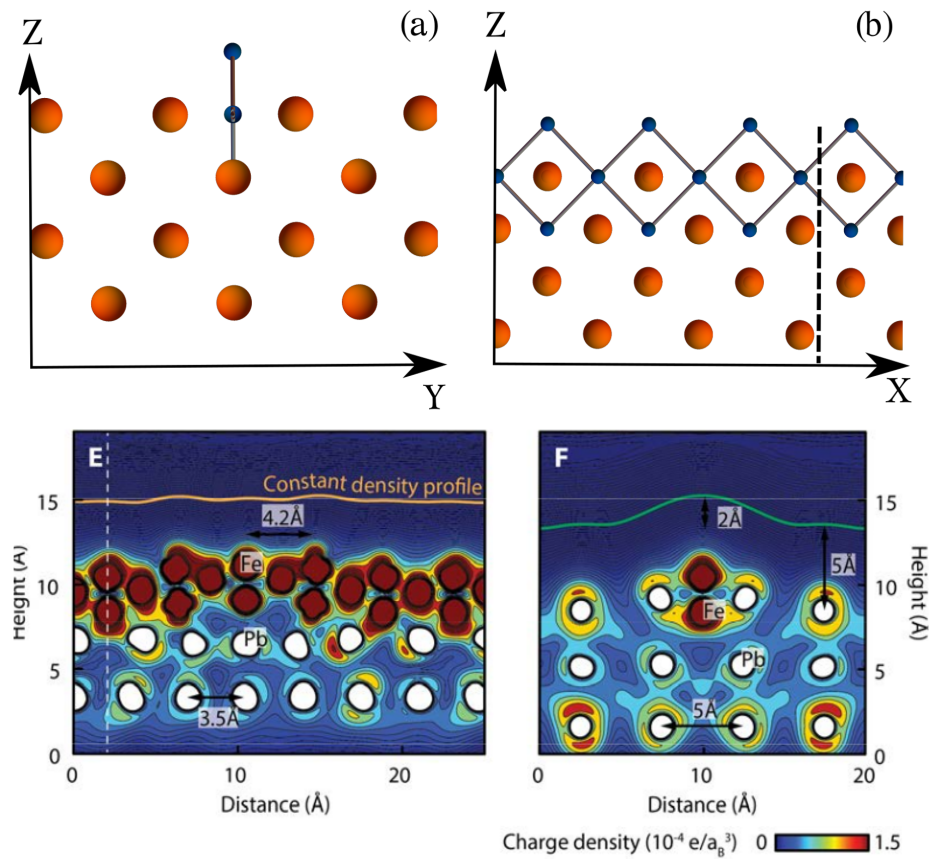


Figure 2.14: Lateral view of the atomic wire showing Fe (blue) atoms and the bonds (gray), on top of a Pb (orange) surface.

The description of the full system is given by the Hamiltonian shown in Eq. E.1. There are two structural Hamiltonians that describe each atomic specie, and there is a kinetic coupling between them. The system includes the following interactions: i) Kinetic interaction given by SK integrals. ii) Atomic SO interaction from Fe and Pb atoms. iii) Ferromagnetic order along the chain axis for all  $d$ -orbitals. iv) s-wave superconductivity in the Pb surface. The full Hamiltonian is given by,

$$H = H_{Fe} + H_{Pb} + H_{Fe-Pb}, \quad (2.75)$$

where,

$$H_{Fe} = H_{SK}^{Fe} + H_J + H_{SO}^{Fe}, \quad H_{Pb} = H_{SK}^{Pb} + H_{SO}^{Pb} + H_{SC} \quad (2.76)$$

$$H_{Pb-Fe} = H_{SK}, \quad H_J = \mathbf{J} \cdot \boldsymbol{\sigma} = J\sigma_x, \quad (2.77)$$

where,  $H_{SO}$  is the spin-orbit interaction,  $H_{SK}$  is the Slater-Koster interaction of the chain, the surface, and between them, and  $H_{SC}$  is the superconducting effect. Ferromagnetic order is described as a Stoner term  $H_J$  where  $\mathbf{J}$  is the magnetization direction that in this case goes to the  $x$ -axis, and  $\boldsymbol{\sigma}$  is the vector of Pauli matrices.

### 2.6.1 Unit Cell

The unit cell is the one show in Fig. 2.15. There are 8 atoms per unit cell. The three Fe (blue) atoms are labeled **A**, **B**, and **C**. In principle, atom **A** is not connected directly to **C** to first order. The three Pb (orange) atoms are labeled **D**, **F**, **G**, **H** and **D'**. The atom **D'** is placed at  $y = 0$ , *i.e.* in the same plane as the atomic chain, while the other atoms are out of place and symmetric with respect to reflections around  $xz$ -plane. The chain axis is the  $x$  direction, and inversion symmetry is broken at  $z = 0$  by the Pb atoms.

### 2.6.2 Atomic basis and orbital structure

The atomic basis set that is used to describe this system includes  $d$  and  $p$  electrons to describe Fe and Pb, respectively. The states of the system are described by hydrogenic wavefunctions shown in Table 2.1. In principle, there are 5  $d$ -orbitals  $\times$  3 Fe atoms per unit cell plus 3  $p$ -orbitals  $\times$  5 Pb atoms per unit cell, that is a  $30 \times 30$  space without including spin and particle-hole. The size of the full system of the unit cell matrix is  $120 \times 120$ , that is a very large number to describe analytically. Then, we must find a minimal set of atomic orbitals and atoms that encodes the most relevant physical features of the problem. For such purposes, we obtain the representation of all the atomic orbitals involved and show it in Table 2.1. Furthermore, the SK interactions between the  $d$ -orbitals of the atomic chain is shown in Table 2.3, and the SO interaction of  $d$  and  $p$  orbitals is shown in Table 2.2. Using this information we are able to find a minimal basis set that describes the full system effectively.

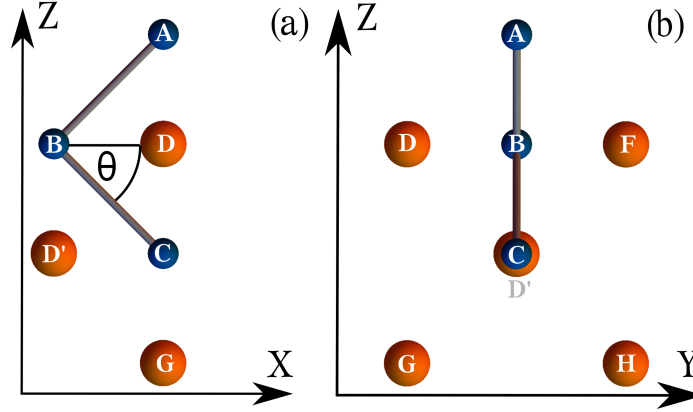
It has been suggested that the appearance of MBS in this structure is caused by the strong hybridization between atomic orbitals of Pb and Fe atoms. Also, previous models have considered that the most hybridized orbitals are those from the  $\pi$  structure, while the  $\sigma$  structure remains smaller. As a first consideration, we choose the atomic

Table 2.1: Orbital basis of  $p$  and  $d$  orbitals in the cartesian and spherical harmonic basis. These basis set is used to describe the different atomic species of the system. Note that the  $d$  orbitals were relabelled to lie around the  $x$  direction, but SO matrix elements have not changed.

	Cubic	Spherical
s orbital	$ s\rangle = \frac{1}{4\pi}$	$=  0, 0\rangle$
p orbitals	$ p_x\rangle = \sqrt{\frac{3}{4\pi}} \frac{1}{r} x$ $ p_y\rangle = \sqrt{\frac{3}{4\pi}} \frac{1}{r} y$ $ p_z\rangle = \sqrt{\frac{3}{4\pi}} \frac{1}{r} z$	$= \frac{1}{\sqrt{2}}( 1, -1\rangle -  1, 1\rangle)$ $= \frac{i}{\sqrt{2}}( 1, -1\rangle +  1, 1\rangle)$ $=  1, 0\rangle$
d orbitals	$ d_{x^2}\rangle = \sqrt{\frac{5}{16\pi}} \frac{1}{r^2} (3x^2 - r^2)$ $ d_{xz}\rangle = \sqrt{\frac{5}{16\pi}} \frac{1}{r^2} 2\sqrt{3}xz$ $ d_{yx}\rangle = \sqrt{\frac{5}{16\pi}} \frac{1}{r^2} 2\sqrt{3}yx$ $ d_{zy}\rangle = \sqrt{\frac{5}{16\pi}} \frac{1}{r^2} 2\sqrt{3}zy$ $ d_{z^2-y^2}\rangle = \sqrt{\frac{5}{16\pi}} \frac{1}{r^2} 2\sqrt{3}(z^2 - y^2)$	$=  2, 0\rangle$ $= \frac{1}{\sqrt{2}}( 2, -1\rangle -  2, 1\rangle)$ $= \frac{i}{\sqrt{2}}( 2, -1\rangle +  2, 1\rangle)$ $= \frac{i}{\sqrt{2}}( 2, -2\rangle -  2, 2\rangle)$ $= \frac{1}{\sqrt{2}}( 2, 2\rangle +  2, -2\rangle)$

Table 2.2: Spin orbit interaction matrix elements for  $p$  and  $d$  orbitals. Here,  $\xi_p$  ( $\xi_d$ ) is the magnitude of the SO interaction between  $p$  ( $d$ ) orbitals, and the  $\sigma_i$  operators are the spin Pauli matrices. Note that there is no SO interaction between  $p$  and  $d$  orbitals.

	$ d_{x^2}\rangle$	$ d_{xz}\rangle$	$ d_{yx}\rangle$	$ d_{zy}\rangle$	$ d_{z^2-y^2}\rangle$	$ p_x\rangle$	$ p_y\rangle$	$ p_z\rangle$
$ d_{x^2}\rangle$	0	$-i\sqrt{3}\xi_d\sigma_y$	$i\sqrt{3}\xi_d\sigma_x$	0	0	0	0	0
$ d_{xz}\rangle$	$i\sqrt{3}\xi_d\sigma_y$	0	$-i\xi_d\sigma_z$	$i\xi_d\sigma_x$	$-i\xi_d\sigma_y$	0	0	0
$ d_{yx}\rangle$	$-i\sqrt{3}\xi_d\sigma_x$	$i\xi_d\sigma_z$	0	$-i\xi_d\sigma_y$	$-i\xi_d\sigma_x$	0	0	0
$ d_{zy}\rangle$	0	$-i\xi_d\sigma_x$	$i\xi_d\sigma_y$	0	$2i\xi_d\sigma_z$	0	0	0
$ d_{z^2-y^2}\rangle$	0	$i\xi_d\sigma_y$	$i\xi_d\sigma_x$	$-i\xi_d\sigma_z$	0	0	0	0
$ p_x\rangle$	0	0	0	0	0	0	$-i\xi_p\sigma_z$	$i\xi_p\sigma_y$
$ p_y\rangle$	0	0	0	0	0	$i\xi_p\sigma_z$	0	$-i\xi_p\sigma_x$
$ p_z\rangle$	0	0	0	0	0	$-i\xi_p\sigma_y$	$i\xi_p\sigma_x$	0



ht

Figure 2.15: Unit cell of the ferromagnetic atomic chain. Two layers of Pb atoms are considered to interact at the top of the surface. (a) Lateral view where the Fe atoms are called **A**, **B** and **C**. (b) Front view where all the five Pb atoms can be observed. Pb atom **D'** (gray) is behind Fe atom **C**.

Table 2.3: Slater Koster integrals for  $d$  orbitals. Vertical and horizontal lines separate the subspace of  $d$  bands  $\sigma$ ,  $\pi$  and  $\delta$ . Here  $V_{dd\sigma}$ ,  $V_{dd\pi}$  and  $V_{dd\delta}$  are the SK parameters that describe the strength of the bonding.

	$ d_{x^2}\rangle$	$ d_{xz}\rangle$	$ d_{yx}\rangle$	$ d_{zy}\rangle$	$ d_{z^2-y^2}\rangle$
$\langle d_{x^2} $	$\frac{1}{16}(6V_{dd\delta} + 12V_{dd\pi} + V_{dd\sigma})$	$-\frac{\sqrt{3}}{8}(V_{dd\delta} - 2V_{dd\pi} + V_{dd\sigma})$	0	0	$\frac{1}{16}(3V_{dd\delta} - 4V_{dd\pi} + V_{dd\sigma})$
$\langle d_{xz} $	$-\frac{\sqrt{3}}{8}(V_{dd\delta} - 2V_{dd\pi} + V_{dd\sigma})$	$\frac{1}{2}(V_{dd\pi} + V_{dd\delta})$	0	0	$-\frac{3}{8}(V_{dd\delta} - V_{dd\sigma})$
$\langle d_{yx} $	0	0	$\frac{1}{4}(3V_{dd\sigma} + V_{dd\delta})$	$\frac{1}{2}(V_{dd\pi} - V_{dd\delta})$	0
$\langle d_{zy} $	0	0	$\frac{1}{2}(V_{dd\pi} - V_{dd\delta})$	$\frac{1}{2}(V_{dd\pi} + V_{dd\delta})$	0
$\langle d_{z^2-y^2} $	$\frac{1}{16}(3V_{dd\delta} - 4V_{dd\pi} + V_{dd\sigma})$	$-\frac{3}{8}(V_{dd\delta} - V_{dd\sigma})$	0	0	$\frac{1}{16}(9V_{dd\delta} + 4V_{dd\pi} + 3V_{dd\sigma})$

orbitals involved in a  $\pi$  bonding between the chain and the surface. Then, we are not interested in orbitals with components along  $y$  direction since this directions is for a  $\sigma$  bonding. In any case, further considerations could change this initial idea.

### Atomic Basis for the Fe Ferromagnetic Chain

Electrons from  $d$  orbitals of Fe form three bands defined as,

$$\begin{cases} \sigma : & |x^2\rangle \\ \pi : & |xz\rangle, |xy\rangle \\ \delta : & |yz\rangle, |y^2 - z^2\rangle \end{cases} \quad (2.78)$$

The  $\sigma$  band accounts for the innermost electrons of  $d$ -bands. The  $\pi$  and  $\delta$  are spin degenerate bands, with conduction electrons, because of rotational symmetry of the atomic chain around the  $\hat{x}$  axis. Degeneracy is lifted by SO and SK interactions between the  $\delta$  band with the other bands. In Table 2.3 and 2.2, one observes that  $d_{z^2}$  is connected by both interactions to the  $d_{xz}$ . We consider that degeneracy is lifted due to these interactions, and it is necessary to include all  $d$ -bands in a complete description of the system. In order to build a minimal model based on the geometrical configuration shown in Fig. 2.15, we calculate all the SK integrals between  $d$  orbitals that are shown in Table 2.3 and study the atomic SO interaction between  $d$  orbitals shown in Table 2.2, and we note that the SO matrix elements between the  $\sigma$  and  $\delta$  bands are zero. Then, we choose the  $\pi$  band to be describe the system with inherited interactions from  $\sigma$  and  $\delta$ . Regarding the magnetic properties of the system, we assume that the ferromagnetic order of the chain is directed along the  $x$ -axis and all orbitals contribute equally. This assumption is not prohibited from experimental data. The relevant SK integrals from Table 2.3 are defined as,

$$\begin{aligned} U_{xz} &= E_{xz,xz}^{t,J} = E_{xz,xz}^{J,t} = E_{xz,xz}^{J,k} = E_{xz,xz}^{k,J} = \frac{1}{4}(V_{dd\delta} + 3V_{dd\sigma}), \\ U_{x^2} &= E_{xz,x^2}^{t,J} = -E_{xz,x^2}^{J,t} = -E_{xz,x^2}^{J,k} = E_{xz,x^2}^{k,J} = -\frac{1}{8}\sqrt{3}(V_{dd\delta} - 2V_{dd\pi} + V_{dd\sigma}), \\ U_{z^2} &= E_{xz,z^2}^{t,J} = -E_{xz,z^2}^{J,t} = -E_{xz,z^2}^{J,k} = E_{xz,z^2}^{k,J} = -\frac{3}{8}(V_{dd\delta} - V_{dd\sigma}), \end{aligned} \quad (2.79)$$

where  $V_{dd\sigma}$ ,  $V_{dd\pi}$  and  $V_{dd\delta}$  are SK parameters for each band of the  $d$ -orbitals. In general, these expressions are a function of the angle of the atomic chain  $\theta$ , but for  $\theta = \pi/4$ , as in Fig.2.14, they have this forms.

### Atomic Basis for the Pb Superconducting Surface

In this model, we assume that the dominant tunneling processes are caused by  $V_{pd\pi}$  rather than  $V_{pd\sigma}$ . In Fig. 2.15 one can observe that the atom  $\mathbf{D}'$  has only a  $\sigma$  bond, while  $\mathbf{D}$  and  $\mathbf{F}$  have only  $\pi$  bonds. Then, we neglect the interaction of the atom  $\mathbf{D}'$  and assume that the dominant contribution comes from the other 4 Pb atoms. All the matrix elements of the SK interaction between  $d_{xz}$  and  $p$  orbitals are shown in Table 2.6. Since  $p_y$  is orthogonal to  $d_{xz}$  their corresponding SK elements are zero. Then, it is only necessary to consider  $p_x$  and  $p_z$  to describe the Pb surface.

The SK elements shown in Table 2.6 are defined as,

$$\begin{aligned} U_x &= E_{x,xz}^{t,J} = V_{pd\pi}, \\ U_z &= E_{z,xz}^{t,J} = V_{pd\pi}. \end{aligned} \quad (2.80)$$

where  $V_{pd\pi}$  represents the degree of hybridization, and  $U'_x = U_x$ . In general, these expression change for different angles between the chain and the surface, but at  $\theta = \pi/4$  they are all equal. Also, in Fig. 2.17 (a) one observes that the curves are identical by changing  $\theta \rightarrow -\theta$ . We exploit this fact in order to describe different geometrical configurations for the chain embeded in the surface. Since atoms  $\mathbf{G}$  and  $\mathbf{H}$  are closer to the Pb bulk, we assume that they do not change their positions.

### Minimal Atomic Basis for the Full System

The minimal set of atoms and orbitals used to describe each atomic specie is,

$$\begin{cases} \text{Fe :} & \{|d_{xz}\rangle, |d_{x^2}\rangle, |d_{z^2}\rangle\} \otimes \{|A\rangle, |B\rangle, |C\rangle\} \\ \text{Pb :} & \{|p_x\rangle, |p_z\rangle\} \otimes \{|D\rangle, |F\rangle\}, \quad |p_x\rangle \otimes \{|G\rangle, |H\rangle\} \end{cases} \quad (2.81)$$

where the kets  $|A\rangle$  describe the each atom, in this case A.

### 2.6.3 Effective Single Orbital Chain

Let us start by bulding an effective single  $d$  orbital chain, where the  $\sigma$  structure is folded into the  $\pi$  structure to include the spin interactions of the innermost electrons. The full Hamiltonian of the wire is shown in Table 2.4, and shows that the only hopping processes that we consider are those purely of the  $\pi$  band, since we assume that these are the moving electrons at the Fermi level.

Table 2.4: Matrix elements of the interaction between orbitals within the chain without ferromagnetic Stoner interaction. Internal lines are used to separate the three bands  $\pi$ ,  $\sigma$  and  $\delta$  in that order.

	$ d_{xz}\rangle_A$	$ d_{xz}\rangle_B$	$ d_{xz}\rangle_C$	$ d_{x^2-r^2}\rangle_A$	$ d_{x^2-r^2}\rangle_B$	$ d_{x^2-r^2}\rangle_C$	$ d_{z^2}\rangle_A$	$ d_{z^2}\rangle_B$	$ d_{z^2}\rangle_C$
$\langle d_{xz} _A$	$\epsilon_d$	$U_{xz}$	0	$-i\sqrt{3}\xi_d\sigma_x$	$-U_{x^2}$	0	$i\xi_d\sigma_x$	$U_{z^2}$	0
$\langle d_{xz} _B$	$U_{xz}$	$\epsilon_d$	$U_{xz}$	$U_{x^2}$	$-i\sqrt{3}\xi_d\sigma_x$	$-U_{x^2}$	$-U_{z^2}$	$i\xi_d\sigma_x$	$U_{z^2}$
$\langle d_{xz} _C$	0	$U_{xz}$	$\epsilon_d$	0	$U_{x^2}$	$-i\sqrt{3}\xi_d\sigma_x$	0	$-U_{z^2}$	$i\xi_d\sigma_x$
$\langle d_{x^2-r^2} _A$	$i\sqrt{3}\xi_d\sigma_x$	$U_{x^2}$	0	$\epsilon_d$	0	0	0	0	0
$\langle d_{x^2-r^2} _B$	$-U_{x^2}$	$i\sqrt{3}\xi_d\sigma_x$	$U_{x^2}$	0	$\epsilon_d$	0	0	0	0
$\langle d_{z^2} _C$	0	$-U_{x^2}$	$i\sqrt{3}\xi_d\sigma_x$	0	0	$\epsilon_d$	0	0	0
$\langle d_{z^2} _A$	$-i\xi_d\sigma_x$	$-U_{z^2}$	0	0	0	0	$\epsilon_d$	0	0
$\langle d_{x^2-r^2} _B$	$U_{z^2}$	$-i\xi_d\sigma_x$	$-U_{z^2}$	0	0	0	0	$\epsilon_d$	0
$\langle d_{z^2} _C$	0	$U_{z^2}$	$-i\xi_d\sigma_x$	0	0	0	0	0	$\epsilon_d$

In order to obtain an effective Hamiltonian using the BF method, we divide the Hamiltonian into two subspaces, one that describes the  $\pi$  band, and the other space for the other two bands. In this manner, the Fe atoms are described by the following Hamiltonian,

$$H_{Fe} = \begin{pmatrix} H_{xz} & T_{xz} \\ T_{xz}^\dagger & H_d \end{pmatrix} + H_J \quad (2.82)$$

where the diagonal components are the structural Hamiltonians of  $|d_{xz}\rangle$  and  $|d_{x^2}\rangle$  and  $|d_{z^2}\rangle$  orbitals,  $H_J = J\sigma_x$  is the Stoner interaction and  $J$  is the exchange interaction, and  $T_{xz}$  is the connection matrix of the two spaces that includes SK and SO terms taken from Eq. 2.79. All the matrix elements of  $H_{Fe}$  for the unit cell are written in Table 2.4.

Using the band folding method, we define the effective system to be  $H_{chain}$ . Then, the effective Hamiltonian for this system is given by,

$$H_{chain} = \begin{pmatrix} \epsilon'_d + J'\sigma_x & U_{xz} + i(\xi_{Fe}\sigma_y + \xi_J\sigma_z) & U_{AC} \\ U_{xz} - i\xi_{Fe}\sigma_y & \epsilon'_d + J'\sigma_x & U_{xz} + i\xi_{Fe}\sigma_y \\ U_{AC} & U_{xz} - i(\xi_{Fe}\sigma_y + \xi_J\sigma_z) & \epsilon'_d + J'\sigma_x \end{pmatrix}, \quad (2.83)$$

where the effective effective interactions from Fe  $d$  orbitals are defined as,

$$\epsilon'_d = \epsilon_d \left( 1 - \frac{U_{x^2} + U_{z^2}}{\epsilon_d^2 - J^2} \right), \quad J' = J \left( 1 + \frac{U_{x^2} + U_{z^2}}{\epsilon_d^2 - J^2} \right), \quad U_{AC} = \epsilon' - \epsilon + (J' - J)\sigma_x, \quad (2.84)$$

$$\xi_{Fe} = \frac{2(\sqrt{3}U_{x^2} + U_{z^2})\xi_d\epsilon_d}{\epsilon_d^2 - J^2}, \quad \xi_J = -\frac{2J(\sqrt{3}U_{x^2} + U_{z^2})\xi_d}{\epsilon_d^2 - J^2}. \quad (2.85)$$

The internal interactions coming from the  $d$ -bands produces several effective interactions within the  $\pi$  band. First of all, there is a shift of the energy and exchange interaction because due to corrections propotional to the SK coupling and  $J$ . Second, there are two effective spin interactions, one from intrinsic SO between orbitals, and other involving SO and ferromagnetic interactions. Third, there is an effective coupling between **A** and **C** atoms that depends on the difference between normal and shifted energies. All of the corrections depend on the interference between SK interactions. In this case,  $d_{x^2}$  and  $d_{z^2}$  effects interfere constructively. Furthermore, since the nature of BF expansion is perturbatively, one must guarantee that  $\epsilon_{d\pi}$  and  $J$  are well separated in energy. Otherwise, Eq. 2.84 diverges. From the denominators of Eq. 2.84, one observes that the exchange interaction,  $J$ , and the superconducting gap,  $\Delta$ , diverge when  $J \sim \epsilon_\pi$  and  $\Delta \sim \xi_{pb}$ . We must guarantee that these quantities are well-separated in energy in order to have valid results.

#### 2.6.4 Proximity Induced Superconductivity and Rashba SO from Pb surface

The Pb surface is described by  $p$  orbitals and have two interactions, *i.e.* SC and RSO. On one hand, SC induces a pairing between particles and holes of opposite spins. On the other hand, RSO occurs at the surface due to inversion symmetry breaking and induces a rotation of spins. These two properties are inherited by proximity when the atomic chain is deposited on the surface due to the high degree of hybridization between both structures represented as  $V_{pd\pi}$ .

##### Rashba SO Pb Hamiltonian

Consider that the atoms of the surface are described by  $p$  orbitals and the SO interaction between them given in Table 2.2. The Hamiltonian that describes the Pb surface without superconductivity is,

where  $\epsilon_p$  is the energy of the bare  $p$  orbitals of the surface, and  $\xi_{pb}$  is the magnitude of the RSO. Note that there is only two SO matrix elements since atoms **G** and **H** have only one orbital.

Table 2.5: Slater Koster integrals for  $d_{xz}$  and  $p$  orbitals for all the atoms in the unit cell except for  $\mathbf{D}'$ . Also, for Pb atoms only  $p_x$  and  $p_z$  are considered. Since the symmetry of the unit cell (Fig. 2.15), all the SK integrals can be expressed with two expressions  $U_x$  and  $U_z$ .

	$ p_x\rangle_D$	$ p_x\rangle_F$	$ p_x\rangle_G$	$ p_x\rangle_H$	$ p_z\rangle_D$	$ p_z\rangle_F$
$\langle p_x _D$	$\epsilon_p$	0	0	0	$i\xi_p\sigma_y$	0
$\langle p_x _F$	0	$\epsilon_p$	0	0	0	$i\xi_p\sigma_y$
$\langle p_x _G$	0	0	$\epsilon_p$	0	0	0
$\langle p_x _H$	0	0	0	$\epsilon_p$	0	0
$\langle p_z _D$	$-i\xi_p\sigma_y$	0	0	0	$\epsilon_p$	0
$\langle p_z _F$	0	$-i\xi_p\sigma_y$	0	0	0	$\epsilon_p$

### Superconducting Pb Hamiltonian

SC has a  $s$ -wave character that accounts for a local pairing potential  $\Delta$  that does not depend on momentum. If one wants to include superconductivity in a real space system, one must write down the BdG Hamiltonian of the system, that is written as,

$$\mathcal{H}_{Pb} = \begin{pmatrix} H_{Pb} & \Delta \\ \Delta & -H_{Pb}^* \end{pmatrix} = H_{Pb}\tau_z + \Delta\tau_x, \quad (2.86)$$

where the  $\tau$  operators are the Pauli matrices in particle-hole space. We only consider on-site interactions and no kinetic processes between sites. In the same manner, one can obtain the BdG Hamiltonian for the effective atomic chain as,  $\mathcal{H}_{Fe} = H_{Fe}\tau_z$ .

### Fe-Pb Coupling Matrix

The interactions that connect the surface and the atomic chain are encoded in,  $T$ , the connection matrix determined by the details of the microscopic model from Fig. 2.14. Under the minimal set of atoms and orbitals, the full connection matrix is given by Table 2.6 where there are 8 entries to  $T$ .

Table 2.6: Slater Koster integrals for  $d_{xz}$  and  $p$  orbitals for all the atoms in the unit cell except for  $\mathbf{D}'$ . Also, for Pb atoms only  $p_x$  and  $p_z$  are considered. Since the symmetry of the unit cell (Fig. 2.15), all the SK integrals can be expressed with two expressions  $U_x$  and  $U_z$ .

	$ p_x\rangle_D$	$ p_x\rangle_F$	$ p_x\rangle_G$	$ p_x\rangle_H$	$ p_z\rangle_D$	$ p_z\rangle_F$
$\langle d_{xz} _A$	$U_x$	$U_x$	0	0	0	0
$\langle d_{xz} _B$	0	0	0	0	$U_z$	$U_z$
$\langle d_{xz} _C$	$U_x$	$U_x$	$U'_x$	$U'_x$	0	0

One can propose a simplification of  $T_s$  by assuming that the structure at the surface breaks the symmetry of the bulk. Two alternatives are proposed in Fig. 2.16 that consider (a) a symmetric shift for both atoms that breaks the interaction of atom **C** with **D** and **F**, and (b) an anti-symmetric shift that lifts **D** up and **F** goes down. The corresponding coupling matrices are given in Eq. 2.87. This approximation only accounts for couplings in  $T$ , but no for angular changes in the SK expressions of the corresponding atoms.

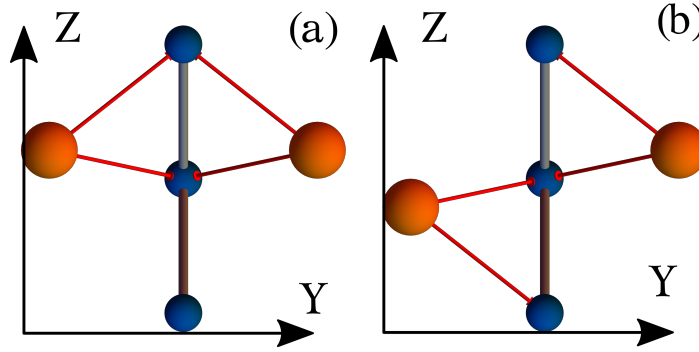


Figure 2.16: (a) Symmetry breaking process where two Pb atoms lift symmetrically. (b) Symmetry breaking process where two Pb atoms lift anti-symmetrically.

Each modified structure has different coupling for atoms **D** and **F** with respect to the initial structure shown in Table 2.6. Each situation is encoded within coupling matrices  $T_a$  and  $T_b$  given by,

$$T_a = \begin{pmatrix} U_x & 0 & 0 & 0 & 0 & 0 \\ 0 & 0 & 0 & 0 & U_z & U_z \\ 0 & U_x & U'_x & U'_x & 0 & 0 \end{pmatrix}, \quad T_b = \begin{pmatrix} U_x & U_x & 0 & 0 & 0 & 0 \\ 0 & 0 & 0 & 0 & U_z & U_z \\ 0 & 0 & U'_x & U'_x & 0 & 0 \end{pmatrix}. \quad (2.87)$$

We choose  $T = T_b$  to be the connection matrix of the problem since there is no reason a priori to have an antisymmetric shift at the top of the surface. In this approximation we have that there is no coupling between atoms **D** and **C**, as for **F**. Also, atom **C** is still superconducting since interacts with the following layer of the surface, *i.e.* **G** and **H** atoms. Then, the full system reads,

$$H = \begin{pmatrix} \mathcal{H}_{Fe}\tau_z & T\tau_z \\ T^\dagger\tau_z & \mathcal{H}_{Pb}\tau_z + \Delta\tau_x \end{pmatrix}. \quad (2.88)$$

### Proximity Induced Hamiltonian

Using BF, one obtains an effective Hamiltonian that describes the full system given by,

$$\mathcal{H} = \begin{pmatrix} \epsilon'_{dt} + \Delta_x\tau_x + J'\sigma_x & U_{xz} + i(\xi_{Pb} + \xi_{Fe})\sigma_y + i\xi_J\sigma_z & U_{AC} \\ U_{xz} - i(\xi_{Pb} + \xi_{Fe})\sigma_y - i\xi_J\sigma_z & \epsilon'_d + \Delta_z\tau_x + J'\sigma_x & U_{xz} + i\xi_{Fe}\sigma_y + i\xi_J\sigma_z \\ U_{AC} & U_{xz} - i\sigma_y\xi_{Fe} - i\xi_J\sigma_z & \epsilon'_d + \Delta'_x\tau_x + J'\sigma_x \end{pmatrix}, \quad (2.89)$$

where there is a Rashba SO interaction coming from Pb surface, and a different SC gap at each Fe atom. The new effective quantities are defined as,

$$\xi_{Pb} = \frac{\xi_p U_x U_z}{\xi_p^2 - \Delta^2}, \quad \Delta_x = \frac{2\Delta U_x^2}{\Delta^2 - \xi_p^2}. \quad (2.90)$$

Here the SC interactions,  $\Delta_i$  where  $i = x, z, x'$  is the orbital labeling that corresponds with the SK element  $U_i$ .

## 2.6.5 Effective $2 \times 2$ Hamiltonian

Finally, we apply BF for the last time to include the **C** atom effectively into the **A** and **B** atoms as a shift to the energy and exchange interaction,  $\epsilon_C$  and  $J_C$  respectively, that breaks the symmetry between the two atomic sites. Let us consider that Eq. 2.89 is written in the atom basis for **A**, **B** and **C**. Let us separate the first  $2 \times 2$  space as  $h_{AB}$ , the lowest one as  $h_C$ , and the connections as  $t$ . Then, the final effective Hamiltonian is given by,

$$\mathcal{H} \approx h_{AB} - t h_C^{-1} t^\dagger, \quad (2.91)$$

where the corrections are given by,

$$t h_C^{-1} t^\dagger = \frac{\epsilon'_d - J' \sigma_x + \tau_x \Delta'_x}{\epsilon'_d (\epsilon'_d + \Delta'_x) - J'^2} \begin{pmatrix} U_{AC} & \\ U_{xz} - i(\xi_{Fe} \sigma_y + \xi_J \sigma_z) & \end{pmatrix} \begin{pmatrix} U_{AC} & U_{xz} + i(\xi_{Fe} \sigma_y + \xi_J \sigma_z) \\ 0 & \epsilon_C - J_C \sigma_x \end{pmatrix} \approx \begin{pmatrix} 0 & 0 \\ 0 & \epsilon_C - J_C \sigma_x \end{pmatrix}. \quad (2.92)$$

Here we have obtained a  $2 \times 2$  matrix that has components of the order  $U_{AC}^2$  that is third and fourth order in SK and SO interactions. We neglect these terms and obtain only a correction for the energy and exchange interaction of the **B** atom. The resulting Hamiltonian is written as,

$$\mathcal{H} \approx \begin{pmatrix} \epsilon'_d + \Delta_x \tau_x + J' \sigma_x & U_{xz} + i(\xi' \sigma_y + \xi_J \sigma_z) \\ U_{xz} - i(\xi' \sigma_y + \xi_J \sigma_z) & \epsilon'_d + \Delta_z \tau_x + J'' \sigma_x \end{pmatrix}. \quad (2.93)$$

The corrected energy and exchange interaction are,

$$\begin{aligned} \epsilon''_d &= \epsilon'_d - \epsilon_C = \epsilon'_d - \frac{U_{xz}^2 \epsilon_d}{(\xi_{Pb}^2 - \Delta^2)(\epsilon_d'^2 - J'^2) + (2U_x'^2 \Delta J' + U_x^2(\xi_{Pb}^2 - \Delta^2))}, \\ J'' &= J' - J_C = J' - \frac{J U_{xz}^2}{(\xi_{Pb}^2 - \Delta^2)(\epsilon_d'^2 - J'^2) + (2U_x'^2 \Delta J' + U_x^2(\xi_{Pb}^2 - \Delta^2))}. \end{aligned} \quad (2.94)$$

In the full expression we observe that second order corrections have poles at corrected energies resembling the perturbative nature of BF method. The final effective Hamiltonian is for a  $2 \times 2$  problem, that effectively includes the **C** atom that is very deep in the superconductor. We are interested in the part of the chain that is not embedded because we cannot access below the surface. On the contrary, several measurements can be done on the uppermost atoms of the chain. Nonetheless, the presence of the **C** atom is relevant for discussing the geometrical structure of the system and stability of zero-energy modes. If these corrections are ignored, one can describe a single layer zig-zag atomic chain.

### 2.6.6 Deformation Scheme

The geometrical nature of SK integrals allows us to explore different atomic chain structures proposed. Also, it allows analyze how MBS are in different configuration. For the deformation scheme, we assume the following:

1. Pb atoms are fixed. The positions of Pb atoms do not change, but their relative angles to the atomic chain modify when it is deformed.
2. Position of **B** Fe atoms is fixed. In this manner the length of the chain does not change significantly under reasonable deformations. Then, the angle between **B** Fe atom with **D** or **F** Pb atoms is fixed to  $\theta_B = \pi/4$ .
3. Positions of **A** and **C** Fe atoms change anti-symmetrically according to  $\theta$ . In this manner, **A** atoms can go out of the surface or closer to  $z = 0$ . The opposite case for **C** atoms that go deep in the surface or close to the zero.

We are interested in deformations of the atomic chain that do not alter the commensurability of the lattice is not changed. The previous assumptions guarantee that the angle of the chain varies in a reasonable range, *i.e.*  $\theta : [0.05\pi, 0.45\pi]$ . Then, we analyze the properties of the chain in different angular configurations. To describe such system, let us define the angles  $\theta_A$  and  $\theta_C$  as the angle of the **D** atom to the **A** and from atom **G** to **C** respectively. They are shown in Fig. 2.15. One can derive conditions for the evolution of the SK integrals given that come from the movement of the Fe atoms in the different positions with respect to Pb atoms. They are given as,

$$U_x = U_x(\theta_A), \quad U'_x = U'_x(\theta_C) = U'_x(0.45\pi - \theta_A). \quad (2.95)$$

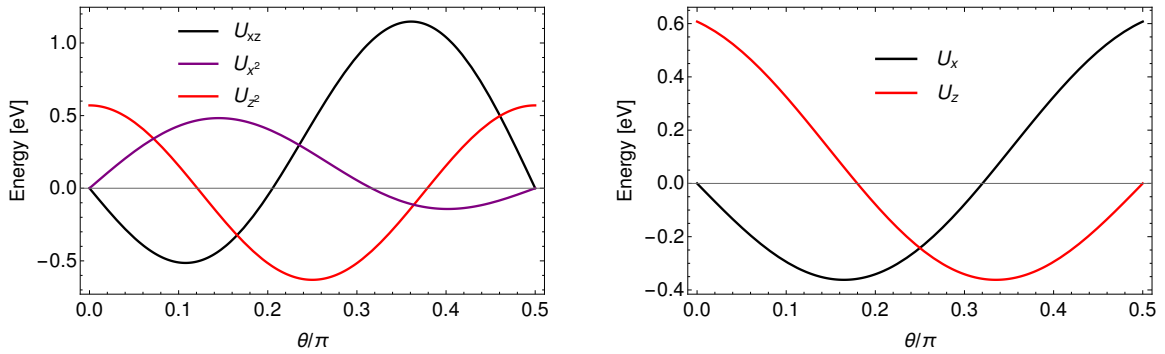


Figure 2.17: (a) SK integrals of the atomic chain. (b) SK integrals that connect Pb to Fe from  $p$ -orbitals.

Under this scheme of deformations we are able to exploit the angular dependence of SK parameters. In Fig. 2.17 (a) and (b) one can observe the angular dependence of the SK integrals. The overlaps for  $d$ -orbitals (a) have several crossings with zero energy that will be very important to changes in effective interactions. The SK integrals for the  $|d_{xz}\rangle$  and  $|d_{z^2}\rangle$  (black and purple curves) are zero when  $\theta = 0$ , that is expected since in this configuration bonds

---

are predominantly of  $\sigma$  kind. Consequently,  $|d_{x^2}\rangle$  orbitals have a maximum at  $\theta = 0$ . On the other hand, the overlaps for  $p$ -orbitals (b) are symmetric under reflections at  $\theta = \pi/4$ . It is important to note that local extremas will be inherited by effective interactions.



# Chapter 3

## Results & Discussion

### 3.1 Effective Hamiltonian

The effective Hamiltonian can be written, from Eq. 2.93, as a BdG Hamiltonian written in the Nambu basis as,

$$\mathcal{H} = \sum_{i=1}^N \hat{\Psi}_i^\dagger [-\epsilon_i \tau_z + \Delta_i \tau_x + J_i \sigma_x] \hat{\Psi}_i + \sum_{i=1}^{N-1} \hat{\Psi}_{i+1}^\dagger [U_{xz} + i(\xi \sigma_y + \xi_J \sigma_z)] \tau_z \hat{\Psi}_i + H.C., \quad (3.1)$$

where the creation and annihilation operators are written as  $\hat{\Psi} = (\Psi_{j,\uparrow}^\dagger, \Psi_{j,\downarrow}^\dagger, \Psi_{j,\downarrow}, -\Psi_{j,\uparrow})$ ,  $\sigma(\tau)$  operators act on spin(particle-hole) space,  $\epsilon_i$  is the energy of the site  $i$ ,  $J_i$  and  $\Delta_i$  are the exchange interaction and the SC gap at site  $i$  that change between shifted and normal energies,  $U_{xz}$  is the hopping amplitude between pure  $|d_{xz}\rangle$  orbitals, and  $\xi$  is the effective RSO interaction that includes effects from the chain and the surface.

Eq. 3.1 is similar to the one that was used to describe the so-called topological Rashba nanowire<sup>45</sup> that is a well known platform for MBS. The differences are: i) Different energy and exchange interaction, Eq. 2.94, between successive atomic sites. ii) Extra interaction coming from the interplay of ferromagnetic order and atomic SO. In principle, this extra terms produce a gap between the two zero-energy states that breaks the symmetry of MBS. Since the perturbative nature of this corrections, experimental techniques with high energy resolution are fundamental to confirm our predictions.

### 3.2 Physical Parameters

The main result of this work is Eq. 3.1 from which we can extract information about the quasiparticle excitations in real space, *i.e.* position space. Also, we can manipulate the experimental parameters in order to stabilize and optimize Majorana excitations. We analyze the energy spectra, the wavefunctions, and the local density of states. To do so, we require numerical values for the parameters of the system, which are obtained from previous works. The parameters are listed in the following table: The following parameters are not listed:  $J$  and  $\Delta$ . We analyze

Table 3.1: SK parameters for  $d$  and  $p$  orbitals.

Parameter	Value [eV]	Parameter	Value [eV]
$V_{dd\sigma}$	-0.6702 <sup>46</sup>	$\xi_{Fe}$	0.03 <sup>47</sup>
$V_{dd\pi}$	0.5760 <sup>46</sup>	$\xi_{Pb}$	0.665 <sup>48</sup>
$V_{dd\delta}$	-0.1445 <sup>46</sup>	$\epsilon_d$	1
$V_{pd\pi}$	-0.2170 <sup>46</sup>	$\epsilon_p$	0

different regimes for these parameters, and we propose variations from reported values due to limitations of this model. The magnitude of the exchange interaction,  $J$ , must be at least of the same order than  $\epsilon_d$  in order to Eq. 2.94 to converge. This is in agreement with computational and experimental data<sup>2</sup>, but the precise value is higher than the ones that we used. This is in agreement with considerations about ferromagnetic order since it requires a large exchange interaction. Similarly, the SC gap,  $\Delta$ , is reported to be  $\sim$  meV, but here we use larger values (100 times larger) to have localized zero-energy states.

### 3.3 Real Space Signatures of MBS

The signatures of MBS can be observed in different properties of the real space Hamiltonian. Here we analyze the low energy spectra of the system, the wavefunctions of low energy states, and the local density of states that can be used to reproduce STM measurements. Furthermore, robustness against disorder was found to be enhanced in magnetic chains<sup>49</sup> Using the deformation scheme discussed in section 2.6.6, we analyze the low energy spectra of an atomic Fe chain of length  $L = 200$  sites that corresponds to a chain of  $\sim 60$  nm using the Fe-Fe distance 0.34 nm<sup>50,51</sup>. In the low energy spectra, we find zero-energy states within a small energy range ( $>$ meV)<sup>50,51</sup> that varies in different angular configurations.

#### 3.3.1 Effective Interactions

The effective interactions are given by the geometrical configuration of the chain. The interplay between  $d$  and  $p$  orbitals controls the magnitude of the Rashba SO and SC gap. In Fig. 3.1 one can observe the evolution of effective quantities as  $\theta$  changes. Energy and exchange interactions shifts (a) and (b) depend on SK integrals and can be suppressed around a certain geometry. The shifts caused by the exchange interactions (a) within  $d$ -orbitals are very small around  $\theta \sim 0, 0.2, 0.5$  in units of  $\pi$ , and they have a local maximum for  $\theta \sim 0.4$ . On the other hand, the magnitude of the shifts caused by the C atom (b) have a more complex structure than (a). One observes regions where the interaction is small, and it grows at  $\theta \sim 0.25, 0$ . This also happens for angles  $\sim 1/2$ . In Fig. 3.1 (c) and (d) one observes the evolution of effective interactions. Rashba SO and SC gap (c) have an opposite behaviour around  $\theta \sim 0.12$  since the SO grows, while the SC gap is small. As expected, we find that the Rashba SO is zero when the chain is flat because there is no inversion symmetry breaking, and in the same condition the SC gap is maximum

since all the atoms are in contact with the superconductor. The effective interaction produced by the interplay of the magnetic order and atomic SO of Fe atom is shown in (d). We find that this interaction is suppressed when  $\theta \sim 0.1325$ , and grows for large angles. Furthermore, as  $J$  increases,  $\xi_J$  decreases. Then, we expect the exchange interaction to be large enough to suppress this interaction that destroy MBS.

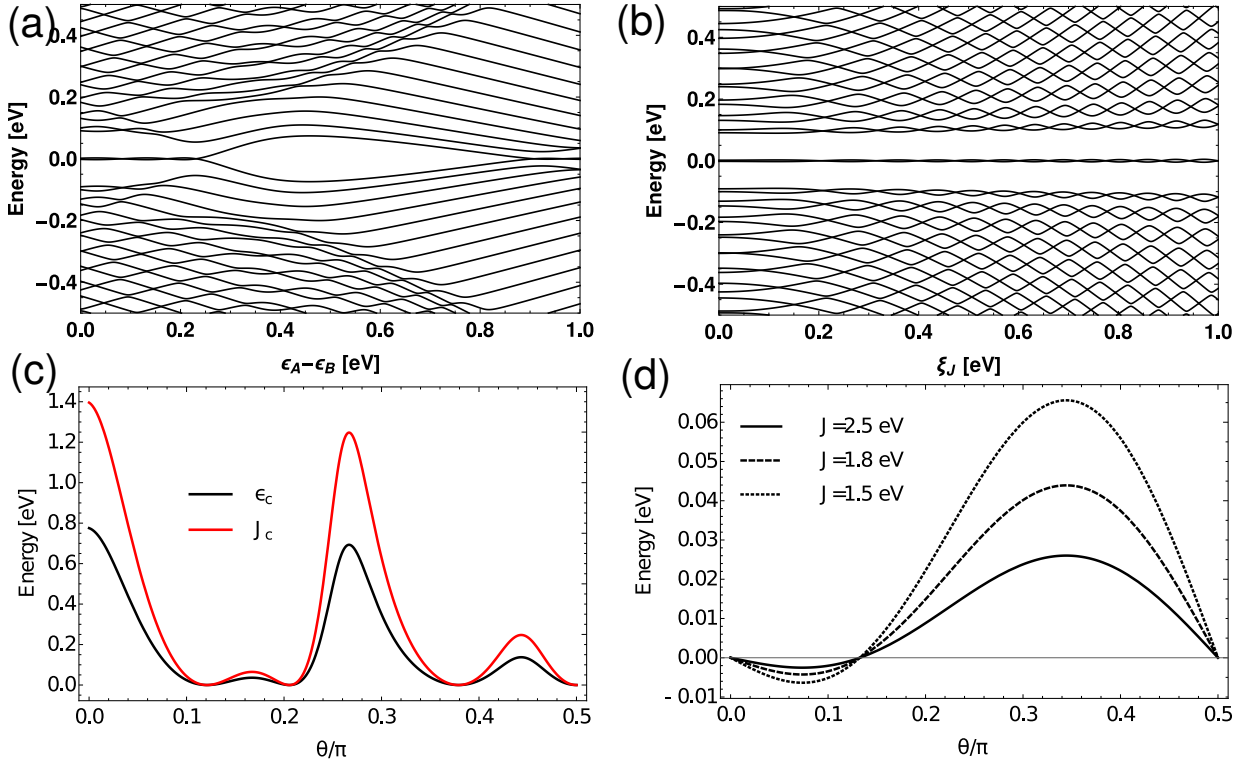


Figure 3.1: Effective interactions as a function  $\theta$ . (a) Magnitude of energy shift in  $d$ -orbitals caused by magnetic order. (b) Magnitude of energy shift in  $\mathbf{B}$  atom due to BF of  $\mathbf{C}$  atom. (c) Rashba SO and SC gap as a function of  $\theta$ . (d) Magnitude of SO-exchange interaction,  $\xi_J$ , as a function of  $\theta$  for different values of  $J$ .

The magnitude of the interactions change in different geometrical configurations and the magnitude in the choose configurations is shown in Table 3.2.

### 3.3.2 Topological phase

To characterize the topological phase of the system one has to calculate a topological invariant quantity, the Pfaffian<sup>13</sup>, from the reciprocal space Hamiltonian. Also, this phase is characterized by the presence of zero-energy states that correspond to MBS. Here choose the second criteria to characterize the topological phase of the system. However, we must establish a criteria for the energy difference between the two lowest energy states because this difference

Table 3.2: Calculated effective SO and SC interactions for two different angular configurations of the atomic chain and for  $\Delta = 0.05$  eV. Atomic and SK parameters were taken from Table 3.1.

Parameter	$\theta = 0.09$	$\theta = 0.1325$	$\theta = 0.25$
$\xi$	2 meV	8 meV	8 meV
$\xi_J$	4 meV	4 $\mu$ eV	29 meV
$\Delta_x$	0.53 eV	0.15 eV	0.23 eV

changes due to energy shifts and SO-exchange effective interactions.

### Angular dependence

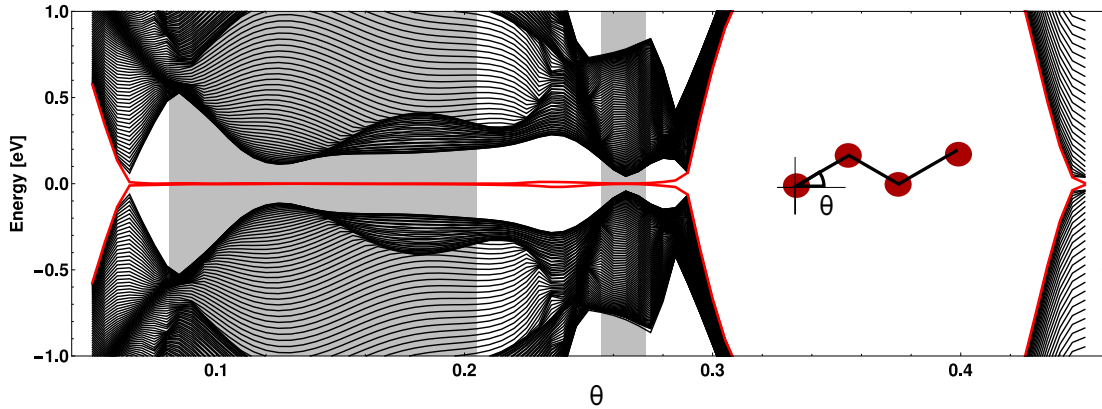


Figure 3.2: Low energy spectra for an atomic chain of  $L = 200$  sites with parameters from Table 3.1, and  $J = 1.5$  eV. The two lowest states are shown in red. The shaded gray region is considered the topological phase of the system and the energy difference between these two states is 0.005 eV.

Let us start by calculating the low-energy spectra of the system as a function of the chain angle  $\theta$ . In Fig. 3.2 one can observe that there are two states around zero energy. However, when one zooms in (Fig. 3.3) one finds the following: i) Particle-hole symmetry was broken, ii) and the shift between them is irregular. This irregular structure does not correspond to previous analyzed shifts such as the MBS oscillations caused by finite overlaps of MBS wavefunctions. Furthermore, when one observes the wavefunctions corresponding to these states (Fig. 3.6 and 3.7), one finds that they are localized wavefunctions with no overlap. We argue that this structure appears due to the interplay between the effective energy shifts and SO-exchange interaction, while the strong localization is due to effective Rashba SO and SC gap. To support such idea, one observes that the shift is minimum for  $\theta \sim 0.1325$  that corresponds to the zero of the  $\xi_J$  interaction. The small remaining shift arises due to energy differences between

sites **A** and **B**. On the other hand, in the range  $\theta : [0.2, 0.45]$  the dominant shift is the one produced from the **C** atom because it corresponds to the region where it is maximum as shown in Fig. 3.1.

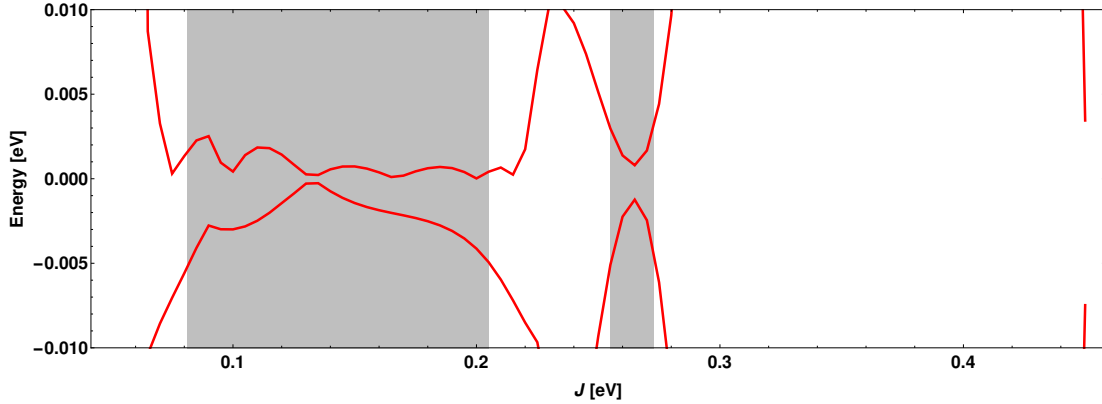


Figure 3.3: Zoom of the zero-energy states in Fig. 3.2.

In this manner, we find that the angles where energy shift between zero-energy states is small are  $\theta \sim [0.05, 0.2]$ . In this region the shift between the two atomic sites is small and the SO-exchange interaction dominates. We suspect that these states are topologically protected MBS, but they could be Shiba states that are strongly spin polarized as the ferromagnetic order<sup>50,52,53</sup>. This is possible since the effect of  $\xi_J \sigma_z$  causes shift between spin up and down states. This SO-exchange interaction creates conduction channels for electrons rather than an effective field along  $z$  direction. In any case, a confirmation of these assumptions can be obtained by calculating the Pfaffian and confirm that these states are MBS or not. Here we choose two angular configurations that may host MBS given by  $\theta = 0.1325\pi$  and  $\theta = 0.09\pi$  that are labeled **1** and **2** respectively.

### Exchange Interaction

We explore the low-energy spectra as a function of the exchange interaction  $J$ , and find a topological phase as was previously described in literature<sup>15,49,54</sup> for MBS. First, in Fig. 3.4, we analyze the configuration **1**, and we find a clear zero energy gap where the criteria for the topological phase is an energy difference of the order  $\sim 10^{-7}$  eV. In this configuration, we minimize the effect of the SO-exchange effective interaction as shown in Fig. 3.1 (d). Nonetheless, precise values for  $J$  coming from DFT<sup>2</sup> calculations ( $J = 2.4$  eV) do not have zero-energy excitations. We find such excitations for smaller values. In any case, the difference of our values can be explained from the approximation order that we have used because it misses higher order corrections that stabilize this value around the realistic value. On the other hand, a dimensionality argument can be used to propose a smaller value for  $J$  since it is directly related with the number of nearest neighbors. Also, most of DFT<sup>50,55</sup> investigations about Fe systems establish a range for  $J$  between 2 and 3 eV. Then, the used values of  $J$  that have zero-energy states are based on reasonable assumptions and lie very close to experimental measurements and computational simulations.

Nonetheless, the role of  $\xi_J$  manifests immediately after we move from  $\theta \sim 0.1325\pi$ . In Fig. 3.5 one observes

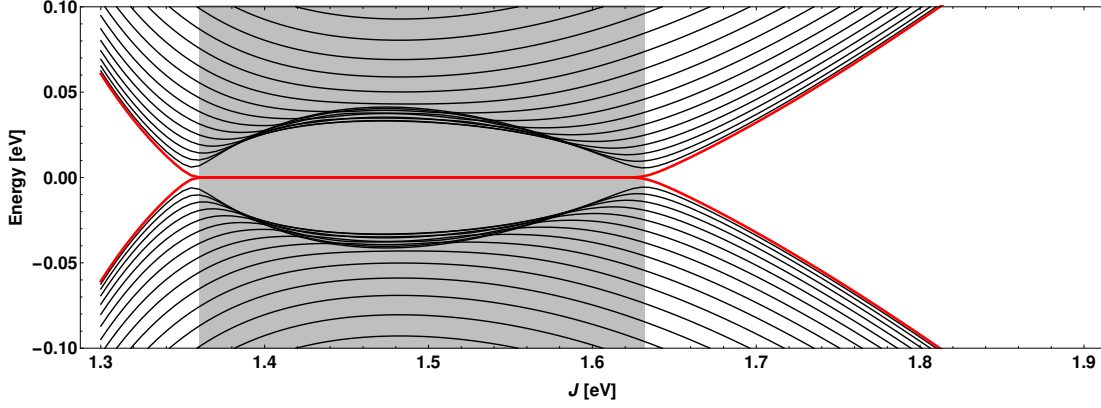


Figure 3.4: Low-energy spectra a s function of  $J$ , angular configuration **1**, and  $\Delta=0.05$  eV. Criteria for the shaded region (topological phase) was  $10^{-7}$  eV.

that the gap between zero-energy states is clearly noticeable in the range of meV. Then, we note that even when  $\xi_J$  is small it generates an effective shift destroying the nature of zero-energy states by a finite gap.

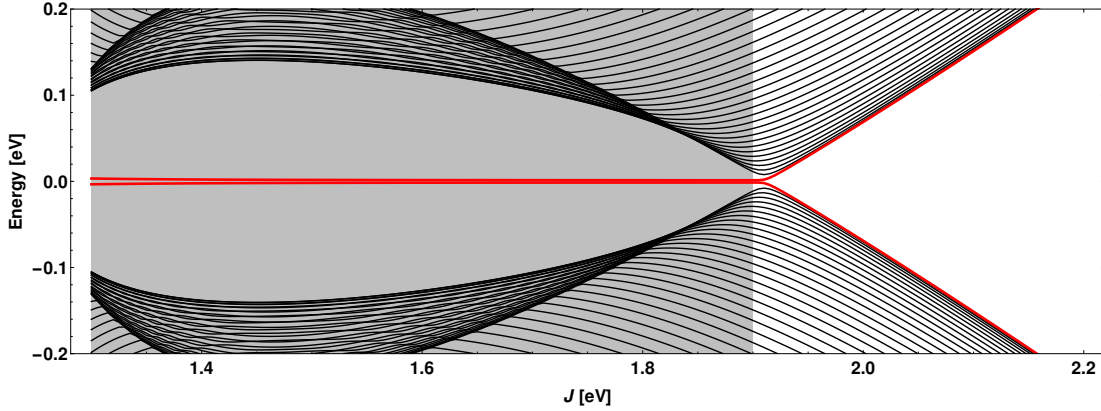


Figure 3.5: Low-energy spectra a s function of  $J$ , angular configuration **2**, and  $\Delta=0.3$  eV. Criteria for the shaded region (topological phase) was 5 meV.

In conductance measurements of this system, one finds a clear peak around zero energy in the range on the meV. Then, this interaction must vanish in order to support zero energy modes. Here we propose several mechanisms that may account for the cancelation of this term. If one observes Table 2.2 and 2.3 one finds that there is a SO term proportional to  $\sigma_z$  within  $d$ -orbitals of the  $\pi$  band. However, when  $\theta = \pi/4$  the coupling between these orbital is zero, and then it is not included in the initial Hamiltonian Eq. 2.88. In angular configurations **1** and **2**, this term is non-zero, and then it competes with the SO-exchange interaction. Then, it is plausible to consider that this term is

a representation of the internal effective processes of the system, but due to limitations of the model this term does not vanish.

### 3.3.3 Wavefunctions of MBS

In spite of the energy shift between the two zero-energy modes, one can find localized wavefunctions corresponding to these states. Here in Fig. 3.6 and 3.7 one observes that when the system is in the topological phase, there are localized states at the ends of the wire. The localization length of these states is mainly characterized by the SC gap as we can observe in both figures<sup>50</sup>. Nonetheless, the dependence of length of such states does not changes in a linear fashion, but in a rather complicated way related with the divergences at the denominators of Eq. 2.90. Then, we find that the value for the atomic SO coupling of Pb is strongly related to the localization length of MBS not directly, but through the effective quantities.

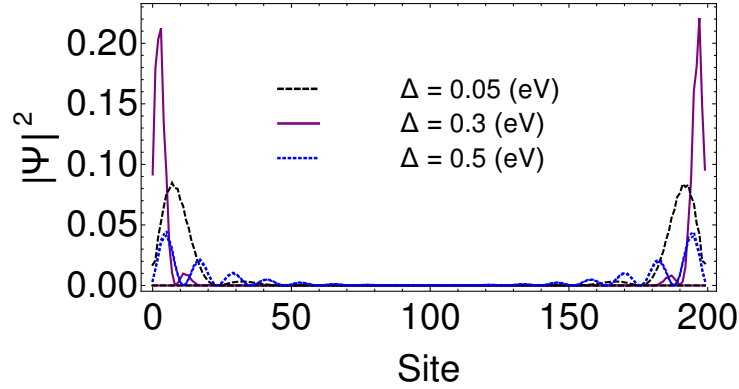


Figure 3.6: Wavefunctions of the two lowest energy states in angular configuration **1**, and  $J = 1.5$  eV.

Also, we are able to explore the influence of  $\theta$  on the properties of MBS such as the localization length. We find that there is no major changes in this length for a smaller angle by observing Fig. 3.6 and 3.7. In fact, we note that smaller angles will enhance the localization of MBS but for a small factor of  $\sim 5$  sites for  $\theta = 0.05\pi$  that changes for different values of  $\Delta$ . We expect that an almost flat configuration will host localized MBS that may correspond to experimental measurements.

In summary, we find that the localization length of MBS is controlled by the superconducting gap  $\Delta$ , while the Rashba SO,  $\xi$ , and the exchange interaction,  $J$ , control the oscillations within this length. The experimentally measured SC gap for Pb atoms was found to be  $\Delta_{exp} = 1.5^{2,50}$  meV, but we find no MBS for this value. Then, we explore larger values for the SC gap. We are able to explore a reasonable range of values for several quantities, such as  $\Delta$ , since the nature of this model is a first order approximation coming from BF. Then, it is expected to have significant differences between the experimental values and the ones that we use. Furthermore, these deviations do not suppress the validity of our model, since there are several processes and interactions that we are not considering and are relevant for the realistic system.

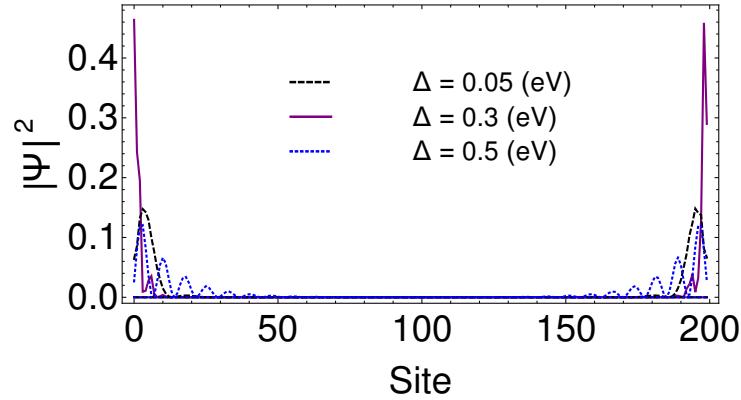


Figure 3.7: Wavefunctions of the two lowest energy states in angular configuration **2**, and  $J = 1.8$  eV.

### 3.3.4 Local Density of States

By solving Eq. 3.1, we obtain information about the spectra and the spatial distribution of states from their wavefunctions. Then, we are able to reconstruct the local density of states (LDOS) that gives the amplitude of probability at a given position and energy. This results have no temperature dependence. However, we do not have access to all energies, but rather to the definite energies of the available states. This is not a problem out of the gap since there is a continuum of energies that create each band, but inside the SC gap we can only access to two finite values corresponding to the eigenenergies of the lowest states. On the other hand, a full LDOS can reproduce the energy width of states and include thermal broadening. For such reason, we set an energy width of 2 meV<sup>50,51</sup> for the lowest energy state that is in the range of current experimental techniques of STM with normal tips. If one uses superconducting tips for STM the resolution is much precise  $\sim \mu\text{eV}$ <sup>50</sup>.

In Fig. 3.8 one observes a 3D plot of the LDOS where the  $x$  and  $y$  axis represent energy and position, and the  $z$  axis represent the amplitude of the wavefunction. One observes that out of the gap there are delocalized excitations (orange) that create the bands of ground state Cooper pairs and quasiparticle excitations. Inside the gap, one observes a flat space where no states live, but close to zero energy, there are two states localized at the ends of the atomic wire. This illustrative image shows the nature of MBS: they appear inside the SC gap as a consequence of the topological properties of the system with a highly local character. In the Majorana representation, each of these particles represents half a fermion that is left at the end of the wire due to the pairing between electrons as in the SSH model (see Appendix D).

### 3.3.5 Experimental Signatures: STM measurements

Using the previous discussed considerations about the influence of  $\xi_J$ , and setting the energy resolution to 2 meV, we are able to construct the STM measurement at zero K for the zero energy states of the system and show them for different range of values in Fig. ???. There was a lot of attention about STM measurement of zero-energy modes

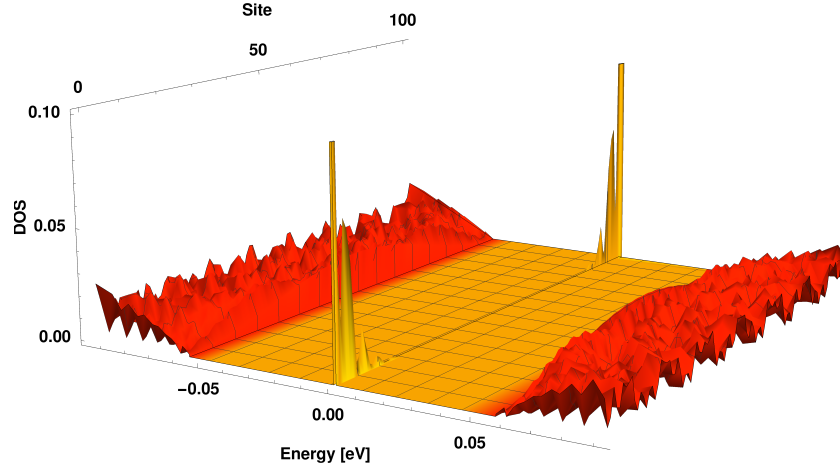


Figure 3.8: Illustrative image of the local density of states of an atomic chain of 100 sites of length. Axes in plane represent position (atomic sites) and energy (eV), and vertical axis represents  $|\Psi|^2$ . States out of the gap are orange, while in gap states are yellow. Parameters used are within the topological regime, but without discussion purposes.

recently. The most remarkable property is the high localization of zero-energy modes<sup>2</sup> that has not been addressed by current models<sup>25</sup>. According to recent measurements, the localization length of this states was found to be  $\sim 1$  nm. Here in Fig. ?? we show the STM prediction for four different configurations of parameters. In (a) and (b) we use the angular configuration **1**, and change the SC gap from  $\Delta = 0.3$  and  $\Delta = 0.01$  respectively. We find that the larger the gap, the strongest the localization of zero-energy modes. If the gap decreases by an order of magnitude we may expect oscillations of the LDOS, but no significant change in localization since it still decays very fast. In (b) and (c) we show the angular configuration **2**, and find similar properties than in **1**. We find that in this configuration the localization of zero-energy modes is even higher than before. Then, one observes that the geometrical configuration of the chain has a direct effect on the MBS properties such as the localization length. Remarkably, in (d) one find that the localization length is  $\sim 1$  nm.



## Chapter 4

# Conclusions & Outlook

We have derived the physics for Majorana bound states from a microscopic model in the tight binding Slater Koster approach. The model is guided by experimentally feasible Fe low dimensional structure on a Pb superconducting surface. This configuration allows to build a Kitaev-like model that incorporates superconducting correlations onto a ferromagnetic system by proximity effects. The developed model is the first derivation of the Kitaev-like model from an actual physical system. The great advantage of the developed model is that it allows to tune the parameters of the experimental setup in order to achieve optimal Majorana excitations, such as manipulate the positions of the atoms in the Fe chain using mechanical deformations.

The proximity effect was modeled as pure kinetic interaction between  $p$  and  $d$  orbitals, and the superconducting correlations show  $s$ -wave superconductivity from band folding. There are two kinds of effective SO interactions that interplay in the properties of the MBS. The SO from Fe and the SO from Pb are modified by the geometrical nature of the structure. We have shown that the most important SO contribution and proximity induced SC appear because of the high degree of hybridization between  $p$  and  $d$  orbitals.

It is worth to consider if the missing orbitals would produce a significant difference between this model and the real system. However, we have estimated that the interactions with the  $\delta$  band will produce an effective spin interaction proportional to  $\sigma_y$ , which will enhance the Rashba interaction, and another spin interaction proportional to  $\sigma_z$  that is not relevant for this work. Nevertheless, considering only linear contribution of SK terms from the  $\delta$  band will only produce corrections to the energy and hopping terms. Therefore, the relevant physics of the Rashba SO interaction between the chain and the surface, and the intrinsic SO interaction from the  $\sigma$  subspace are well described by our model.

An asymmetry between the two sites of the effective Hamiltonian makes impossible for the MBS to appear exactly at zero energy. To solve this problem we rely on mechanical deformations of the atomic chain that change the angle or length. Then, MBS appear at optimal structural conditions within the topological phase. This allows us to explore different configurations that host MBS and compare their properties. The optimal geometrical configuration for the atomic chain considers an angle of  $\theta = 0.28\pi$ . It enhances the Rashba SO interaction and decreases the energy shift and the intrinsic SO interaction. MBS in this geometrical configuration will be highly localized at the ends of the

wire, and there will be an energy shift between them that is small compared with the superconducting gap.

The role of Rashba SO is to determine the localization length of MBS, which must be considered as an important factor when determining the length of the wire. In principle, the intrinsic SO interaction does not affect MBS until it reaches the same energy scale as the Rashba SO. For this system, a chain of  $L = 100$  sites will host MBS has edge states. For sufficiently strong exchange interaction of Fe atoms, the topological phase is realizable.

This model can be further analyzed to obtain insight in the physics of MBS. There are several possibilities that are not explored in deep in this work. First, this system represents a static setup where we analyze the states and energies at equilibrium, but other features of MBS emerge in transport problems. In future works based on this thesis, one expects to find a zero bias peak in the conductance, a property that is characteristic of MBS. Also, the influence of other states can be analyzed in order to exclude signatures of Andreev bound states or Shiba states. The formalism required to describe the transport properties is based on Green's functions methods, but it is beyond the scope of this work that is focused on an analytical microscopic tight binding model. There are different features of the system that are not calculated or well described in this work. An analytic form for the MBS wavefunctions is required in order to understand the role of intrinsic and Rashba SO in the problem. Also, the Bloch expansion of the system is required to calculate the topological invariant of Majorana systems, the Pfaffian. Finally, different geometrical configurations can host different species of MBS, and their origin in the Slater Koster interaction can be studied. At this point we can propose different experimental setups where the atomic chain is manipulated by different methods such as mechanical deformations. Also, one can explore if the topological phase of each stable geometrical configuration produces changes and allow different values of  $J$ . Then, different species of topological regimes could be found in feasible experimental conditions, and our predictions could be confirmed.

In summary, the Kitaev toy model was effectively obtained from a big physical system, and the parameters give insight into the geometrical details. The proximity effect is studied as a function of the microscopic details and can be manipulated by moving the system. A particular structure optimized for MBS is proposed and studied. It shows the expected MBS highly localized at the wire ends. Further analysis are required for a complete understanding of the electronic interactions and geometrical details in this model.

## Appendix A

# Spin Orbit Interaction

The Spin Orbit Interaction (SOI) is a relativistic quantum mechanical effect. It couples the spin of the electron to the internal magnetic field of the nuclei. In the tight-binding context, it promotes transitions between spin eigenstates. In other words, it flips the spin of the electron in a transition from one orbital to another. The SOI term is the following,

$$\begin{aligned} H_{SOI} &= \frac{e}{2m_o^2c^2}(\nabla V \times \mathbf{p}) \cdot \mathbf{S} \\ &= \frac{1}{r} \frac{\partial V}{\partial r} \frac{e}{2m_o^2c^2} \mathbf{L} \cdot \mathbf{S} \\ &= \lambda \mathbf{L} \cdot \mathbf{S} \\ &= \frac{\lambda}{2}(L_+S_- + L_-S_+ + 2L_zS_z) \end{aligned} \tag{A.1}$$

Where  $V$  is the electrostatic potential in radial coordinates,  $m_o$  is the rest electron mass,  $e$  is the charge of the electron,  $\mathbf{S}$  and  $\mathbf{L}$  are the spin and orbital angular momentum operators. The last expression is in terms of the ladder operators. It can be used to compute the matrix elements between d-orbitals using the following eigenvalue equations,

$$\mathbf{L}_{\pm}|lm\rangle = \hbar \sqrt{l(l+1) - m(m \pm 1)}|lm \pm 1\rangle \tag{A.2}$$

$$\mathbf{S}_{\pm}|m_s\rangle = \hbar \sqrt{s(s+1) - m_s(m_s \pm 1)}|m_s \pm 1\rangle \tag{A.3}$$

$$\mathbf{L}_z|lm\rangle = m\hbar|lm\rangle \tag{A.4}$$

$$\mathbf{S}_z|m_s\rangle = m_s\hbar|m_s\rangle \tag{A.5}$$

Since there are two electrons with opposite spin per orbital, we must include the space of spin eigenstates  $|sm_s\rangle = \{|\uparrow\rangle, |\downarrow\rangle\}$ . The new space of solutions is given by  $|lm\rangle \otimes |sm_s\rangle$ . Apply  $H_{SOI}$  to the d-orbitals with spin yields,

$$\begin{aligned} H_{SOI}|d_{xy}\uparrow\rangle &= \xi_P[(|d_{yz}\rangle + i|d_{xz}\rangle)|\downarrow\rangle + i|d_{x^2-y^2}\rangle|\uparrow\rangle] \\ H_{SOI}|d_{xy}\downarrow\rangle &= \xi_P[(|d_{yz}\rangle + i|d_{xz}\rangle)|\uparrow\rangle - i|d_{x^2-y^2}\rangle|\downarrow\rangle] \end{aligned} \quad (\text{A.6})$$

$$\begin{aligned} H_{SOI}|d_{yz}\uparrow\rangle &= \xi_P[(\sqrt{3}|d_{z^2}\rangle + |d_{xy}\rangle + i|d_{x^2-y^2}\rangle)|\downarrow\rangle - |d_{xz}\rangle|\uparrow\rangle] \\ H_{SOI}|d_{yz}\downarrow\rangle &= \xi_P[(\sqrt{3}|d_{z^2}\rangle + |d_{xy}\rangle + i|d_{x^2-y^2}\rangle)|\uparrow\rangle + |d_{xz}\rangle|\downarrow\rangle] \end{aligned} \quad (\text{A.7})$$

$$\begin{aligned} H_{SOI}|d_{z^2}\uparrow\rangle &= \xi_P\sqrt{3}(|d_{yz}\rangle - i|d_{xz}\rangle)|\downarrow\rangle \\ H_{SOI}|d_{z^2}\downarrow\rangle &= \xi_P\sqrt{3}(|d_{yz}\rangle + i|d_{xz}\rangle)|\uparrow\rangle \end{aligned} \quad (\text{A.8})$$

$$\begin{aligned} H_{SOI}|d_{xz}\uparrow\rangle &= \xi_P[(\sqrt{3}|d_{z^2}\rangle + |d_{xy}\rangle - i|d_{x^2-y^2}\rangle)|\downarrow\rangle - |d_{yz}\rangle|\uparrow\rangle] \\ H_{SOI}|d_{xz}\downarrow\rangle &= \xi_P[(\sqrt{3}|d_{z^2}\rangle + |d_{xy}\rangle - i|d_{x^2-y^2}\rangle)|\uparrow\rangle + |d_{yz}\rangle|\downarrow\rangle] \end{aligned} \quad (\text{A.9})$$

$$\begin{aligned} H_{SOI}|d_{x^2-y^2}\uparrow\rangle &= \xi_P[(|d_{yz}\rangle - i|d_{xz}\rangle)|\downarrow\rangle - |d_{xy}\rangle|\uparrow\rangle] \\ H_{SOI}|d_{x^2-y^2}\downarrow\rangle &= \xi_P[(|d_{yz}\rangle - i|d_{xz}\rangle)|\uparrow\rangle + |d_{xy}\rangle|\downarrow\rangle] \end{aligned} \quad (\text{A.10})$$

The SOI coupling between d orbitals can be obtained by calculating the matrix elements of  $H_{SOI}$ . It is easy to see that the diagonal elements are zero. That is, there are no spin transitions in the same orbital. The non-zero elements are shown below,

$$\langle d_{xy}|H_{SOI}|d_{x^2-y^2}\rangle = 2i\hat{\sigma}_z\xi_P \quad (\text{A.11})$$

$$\langle d_{yz}|H_{SOI}|d_{xz}\rangle = i\hat{\sigma}_z\xi_P \quad (\text{A.12})$$

$$\langle d_{xy}|H_{SOI}|d_{z^2}\rangle = -i\sqrt{3}\hat{\sigma}_x\xi_P \quad (\text{A.13})$$

$$\langle d_{yz}|H_{SOI}|d_{x^2-y^2}\rangle = -i\hat{\sigma}_x\xi_P \quad (\text{A.14})$$

$$\langle d_{xz}|H_{SOI}|d_{x^2-y^2}\rangle = -i\hat{\sigma}_y\xi_P \quad (\text{A.15})$$

## Appendix B

# Tight-Binding Method

This method allows to describe a translational invariant system as a lattice. In the general case, consider  $n$  atomic orbitals  $|\phi_j(\mathbf{r})\rangle$  at each lattice point where  $j = 1, \dots, n$ . Because of translational symmetry, the system is invariant under transformations of  $\mathbf{r} \rightarrow \mathbf{r} + \mathbf{R}_i$ . Bloch theorem holds in this model. Then, the Bloch theorem allows us to express the system in terms of Bloch functions  $|\Phi(\mathbf{r}, \mathbf{k})_j\rangle$ . They are defined as:

$$|\Phi(\mathbf{r}, \mathbf{k})_j\rangle = \frac{1}{\sqrt{N}} \sum_{i=1}^N e^{i\mathbf{k}\cdot\mathbf{R}_{ji}} |\phi_j(\mathbf{r} - \mathbf{R}_{i,j})\rangle \quad (\text{B.1})$$

where  $N$  is the number of unit cells in the system,  $\mathbf{r}$  and  $\mathbf{k}$  represent the real and momentum space vectors respectively, and  $\mathbf{R}_{i,j}$  represents the  $j$ -th orbital in the  $i$ -th unit cell. Bloch functions Eq. B.1 are a set of basis functions that can be used to write the general solution of the system as:

$$|\Psi_i(\mathbf{r}, \mathbf{k})\rangle = \sum_l c_{i,l}(\mathbf{k}) |\Phi_l(\mathbf{r}, \mathbf{k})\rangle \quad (\text{B.2})$$

Let's consider the Schrodinger equation in momentum space,

$$\mathcal{H}(\mathbf{k})|\Psi_i(\mathbf{k})\rangle = E_i(\mathbf{k})|\Psi_i(\mathbf{k})\rangle \quad (\text{B.3})$$

Then, by taking the inner product with  $\langle\Psi_i(\mathbf{k})|$ , the energy is given by,

$$E_i(\mathbf{k}) = \frac{\langle\Psi_i(\mathbf{k})|\mathcal{H}(\mathbf{k})|\Psi_i(\mathbf{k})\rangle}{\langle\Psi_i(\mathbf{k})|\Psi_i(\mathbf{k})\rangle} \quad (\text{B.4})$$

Then, by substituting Eq. B.2, the energy becomes,

$$E_i(\mathbf{k}) = \sum_{l,m} \frac{c_{i,l}^* c_{i,m} \langle\Phi_l(\mathbf{r}, \mathbf{k})|\mathcal{H}|\Phi_m(\mathbf{r}, \mathbf{k})\rangle}{c_{i,l}^* c_{i,m} \langle\Phi_l(\mathbf{r}, \mathbf{k})|\Phi_m(\mathbf{r}, \mathbf{k})\rangle} \quad (\text{B.5})$$

Let's define  $H$  and  $S$  as the transfer and direct matrices respectively. Their matrix elements are given as,

$$H_{ij} = \langle\Phi_j|\mathcal{H}|\Phi_i\rangle \quad S_{ij} = \langle\Phi_j|\Phi_i\rangle \quad (\text{B.6})$$

Then, the energy is given as,

$$E_j(\mathbf{k}) = \sum_{i,l} \frac{c_{j,l}^* c_{j,i} H_{i,l}}{c_{j,l}^* c_{j,i} S_{i,l}} \quad (\text{B.7})$$

Following a variational approach, we minimize the equation with respect to one of the parameters,

$$\frac{\partial E_j}{\partial c_{j,m}^*} = \frac{\sum_l c_{j,l} H_{m,l}}{\sum_{i,l} c_{j,l}^* c_{j,i} S_{i,l}} - \frac{\sum_l c_{j,l} S_{m,l} \sum_{i,l} c_{j,l}^* c_{j,i} H_{i,l}}{\left(\sum_{i,l} c_{j,l}^* c_{j,i} S_{i,l}\right)^2} = 0 \quad (\text{B.8})$$

Then,

$$\sum_l c_{j,l} H_{m,l} = E_j \sum_l c_{j,l} S_{m,l} \quad (\text{B.9})$$

Consider that there are  $j$ -bands in the system. Each one has its energy dispersion relation  $E_j(\mathbf{k})$ . Consider that there are  $m$ -orbitals per lattice point. For two orbitals per unit cell,  $m = 1, 2$ , the system of equations can be written in matrix form as:

$$\begin{bmatrix} H_{11} & H_{12} \\ H_{21} & H_{22} \end{bmatrix} \begin{bmatrix} c_{j1} \\ c_{j2} \end{bmatrix} = E_j \begin{bmatrix} S_{11} & S_{12} \\ S_{21} & S_{22} \end{bmatrix} \begin{bmatrix} c_{j1} \\ c_{j2} \end{bmatrix} \quad (\text{B.10})$$

We have arrived to an effective Schrodinger equation, which can be written as,

$$H\Psi_j = E_j S\Psi_j \quad (\text{B.11})$$

The problem of solving the Schrodinger equation in a system with traslational invariance has reduced to obtaining the components of H and S.

## B.1 Direct Integral Matrix

Consider a system, as before, with two different orbitals per atom. The orbitals are labeled as A and B. The diagonal terms of H are given by,

$$H_{AA} = \frac{1}{N} \sum_{i=1}^N \sum_{j=1}^N e^{i\mathbf{k}\cdot(\mathbf{R}_i - \mathbf{R}_j)} \langle \phi_A(\mathbf{r} - \mathbf{R}_j) | \mathcal{H} | \phi_A(\mathbf{r} - \mathbf{R}_i) \rangle \quad (\text{B.12})$$

$H_{AA}$  refers to the matrix element that connects A-orbitals. This sum counts the interaction of every A orbital, with every other one of the same specie. For the diagonal terms, we assume that most of the interaction comes from the same atom. Since the contribution of each atom is independent from one another, we sum up their contributions. The diagonal terms correspond to the energy of the orbital.

$$H_{AA} \approx \frac{1}{N} \sum_{i=1}^N \langle \phi_A(\mathbf{r} - \mathbf{R}_i) | \mathcal{H} | \phi_A(\mathbf{r} - \mathbf{R}_i) \rangle = \frac{1}{N} \sum_{i=1}^N \epsilon = \epsilon \quad (\text{B.13})$$

The non-diagonal terms represent the interaction between A and B orbitals. They are given by,

$$H_{AB} = \frac{1}{N} \sum_{i=1}^N \sum_{j=1}^N e^{i\mathbf{k}\cdot(\mathbf{R}_{Bi} - \mathbf{R}_{Aj})} \langle \phi_A(\mathbf{r} - \mathbf{R}_{Aj}) | \mathcal{H} | \phi_B(\mathbf{r} - \mathbf{R}_{Bi}) \rangle \quad (\text{B.14})$$

We assume the nearest neighbor approximation to first order. That is, the orbitals interact mainly with their first nearest neighbors. The connection to each neighbor is given by the vectors  $\delta_j$ . The interaction with each neighbor depends on the geometry of the system, then, it can be expressed using the Slater Koster parameters.

$$H_{AB} \approx \frac{1}{N} \sum_{i=1}^N \sum_{\langle j \rangle} e^{i\tau_j} E_{AB}^j \quad (\text{B.15})$$

## B.2 Overlap Integral Matrix

The diagonal terms of S are given by,

$$S_{AA} = \frac{1}{N} \sum_{i=1}^N \sum_{j=1}^N e^{i\mathbf{k} \cdot (\mathbf{R}_i - \mathbf{R}_j)} \langle \phi_A(\mathbf{r} - \mathbf{R}_j) | \phi_A(\mathbf{r} - \mathbf{R}_i) \rangle \quad (\text{B.16})$$

Following the same approximation as for the Direct Integral Matrix,

$$S_{AA} \approx \frac{1}{N} \sum_{i=1}^N \langle \phi_A(\mathbf{r} - \mathbf{R}_i) | \phi_A(\mathbf{r} - \mathbf{R}_i) \rangle = \frac{1}{N} \sum_{i=1}^N 1 = 1 \quad (\text{B.17})$$

If we consider that the orbitals are orthogonal, the non-diagonal terms of S will be zero. Assuming that they are non-zero, in the nearest neighbor approximation, the Overlap Integral Matrix elements are given by,

$$S_{AB} = \frac{1}{N} \sum_{i=1}^N \sum_{j=1}^N e^{i\mathbf{k} \cdot (\mathbf{R}_{Bi} - \mathbf{R}_{Aj})} \langle \phi_A(\mathbf{r} - \mathbf{R}_{Aj}) | \phi_B(\mathbf{r} - \mathbf{R}_{Bi}) \rangle \approx \frac{1}{N} \sum_{i=1}^N \sum_{\langle j \rangle} e^{i\tau_j} s_0 \quad (\text{B.18})$$

Considering that the contribution of each atoms is independent from other atoms, we have that,

$$S_{AB} = s_0 \sum_{\langle j \rangle} e^{i\tau_j} \quad (\text{B.19})$$

Finally, the full problem of solving a traslational invariant system has reduced to obtaining an expression for Eq. B.13, Eq. B.15, Eq. B.17 and Eq. B.19. It is important to remember that we are allowed to do this because of Bloch's theorem. Also, some approximations are involved that restrict us. Special attention should be taken to remain inside the approximation validity range.



## Appendix C

# Theory of Superconductivity

It has been demonstrated that after cooling below some critical temperature,  $T_C$ , some materials show zero static electrical resistivity, and expulsion of the magnetic field<sup>56</sup>. In fact, superconducting systems are characterized by a gap  $\Delta$  that separates the ground states from the quasiparticle excited states<sup>57</sup>. A short review starts with the experimental discovery of the Meissner effect<sup>58</sup>. From the theoretical approach, the most relevant phenomenological theory came from London<sup>59</sup>. His ideas were led by the Bose-Einstein condensation phenomena which was discovered by that time. He was able to relate a superfluid of fermions with the classical Drude picture. In fact, his theory explained that a magnetic field decays exponentially inside a superconductor. However, microscopic insight was required to fully understand superconductivity. An important contribution came from the mean field theory of phase transition of Landau<sup>60</sup>. The Anderson-Higgs mechanism explained that the force carriers of the electromagnetic field become massive inside a superconductor<sup>56,61</sup> and thus the field decays. A definitive description of low-temperature superconductors was proposed by Bardeen, Cooper and Schriffer in 1957<sup>62</sup>. In this section we treat the equations of BCS theory and discuss the most relevant facts of superconductivity. Furthermore, a brief discussion of p-wave and s-wave pairing is included.

### C.1 BCS Theory

The particles that contribute to the current in a superconductor are not electrons, but pairs of electrons called "Cooper Pairs"<sup>62</sup>. Although electrons are repulsive between each other, an attractive interaction can be effectively obtained from electron-phonon interaction<sup>56</sup>. It is all about the time scales for the moving electrons and the vibrating cores. The velocity of the cores depends on the Debye frequency,  $\omega_D$ , and in general, electrons are  $10^2$  times faster than cores<sup>57</sup>. Such difference allows electrons to move in an effective attractive potential. A detailed derivation of the attractive interaction made by electron-phonon interaction can be found in the lecture notes of Caster Timm about superconductivity<sup>56</sup>.

### C.1.1 BCS Ground State

A Cooper pair is made up of two electrons that corresponds to states  $|\mathbf{k}, \uparrow\rangle$  and  $|\mathbf{-k}, \downarrow\rangle$ . We define a Cooper pair creation operator as,

$$\hat{P}_{\mathbf{k}} = \hat{c}_{\mathbf{k}\uparrow}^\dagger \hat{c}_{-\mathbf{k}\downarrow}^\dagger \quad (\text{C.1})$$

The ansatz proposed<sup>57</sup> by Bardeen, Copper, and Schriffier is,

$$|\Psi_{BCS}\rangle = \prod_{\mathbf{k}} C_{\mathbf{k}} e^{\alpha_{\mathbf{k}} \hat{P}_{\mathbf{k}}} |0\rangle \quad (\text{C.2})$$

It is easy to see that,  $(\hat{P}_{\mathbf{k}})^2 = 0$ , since it would be creating on occupied states. Then, we can expand Eq. C.2 as a Taylor series up to first order. That is,

$$|\Psi_{BCS}\rangle = \prod_{\mathbf{k}} C_{\mathbf{k}} (1 + \alpha_{\mathbf{k}} \hat{P}_{\mathbf{k}}) |0\rangle \quad (\text{C.3})$$

To determine the constants, normalization is imposed in the ground state as  $\langle \Psi_{BCS} | \Psi_{BCS} \rangle$ . Directly, we obtain that,

$$1 = |C_{\mathbf{k}}|^2 \langle 0 | (1 + \alpha_{\mathbf{k}}^* \hat{P}_{\mathbf{k}}^\dagger) (1 + \alpha_{\mathbf{k}} \hat{P}_{\mathbf{k}}) |0\rangle = |C_{\mathbf{k}}|^2 (1 + |\alpha_{\mathbf{k}}|^2) \quad (\text{C.4})$$

Then,

$$|C_{\mathbf{k}}| = \frac{1}{\sqrt{1 + |\alpha_{\mathbf{k}}|^2}} \quad (\text{C.5})$$

Let's define,

$$u_{\mathbf{k}} = \frac{1}{\sqrt{1 + |\alpha_{\mathbf{k}}|^2}} \quad v_{\mathbf{k}} = \frac{\alpha_{\mathbf{k}}}{\sqrt{1 + |\alpha_{\mathbf{k}}|^2}} \quad (\text{C.6})$$

Finally, the BCS ground state can be written as,

$$|\Psi_{BCS}\rangle = \prod_{\mathbf{k}} (u_{\mathbf{k}} + v_{\mathbf{k}} \hat{c}_{\mathbf{k}\uparrow}^\dagger \hat{c}_{-\mathbf{k}\downarrow}^\dagger) |0\rangle \quad (\text{C.7})$$

From Eq. C.7 we note that this state is different from the usual states in condensed matter. In fact, it only has paired states of fermions. There are no single occupied or empty fermion states. Furthermore, the term  $(u_{\mathbf{k}} + v_{\mathbf{k}} \hat{c}_{\mathbf{k}\uparrow}^\dagger \hat{c}_{-\mathbf{k}\downarrow}^\dagger)$  accounts for all the possible combinations of filled or empty paired states. All this possibilities are encoded in a single wavefunction as the BCS ground state.

### C.1.2 BCS Ground State Energy

The BCS Hamiltonian is written as<sup>62</sup>,

$$H_{BCS} = \sum_{\mathbf{k}\sigma} \xi_{\mathbf{k}} c_{\mathbf{k}\sigma}^\dagger c_{\mathbf{k}\sigma} - \sum_{\mathbf{k}} \Delta_{\mathbf{k}}^* c_{-\mathbf{k}\downarrow} c_{\mathbf{k}\uparrow} - \sum_{\mathbf{k}} \Delta_{\mathbf{k}} c_{\mathbf{k}\uparrow}^\dagger c_{-\mathbf{k}\downarrow}^\dagger \quad (\text{C.8})$$

Where the pairing potential  $\Delta$  depends on temperature. To diagonalize the BCS Hamiltonian we recall the Bogoliubov transformations<sup>57</sup>. The new basis will be written in terms of new creation and annihilation operators,

$$\begin{bmatrix} \gamma_{\mathbf{k}\uparrow} \\ \gamma_{-\mathbf{k}\downarrow}^\dagger \end{bmatrix} = \begin{bmatrix} u_{\mathbf{k}}^* & -v_{\mathbf{k}} \\ v_{\mathbf{k}}^* & u_{\mathbf{k}} \end{bmatrix} \begin{bmatrix} c_{\mathbf{k}}^\dagger \\ c_{\mathbf{k}} \end{bmatrix} \quad (\text{C.9})$$

The new operators  $\{\gamma_{\mathbf{k}\uparrow}, \gamma_{-\mathbf{k}\downarrow}^\dagger\}$  are fermionic operators. That is,  $\{\gamma_{\mathbf{k}\uparrow}, \gamma_{\mathbf{k}\uparrow}^\dagger\} = 1$ . From which follows that,  $|u_{\mathbf{k}}|^2 + |v_{\mathbf{k}}|^2 = 1$ . This transformation exactly diagonalizes the BCS Hamiltonian. For a full derivation we refer the reader to the chapter 10 of Timm's book<sup>56</sup>. That is,

$$H_{BCS} = \sum_{\mathbf{k}\sigma} E_{\mathbf{k}} \gamma_{\mathbf{k}\sigma}^\dagger \gamma_{\mathbf{k}\sigma} \quad (\text{C.10})$$

where  $E_{\mathbf{k}} = \sqrt{\xi_{\mathbf{k}}^2 + |\Delta|^2}$  is the superconducting energy.

## C.2 Bogoliubov-de-Gennes Hamiltonian

The BCS Hamiltonian is valid in momentum space. That is, it represents the bulk of a superconducting system<sup>56,61</sup>. Often there are interesting situations where the system is spatially dependent. For instance, consider Josephson junctions<sup>30</sup> or Andreev reflection processes. At this point, we introduce the BCS Ground State, Eq. C.7, as the eigenstate of Eq. C.8. The resulting equation is in the first quantized form, that is, an eigenvalue equation,

$$H_{BCS} |\Psi_{BCS}\rangle = E_{BCS} |\Psi_{BCS}\rangle \quad (\text{C.11})$$

Note that the pairing terms in Eq. C.8 are bilinear in the creation and annihilation operators. That is, they act linearly in each argument. Consider single particle excitations by defining a two-component spinor,

$$|\Psi\rangle = \begin{bmatrix} |\Psi_1\rangle \\ |\Psi_2\rangle \end{bmatrix} = \begin{bmatrix} c_{\mathbf{k},\uparrow}^\dagger \\ c_{-\mathbf{k},\downarrow} \end{bmatrix} |\Psi_{BCS}\rangle \quad (\text{C.12})$$

Consider the following commutators,

$$\begin{aligned} [H_{BCS}, c_{\mathbf{k}',\uparrow}^\dagger] &= \sum_{\mathbf{k}\sigma} \xi_{\mathbf{k}} c_{\mathbf{k}\sigma}^\dagger [c_{\mathbf{k}\sigma}, c_{\mathbf{k}',\uparrow}^\dagger] - \sum_{\mathbf{k}} \Delta_{\mathbf{k}}^* c_{-\mathbf{k}\downarrow} [c_{\mathbf{k}\uparrow}, c_{\mathbf{k}',\uparrow}^\dagger] - \sum_{\mathbf{k}} \Delta_{\mathbf{k}} [c_{\mathbf{k}\uparrow}^\dagger c_{-\mathbf{k}\downarrow}^\dagger, c_{\mathbf{k}',\uparrow}^\dagger] \\ [H_{BCS}, c_{\mathbf{k}',\uparrow}^\dagger] &= \sum_{\mathbf{k}\sigma} \xi_{\mathbf{k}} c_{\mathbf{k}\sigma}^\dagger \delta_{\mathbf{k},\mathbf{k}'} \delta_{\sigma,\uparrow} - \sum_{\mathbf{k}} \Delta_{\mathbf{k}}^* c_{-\mathbf{k}\downarrow} \delta_{\mathbf{k},\mathbf{k}'} \\ [H_{BCS}, c_{\mathbf{k},\uparrow}^\dagger] &= \xi_{\mathbf{k}} c_{\mathbf{k},\uparrow}^\dagger - \Delta_{\mathbf{k}}^* c_{-\mathbf{k}\downarrow} \end{aligned} \quad (\text{C.13})$$

Also,

$$\begin{aligned} [H_{BCS}, c_{-\mathbf{k}',\downarrow}] &= \sum_{\mathbf{k}\sigma} \xi_{\mathbf{k}} c_{\mathbf{k}\sigma}^\dagger [c_{\mathbf{k}\sigma}, c_{-\mathbf{k}',\downarrow}] - \sum_{\mathbf{k}} \Delta_{\mathbf{k}}^* c_{-\mathbf{k}\downarrow} [c_{\mathbf{k}\uparrow}, c_{-\mathbf{k}',\downarrow}] - \sum_{\mathbf{k}} \Delta_{\mathbf{k}} [c_{\mathbf{k}\uparrow}^\dagger c_{-\mathbf{k}\downarrow}^\dagger, c_{-\mathbf{k}',\downarrow}] \\ [H_{BCS}, c_{-\mathbf{k}',\downarrow}] &= \sum_{\mathbf{k}\sigma} \xi_{\mathbf{k}} c_{\mathbf{k}\sigma}^\dagger \delta_{\mathbf{k},\mathbf{k}'} \delta_{\sigma,\uparrow} - \sum_{\mathbf{k}} \Delta_{\mathbf{k}}^* c_{-\mathbf{k}\downarrow} \delta_{\mathbf{k},\mathbf{k}'} \\ [H_{BCS}, c_{-\mathbf{k},\downarrow}] &= -\xi_{\mathbf{k}} c_{-\mathbf{k},\downarrow} - \Delta_{\mathbf{k}} c_{-\mathbf{k}\downarrow} \end{aligned} \quad (\text{C.14})$$

Now, consider what is the result of applying the Hamiltonian to the state we defined in Eq. C.12

. It results in,

$$H_{BCS} |\Psi\rangle = \begin{bmatrix} H_{BCS} c_{\mathbf{k},\uparrow}^\dagger \\ H_{BCS} c_{-\mathbf{k},\downarrow} \end{bmatrix} |\Psi_{BCS}\rangle \quad (\text{C.15})$$

From the commutation relations derived in Eq. C.13 and Eq. C.14, we rewrite the previous equation as,

$$H_{BCS}|\Psi\rangle = \begin{bmatrix} \xi_{\mathbf{k}}c_{\mathbf{k}\uparrow}^\dagger - \Delta_{\mathbf{k}}^*c_{-\mathbf{k}\downarrow} + c_{\mathbf{k}\uparrow}^\dagger H_{BCS} \\ -\xi_{\mathbf{k}}c_{-\mathbf{k}\downarrow} - \Delta_{\mathbf{k}}c_{-\mathbf{k}\downarrow}^\dagger + c_{-\mathbf{k}\downarrow} H_{BCS} \end{bmatrix} |\Psi_{BCS}\rangle \quad (\text{C.16})$$

$$H_{BCS}|\Psi\rangle = \begin{bmatrix} (\xi_{\mathbf{k}} + E_{BCS})|\Psi_1\rangle - \Delta_{\mathbf{k}}^*|\Psi_2\rangle \\ -\Delta_{\mathbf{k}}|\Psi_1\rangle + (E_{BCS} - \xi_{\mathbf{k}})c_{-\mathbf{k}\downarrow}^\dagger|\Psi_2\rangle \end{bmatrix} \quad (\text{C.17})$$

At this point, we can define the Bogoliubov-de-Gennes Hamiltonian considering that the reference energy  $E_{BCS} = 0$ . That is, excitations energy are measured with respect to the condensate energy,

$$H_{BdG}(\mathbf{k}) = \begin{bmatrix} \xi_{\mathbf{k}} & -\Delta_{\mathbf{k}}^* \\ -\Delta_{\mathbf{k}} & -\xi_{\mathbf{k}} \end{bmatrix} \quad (\text{C.18})$$

The energy of the excitations are obtained by diagonalizing Eq. C.18. Energies are given by,

$$E_{\pm\mathbf{k}} = \pm \sqrt{\xi_{\mathbf{k}}^2 + |\Delta_{\mathbf{k}}|^2} \quad (\text{C.19})$$

To obtain the Real-Space Bogoliubov de Gennes Hamiltonian, we Fourier transform Eq. C.18. It is written as,

$$H_{BdG}(\mathbf{r}) := \frac{1}{N} \sum_{\mathbf{k}} e^{i\mathbf{k}\cdot\mathbf{r}} H_{BdG}(\mathbf{k}) = \begin{bmatrix} H_0(\mathbf{r}) & -\Delta(\mathbf{r}) \\ -\Delta^*(\mathbf{r}) & -H_0(\mathbf{r}) \end{bmatrix} \quad (\text{C.20})$$

The diagonal contribution is the free Hamiltonian. Free represents that it is not superconducting, but is given by the kinetic and potential operators which are spatially dependent. It is given as,

$$H_0(\mathbf{r}) = -\frac{\hbar^2}{2m} \nabla^2 - \mu + V(\mathbf{r}) \quad (\text{C.21})$$

The Schrodinger equation can be rewritten as,

$$H_{BdG}(\mathbf{r})\Psi(\mathbf{r}) = E(\mathbf{r}) \quad (\text{C.22})$$

## Appendix D

# Topology in Condensed Matter: SSH Model

The Su-Schrieffer-Hegger (SSH) model is a paradigmatic model of topological insulators (TI). It introduces the foundations of a topological invariant quantity, and the treatment of the bulk and edge properties that will be required later. It was originally proposed to describe topological solitons in polyacetylene which is a linear polymer  $(CH)_x$ . The polyacetylene molecule has a periodic structure of single and double bonds between carbon atoms. It can be represented as a periodic superlattice double-well potential with intra-cell and inter-cell hopping parameters. The SSH Hamiltonian for a chain of  $L$  lattice sites for spinless fermions with intercell hopping  $t_1$  and intracell hopping  $t_2$  can be written as,

$$H = - \sum_{j \text{ odd}}^{L-1} (t_1 c_{j+1}^\dagger c_j + H.C.) - \sum_{j \text{ even}}^{L-2} (t_2 c_{j+1}^\dagger c_j + H.C.) \quad (\text{D.1})$$

Where  $c_j$  are the usual annihilation operator with anticommutation relations, and the hopping parameters are real. We restrict our treatment to the single-particle basis by introducing an unit cell with two sublattices A and B. The intercell hopping can be represented as  $|B, j\rangle \langle A, j|$ , and the intracell as  $|A, j+1\rangle \langle B, j|$ . The Hamiltonian in this new basis can be written as,

$$H = - \sum_{j=1}^N (|B, j\rangle \langle A, j| + H.C.) - \sum_{j=1}^{N-1} (|A, j+1\rangle \langle B, j| + H.C.) \quad (\text{D.2})$$

### D.1 Bulk Properties

The periodicity of the system implies that the Hamiltonian is invariant under translations on the site space  $|j\rangle \rightarrow |j+l\rangle$  where  $l$  is an integer times the lattice constant. The full Hamiltonian includes the site space, and the sublattice space. Their states are defined as  $|j, \circ\rangle = |j\rangle \otimes |\circ\rangle$ . At this point we can introduce the concept of internal and external degrees

of freedom. That is,  $|j\rangle \in \mathcal{H}_{external}$  and  $|\circ\rangle \in \mathcal{H}_{internal}$ . The external degree of freedom can be Fourier transformed out,

$$|k\rangle = \frac{1}{\sqrt{N}} \sum_{j=1}^N e^{ijk} |j\rangle \quad \text{where } k = \frac{2\pi}{N}, \frac{4\pi}{N}, \dots, 2\pi. \quad (\text{D.3})$$

The inverse Fourier transform can be written as,

$$|j\rangle = \frac{1}{\sqrt{N}} \sum_k e^{-ijk} |k\rangle \quad \text{where } j = 1, 2, \dots, N. \quad (\text{D.4})$$

The orthonormality of the basis functions is written as,

$$\sum_j e^{-(k-k')j} = N\delta_{k,k'}. \quad (\text{D.5})$$

We substitute the previous expression the Hamiltonian. The Fourier transform of each term is given by,

$$\begin{aligned} \sum_{j=1}^N |j\rangle \langle j| &= \frac{1}{N} \sum_j \sum_{k,k'} e^{-(k-k')j} |k\rangle \langle k'| \\ &= \sum_{k,k'} \delta_{k,k'} |k\rangle \langle k'| = \sum_k |k\rangle \langle k|, \end{aligned} \quad (\text{D.6})$$

$$\begin{aligned} \sum_{j=1}^N |j+1\rangle \langle j| &= \frac{1}{N} \sum_j \sum_{k,k'} e^{-ik(j+1)} e^{ik'j} |k\rangle \langle k'| \\ &= \sum_{k,k'} e^{-ik} \delta_{k,k'} |k\rangle \langle k'| = \sum_k e^{-ik} |k\rangle \langle k| \end{aligned} \quad (\text{D.7})$$

Then, the Hamiltonian in the Fourier transform basis is written as,

$$H = \sum_k |k\rangle \langle k| \otimes [-(t_1 + t_2 e^{-ik}) |A\rangle \langle B| + H.C.] = \sum_k |k\rangle \langle k| \otimes H_{Bloch}(k). \quad (\text{D.8})$$

All the information of the internal degrees of freedom is contained inside the Bloch Hamiltonian  $H_{Bloch}(k)$ . An ansatz, based on the Bloch theorem, for the eigenstates is that  $|\psi_n(k)\rangle = |k\rangle \otimes |u_n(k)\rangle$  where  $|u_n(k)\rangle = a_n(k) |A\rangle + b_n(k) |B\rangle$  is a Bloch function. Thus, the eigenvalue problem  $H |\psi_n\rangle = E_n |\psi_n\rangle$  can be written as  $H_{Bloch} |u_n(k)\rangle = E_n(k) |u_n(k)\rangle$ . In a matrix form, it can be expressed as,

$$H_{Bloch} = \begin{bmatrix} 0 & t_1 + t_2 e^{-ik} \\ t_1 + t_2 e^{ik} & 0 \end{bmatrix}. \quad (\text{D.9})$$

Its energy spectra is given by solving the secular equation and is given by,

$$E_{1,2}(k) = \pm \sqrt{t_1^2 + t_2^2 + 2t_1 t_2 \cos(k)} \quad (\text{D.10})$$

## D.2 Edge States

The bulk is characterized by a translational invariant symmetry, and the edges can be characterized in the thermodynamic limit. To start, consider the fully dimerized limits. First,  $t_1 = 1$  and  $t_2 = 0$ , which we call the trivial phase. In this phase, the chain becomes a sequence of disconnected dimers.

$$\hat{H}(|m, A\rangle \pm |m, B\rangle) = \pm(|m, A\rangle \pm |m, B\rangle). \quad (\text{D.11})$$

The second case,  $t_1 = 0$  and  $t_2 = 1$ , which we call topological. In this phase, the dimers of carbon atom are formed between atoms from different unit cells. Each end of the chain remains unconnected and hosts a zero-energy state.

$$\hat{H}(|m, A\rangle \pm |m + 1, B\rangle) = \pm(|m, A\rangle \pm |m + 1, B\rangle). \quad (\text{D.12})$$

The ends of the chain are eigenstates of the Hamiltonian as,

$$\hat{H} |1, A\rangle = \hat{H} |N, B\rangle = 0. \quad (\text{D.13})$$



## Appendix E

# Effective Hamiltonians and Block Diagonalization

An effective Hamiltonian allows us to obtain an approximate solution in a subspace of the full problem. It is solved for certain subset of the eigenvalues and eigenvectors that are of our interest. Depending on the problem<sup>44</sup>, we can neglect the second subspace, or consider its influence onto the first one. For instance, consider the model of graphene that we discussed in the Sec. 2.2. In that case, we restricted to one  $|p_z\rangle$  orbital per atom. Interestingly, the physics of a Dirac-like Hamiltonian can be derived. However, there are far more interactions that can be included into the model. For instance, there is a non-zero Spin Orbit interaction that our model cannot explain. Instead, Kane and Mele propose an effective model that does include spin interactions<sup>38</sup>. Furthermore, the influence of the  $d$ -orbitals describe an assymetry found at the K point<sup>63</sup>. The role of the block diagonalization methods is to include the details of one subspace effectively into the interesting one. In the effective model, the  $|p_z\rangle$  states represent an effective orbital that accounts for the extra interactions.

In general, effective Hamiltonians can be divided into two subclasses: Energy-dependent and energy-independent. Early developments of energy-dependent effective Hamiltonians were done by Lowdin<sup>64,65</sup>. On the other hand, the energy-independent approach is used when there is degeneracy of the energy levels<sup>44</sup>. In this section we discuss energy-independent partitioning techniques. We compare this with the early proposals of Lowdin, and use the methodology to obtain the energies of the Spin Orbit interaction in a graphene monolayer.

### E.0.1 Energy-Independent Partitioning Methods

To begin, let's write in matrix notation the problem that we are describing. Let  $H_{AA}$  and  $H_{BB}$  block matrices that represent the subspace A and B respectively. We are mainly interested in the subspace A, and we want to obtain an effective Hamiltonian for A where B can be included as a correction up to an arbitrary order. The coupling between these subspaces is given by  $H_{AB}$ . We assume that the coupling between them is weak<sup>44</sup>. This problem can be written

as,

$$H = \begin{bmatrix} H_{AA} & H_{AB} \\ H_{AB}^\dagger & H_{BB} \end{bmatrix} \quad (\text{E.1})$$

Our strategy is to diagonalize Eq. E.1 by considering a unitary transformation such that,

$$H' = U^\dagger H U \quad H' = \begin{bmatrix} H_{AA} & 0 \\ 0 & H_{BB} \end{bmatrix} \quad (\text{E.2})$$

Let  $U = e^S$ , where U and S are operators. To obtain a valid transformation, U must be unitary. Then,

$$1 = U^\dagger U = (e^S)^\dagger e^S = e^{S^\dagger} e^S = e^{-S} e^S = 1 \quad (\text{E.3})$$

As a consequence of the unitarity of U, we find that S must be anti-Hermitian. That is,  $S^\dagger = -S$ . Now, we have to find a representation for S. It can be found in terms of the following infinite formula<sup>66</sup>,

$$e^{-L} A e^L = A + [A, L] + \frac{1}{2} [[A, L], L] + \dots \quad (\text{E.4})$$

Let's consider up to linear terms in the coupling. Then,

$$H' = e^{-S} H e^S \approx H + [H, S] \quad (\text{E.5})$$

At this point, we consider the following representation for S in terms of M, which satisfies the anti-Hermiticity. In any case, the problem now is to find a representation for the matrix M. This representation is, as we see, perturbative.

$$S = \begin{bmatrix} 0 & M \\ -M^\dagger & 0 \end{bmatrix} \quad (\text{E.6})$$

We want to find Eq. E.5, so we find the commutators in that expression.

$$[H, S] = \begin{bmatrix} -H_{AB}M^\dagger - MH_{AB}^\dagger & H_{AA}M - MH_{BB} \\ M^\dagger H_{AA} - H_{BB}M^\dagger & H_{AB}^\dagger M + M^\dagger H_{AB} \end{bmatrix} \quad (\text{E.7})$$

The following equations are obtained,

$$H'_{AA} = H_{AA} - H_{AB}M^\dagger - MH_{AB}^\dagger \quad (\text{E.8})$$

$$H_{AB} + H_{AA}M - MH_{BB} = 0 \quad (\text{E.9})$$

Assuming that the inverse of  $H_{BB}$  exists, from Eq. E.9 an expression for M can be derived. It is important to note that the nature of this solution is perturbative. That is,

$$M = H_{AA}H_{BB}^{-1} + H_{AA}MH_{BB}^{-1} \quad (\text{E.10})$$

A feature of the Hamiltonian is that it should be invariant under diagonal shifts. Consider such shift for Eq. E.9 and Eq. E.10. It reads,

$$H_{AB} + (H_{AA} + \mathbf{1}\nu)M - M(H_{BB} + \mathbf{1}\nu) = 0 \quad (\text{E.11})$$

$$M = (H_{AA} + \mathbf{1}\nu)(H_{BB} + \mathbf{1}\nu)^{-1} + (H_{AA} + \mathbf{1}\nu)M(H_{BB} + \mathbf{1}\nu)^{-1} \quad (\text{E.12})$$

It is clear that while the first equation is invariant under such shift, the latter one is not. In fact, by taking a perturbative solution, we lose this symmetry. It is recovered only when we take the infinite sum of the corrections. Boykin<sup>44</sup> propose a way to address this problem. It is based on the right choice for the basis functions. That is, choose a basis set that "almost" diagonalize  $H$ . Then, the eigenvalue problem for each subspace is solved by,

$$\begin{bmatrix} H_{AA} & 0 \\ 0 & H_{BB} \end{bmatrix} \begin{bmatrix} \mathbf{v}_A^{(\alpha)} \\ 0 \end{bmatrix} = \epsilon_\alpha^{(A)} \begin{bmatrix} \mathbf{v}_A^{(\alpha)} \\ 0 \end{bmatrix} \quad (\text{E.13})$$

$$\begin{bmatrix} H_{AA} & 0 \\ 0 & H_{BB} \end{bmatrix} \begin{bmatrix} 0 \\ \mathbf{v}_B^{(\beta)} \end{bmatrix} = \epsilon_\beta^{(B)} \begin{bmatrix} 0 \\ \mathbf{v}_B^{(\beta)} \end{bmatrix} \quad (\text{E.14})$$

The subspaces A and B are diagonal in this basis, that is,

$$[H_{AA}]_{\alpha\alpha'} = \epsilon_\alpha^{(A)} \delta_{\alpha\alpha'} \quad (\text{E.15})$$

$$[H_{BB}]_{\beta\beta'} = \epsilon_\beta^{(B)} \delta_{\beta\beta'} \quad (\text{E.16})$$

In order to calculate an effective Hamiltonian for the subspace A, we calculate the formula Eq. E.9. To do so, and assuming Einstein summation convention, consider the following expressions

$$[H_{AA}M]_{\alpha\beta} = \epsilon_\alpha^{(A)} \delta_{\alpha\alpha'} M_{\alpha'\beta} = \epsilon_\alpha^{(A)} M_{\alpha\beta} \quad (\text{E.17})$$

$$[MH_{BB}]_{\alpha\beta} = \epsilon_\beta^{(B)} M_{\beta\alpha} \quad (\text{E.18})$$

Then,

$$\begin{aligned} [H_{AB}]_{\alpha\beta} &= (\epsilon_\beta^{(B)} - \epsilon_\alpha^{(A)}) [M]_{\alpha\beta} \\ [M]_{\alpha\beta} &= \frac{1}{(\epsilon_\beta^{(B)} - \epsilon_\alpha^{(A)})} [H_{AB}]_{\alpha\beta} \end{aligned} \quad (\text{E.19})$$

The expression Eq. E.19 diverges when  $\epsilon_\beta^{(B)} = \epsilon_\alpha^{(A)}$ . In fact, they must be well-separated in energy for this expression to be valid. If not, the two subsystems are strongly coupled and a series expansion fails. Furthermore, the expansion can be considered up to an arbitrary order. Note that Eq. E.19 is linear in  $[H_{AB}]_{\alpha\beta}$ . The higher-order contributions do not change this expression. Since we are interested in the A subspace, we find Eq. E.8 by using Eq. E.19,

$$\begin{aligned} [H_{AA}M]_{\alpha\beta} &= \epsilon_\alpha^{(A)} \delta_{\alpha\beta} - [H_{AB}]_{\alpha\alpha'} \frac{1}{\epsilon_\beta^{(B)} - \epsilon_\alpha^{(A)}} [H_{AB}]_{\alpha\beta} - [M]_{\alpha\alpha'} [H_{AB}]_{\alpha\beta}^\dagger \\ [H_{AA}M]_{\alpha\beta} &= \epsilon_\alpha^{(A)} \delta_{\alpha\beta} - [H_{AB}]_{\alpha\alpha'} \frac{1}{(\epsilon_\beta^{(B)} - \epsilon_\alpha^{(A)})} [H_{AB}]_{\alpha'\beta}^\dagger - \frac{1}{(\epsilon_\beta^{(B)} - \epsilon_\alpha^{(A)})} [H_{AB}]_{\alpha\alpha'} [H_{AB}]_{\alpha'\beta}^\dagger \\ [H'_{AA}]_{\alpha\beta} &= \epsilon_\alpha^{(A)} \delta_{\alpha\beta} - \left( \frac{1}{(\epsilon_\beta^{(B)} - \epsilon_\alpha^{(A)})} + \frac{1}{(\epsilon_\beta^{(B)} - \epsilon_\alpha^{(A)})} \right) [H_{AB}]_{\alpha'\beta} [H_{AB}]_{\alpha\beta}^* \end{aligned} \quad (\text{E.20})$$



# Bibliography

- [1] Zhang, H. *et al.* Quantized Majorana conductance. *Nature* **2018**, *556*, 74–79.
- [2] Nadj-Perge, S.; Drozdov, I. K.; Li, J.; Chen, H.; Jeon, S.; Seo, J.; MacDonald, A. H.; Bernevig, B. A.; Yazdani, A. Observation of Majorana fermions in ferromagnetic atomic chains on a superconductor. *Science* **2014**, *346*, 602–607.
- [3] Konschuh, S.; Gmitra, M.; Kochan, D.; Fabian, J. Theory of spin-orbit coupling in bilayer graphene. *Phys. Rev. B* **2012**, *85*, 115423.
- [4] McCann, E. *Graphene Nanoelectronics*; Springer Berlin Heidelberg, 2011; pp 237–275.
- [5] Akhmerov, A.; Sau, J.; van Heck, B.; Nijholt, B.; Muhammad, I.; Rosdahl, T. O. *Topology in Condensed Matter*; 2013; EdX course.
- [6] Majorana, E.; Maiani, L. In *Ettore Majorana Scientific Papers: On occasion of the centenary of his birth*; Bassani, G. F., Ed.; Springer Berlin Heidelberg: Berlin, Heidelberg, 2006; pp 201–233.
- [7] Dirac, P. A. M.; Fowler, R. H. The quantum theory of the electron. *Proceedings of the Royal Society of London. Series A, Containing Papers of a Mathematical and Physical Character* **1928**, *117*, 610–624.
- [8] Beenakker, C.; Kouwenhoven, L. A road to reality with topological superconductors. *Nature Physics* **2016**, *12*, 618–621.
- [9] Beenakker, C. Search for Majorana Fermions in Superconductors. *Annual Review of Condensed Matter Physics* **2013**, *4*, 113–136.
- [10] Kitaev, A. Y. Unpaired Majorana fermions in quantum wires. *Physics-Uspekhi* **2001**, *44*, 131–136.
- [11] Yazdani, A.; Jones, B. A.; Lutz, C. P.; Crommie, M. F.; Eigler, D. M. Probing the Local Effects of Magnetic Impurities on Superconductivity. *Science* **1997**, *275*, 1767–1770.
- [12] Read, N.; Green, D. Paired states of fermions in two dimensions with breaking of parity and time-reversal symmetries and the fractional quantum Hall effect. *Phys. Rev. B* **2000**, *61*, 10267–10297.

- [13] Kitaev, A. Fault-tolerant quantum computation by anyons. *Annals of Physics* **2003**, *303*, 2 – 30.
- [14] Fu, L.; Kane, C. L. Superconducting Proximity Effect and Majorana Fermions at the Surface of a Topological Insulator. *Phys. Rev. Lett.* **2008**, *100*, 096407.
- [15] Sau, J. D.; Lutchyn, R. M.; Tewari, S.; Das Sarma, S. Generic New Platform for Topological Quantum Computation Using Semiconductor Heterostructures. *Phys. Rev. Lett.* **2010**, *104*, 040502.
- [16] Qu, F.; Yang, F.; Shen, J.; Ding, Y.; Chen, J.; Ji, Z.; Liu, G.; Fan, J.; Jing, X.; Yang, C.; Lu, L. Strong Superconducting Proximity Effect in Pb-Bi<sub>2</sub>Te<sub>3</sub> Hybrid Structures. *Scientific Reports* **2012**, *2*.
- [17] Sasaki, S.; Kriener, M.; Segawa, K.; Yada, K.; Tanaka, Y.; Sato, M.; Ando, Y. Topological Superconductivity in Cu<sub>x</sub>Bi<sub>2</sub>Se<sub>3</sub>. *Phys. Rev. Lett.* **2011**, *107*, 217001.
- [18] Koren, G.; Kirzhner, T.; Lahoud, E.; Chashka, K. B.; Kanigel, A. Proximity-induced superconductivity in topological Bi<sub>2</sub>Te<sub>2</sub>Se and Bi<sub>2</sub>Se<sub>3</sub> films: Robust zero-energy bound state possibly due to Majorana fermions. *Phys. Rev. B* **2011**, *84*, 224521.
- [19] Yang, F.; Ding, Y.; Qu, F.; Shen, J.; Chen, J.; Wei, Z.; Ji, Z.; Liu, G.; Fan, J.; Yang, C.; Xiang, T.; Lu, L. Proximity effect at superconducting Sn-Bi<sub>2</sub>Se<sub>3</sub> interface. *Phys. Rev. B* **2012**, *85*, 104508.
- [20] Wang, M.-X. *et al.* The Coexistence of Superconductivity and Topological Order in the Bi<sub>2</sub>Se<sub>3</sub> Thin Films. *Science* **2012**, *336*, 52–55.
- [21] Choy, T.-P.; Edge, J. M.; Akhmerov, A. R.; Beenakker, C. W. J. Majorana fermions emerging from magnetic nanoparticles on a superconductor without spin-orbit coupling. *Phys. Rev. B* **2011**, *84*, 195442.
- [22] Nadj-Perge, S.; Drozdov, I. K.; Bernevig, B. A.; Yazdani, A. Proposal for realizing Majorana fermions in chains of magnetic atoms on a superconductor. *Phys. Rev. B* **2013**, *88*, 020407.
- [23] Neupert, T.; Onoda, S.; Furusaki, A. Chain of Majorana States from Superconducting Dirac Fermions at a Magnetic Domain Wall. *Phys. Rev. Lett.* **2010**, *105*, 206404.
- [24] Lu, A.-H.; Salabas, E.; SchÄijth, F. Magnetic Nanoparticles: Synthesis, Protection, Functionalization, and Application. *Angewandte Chemie International Edition* **2007**, *46*, 1222–1244.
- [25] Nadj-Perge, S.; Drozdov, I. K.; Bernevig, B. A.; Yazdani, A. Proposal for realizing Majorana fermions in chains of magnetic atoms on a superconductor. *Phys. Rev. B* **2013**, *88*, 020407.
- [26] Law, K. T.; Lee, P. A.; Ng, T. K. Majorana Fermion Induced Resonant Andreev Reflection. *Phys. Rev. Lett.* **2009**, *103*, 237001.
- [27] Bolech, C. J.; Demler, E. Observing Majorana bound States in *p*-Wave Superconductors Using Noise Measurements in Tunneling Experiments. *Phys. Rev. Lett.* **2007**, *98*, 237002.

- [28] Morimoto, T.; Hatsugai, Y.; Aoki, H. Optical Hall Conductivity in Ordinary and Graphene Quantum Hall Systems. *Phys. Rev. Lett.* **2009**, *103*, 116803.
- [29] Nilsson, J.; Akhmerov, A. R.; Beenakker, C. W. J. Splitting of a Cooper Pair by a Pair of Majorana Bound States. *Phys. Rev. Lett.* **2008**, *101*, 120403.
- [30] Josephson, B. Possible new effects in superconductive tunnelling. *Physics Letters* **1962**, *1*, 251 – 253.
- [31] Wang, J.; Chang, C.-Z.; Li, H.; He, K.; Zhang, D.; Singh, M.; Ma, X.-C.; Samarth, N.; Xie, M.; Xue, Q.-K.; Chan, M. H. W. Interplay between topological insulators and superconductors. *Phys. Rev. B* **2012**, *85*, 045415.
- [32] Williams, J. R.; Bestwick, A. J.; Gallagher, P.; Hong, S. S.; Cui, Y.; Bleich, A. S.; Analytis, J. G.; Fisher, I. R.; Goldhaber-Gordon, D. Unconventional Josephson Effect in Hybrid Superconductor-Topological Insulator Devices. *Phys. Rev. Lett.* **2012**, *109*, 056803.
- [33] Veldhorst, M.; Molenaar, C. G.; Wang, X. L.; Hilgenkamp, H.; Brinkman, A. Experimental realization of superconducting quantum interference devices with topological insulator junctions. *Applied Physics Letters* **2012**, *100*, 072602.
- [34] Hafner, J.; Kresse, G. *Properties of Complex Inorganic Solids*; Springer US, 1997; pp 69–82.
- [35] Slater, J. C.; Koster, G. F. Simplified LCAO Method for the Periodic Potential Problem. *Phys. Rev.* **1954**, *94*, 1498–1524.
- [36] Wallace, P. R. The Band Theory of Graphite. *Phys. Rev.* **1947**, *71*, 622–634.
- [37] Novoselov, K. S.; Geim, A. K.; Morozov, S. V.; Jiang, D.; Katsnelson, M. I.; Grigorieva, I. V.; Dubonos, S. V.; Firsov, A. A. Two-dimensional gas of massless Dirac fermions in graphene. *Nature* **2005**, *438*, 197–200.
- [38] Kane, C. L.; Mele, E. J. Quantum Spin Hall Effect in Graphene. *Phys. Rev. Lett.* **2005**, *95*, 226801.
- [39] Heide, C.; Higuchi, T.; Weber, H. B.; Hommelhoff, P. Coherent Electron Trajectory Control in Graphene. *Phys. Rev. Lett.* **2018**, *121*, 207401.
- [40] McCann, E.; Kechedzhi, K.; Fal'ko, V. I.; Suzuura, H.; Ando, T.; Altshuler, B. L. Weak-Localization Magnetoresistance and Valley Symmetry in Graphene. *Phys. Rev. Lett.* **2006**, *97*, 146805.
- [41] Neil W. (Neil W. Ashcroft) Ashcroft, N. D. M. 1st ed.; Solid State Physics; Brooks Cole, 1976.
- [42] Berry, M. V. Quantal Phase Factors Accompanying Adiabatic Changes. *Proceedings of the Royal Society A: Mathematical, Physical and Engineering Sciences* **1984**, *392*, 45–57.
- [43] Peralta, M.; Medina, E.; Mireles, F. Proximity-induced exchange and spin-orbit effects in graphene on Ni and Co. *Phys. Rev. B* **2019**, *99*, 195452.

- [44] Boykin, T. B. Effective interactions and block diagonalization in quantum-mechanical problems. *Journal of Mathematical Chemistry* **2014**, *52*, 1599–1609.
- [45] Chevallier, D.; Klinovaja, J. Tomography of Majorana fermions with STM tips. *Phys. Rev. B* **2016**, *94*, 035417.
- [46] Li, J.; Chen, H.; Drozdov, I. K.; Yazdani, A.; Bernevig, B. A.; MacDonald, A. H. Topological superconductivity induced by ferromagnetic metal chains. *Phys. Rev. B* **2014**, *90*, 235433.
- [47] Zhong, W.; Overney, G.; Toma'nek, D. Structural properties of Fe crystals. *Physical Review B* **1993**, *47*, 95–99.
- [48] Würde, K.; Mazur, A.; Pollmann, J. Surface electronic structure of Pb(001), Pb(110), and Pb(111). *Phys. Rev. B* **1994**, *49*, 7679–7686.
- [49] Awoga, O. A.; Björnson, K.; Black-Schaffer, A. M. Disorder robustness and protection of Majorana bound states in ferromagnetic chains on conventional superconductors. *Physical Review B* **2017**, *95*.
- [50] Pawlak, R.; Hoffman, S.; Klinovaja, J.; Loss, D.; Meyer, E. Majorana fermions in magnetic chains. *Progress in Particle and Nuclear Physics* **2019**, *107*, 1–19.
- [51] Pawlak, R.; Kisiel, M.; Klinovaja, J.; Meier, T.; Kawai, S.; Glatzel, T.; Loss, D.; Meyer, E. Probing atomic structure and Majorana wavefunctions in mono-atomic Fe chains on superconducting Pb surface. *npj Quantum Information* **2016**, *2*.
- [52] Brydon, P. M. R.; Das Sarma, S.; Hui, H.-Y.; Sau, J. D. Topological Yu-Shiba-Rusinov chain from spin-orbit coupling. *Phys. Rev. B* **2015**, *91*, 064505.
- [53] Li, J.; Jeon, S.; Xie, Y.; Yazdani, A.; Bernevig, B. A. Majorana spin in magnetic atomic chain systems. *Phys. Rev. B* **2018**, *97*, 125119.
- [54] Li, P.; Sau, J. D.; Appelbaum, I. Robust zero-energy bound states in a helical lattice. *Phys. Rev. B* **2017**, *96*, 115446.
- [55] Ruby, M.; Heinrich, B. W.; Peng, Y.; von Oppen, F.; Franke, K. J. Exploring a Proximity-Coupled Co Chain on Pb(110) as a Possible Majorana Platform. *Nano Letters* **2017**, *17*, 4473–4477.
- [56] Timm, C. *Theory of Superconductivity*, 1st ed.; TU Dresden, 2012.
- [57] Tom Lancaster, S. J. B. *Quantum Field Theory for the Gifted Amateur*; Oxford University Press, 2014.
- [58] Meissner, W.; Ochsenfeld, R. Ein neuer Effekt bei Eintritt der Supraleitfähigkeit. *Die Naturwissenschaften* **1933**, *21*, 787–788.
- [59] The electromagnetic equations of the supraconductor. *Proceedings of the Royal Society of London. Series A - Mathematical and Physical Sciences* **1935**, *149*, 71–88.

- [60] Landau, L. D.; Pitaevskii, L. P.; Lifshitz, E. *Electrodynamics of Continuous Media: Volume 8 (Course of Theoretical Physics S)*; Butterworth-Heinemann, 1984.
- [61] Ketterson, J. B. *Superconductivity: Conventional and Unconventional Superconductors*, 1st ed.; Springer-Verlag Berlin Heidelberg, 2008.
- [62] Bardeen, J.; Cooper, L. N.; Schrieffer, J. R. Theory of Superconductivity. *Physical Review* **1957**, *108*, 1175–1204.
- [63] Boykin, T. B.; Luisier, M.; Klimeck, G.; Jiang, X.; Kharche, N.; Zhou, Y.; Nayak, S. K. Accurate six-band nearest-neighbor tight-binding model for the  $\tilde{\Gamma}$ -bands of bulk graphene and graphene nanoribbons. *Journal of Applied Physics* **2011**, *109*, 104304.
- [64] L $\ddot{u}$ wdin, P. A Note on the Quantum $\ddot{u}$  Mechanical Perturbation Theory. *The Journal of Chemical Physics* **1951**, *19*, 1396–1401.
- [65] L $\ddot{u}$ wdin, P. Studies in Perturbation Theory. V. Some Aspects on the Exact Self $\ddot{u}$  Consistent Field Theory. *Journal of Mathematical Physics* **1962**, *3*, 1171–1184.
- [66] F. Constantinescu, E. M. *Problems in Quantum Mechanics*; Monographs in Natural Philosophy; Pergamon Pr, 1971.